Chemical Science

ROYAL SOCIETY OF CHEMISTRY

REVIEW

View Article Online
View Journal

Cite this: DOI: 10.1039/d6sc01670g

Advanced functional porous materials for photocatalytic H_2O_2 production

Sagarmani Rasaily, [a] Gourab K. Dam [a] and Sujit K. Ghosh *[ab]

Hydrogen peroxide (H_2O_2) is one of the most essential chemicals; it has a high oxidising ability (1.763 V at pH 0) and the highest active oxygen content (47.1 wt%). Current synthesis techniques are energy-intensive, generate harmful waste, and pose the potential danger of explosions. Photocatalytic H_2O_2 production *via* O_2 reduction is a promising, sustainable, and eco-friendly method that harnesses solar energy to drive the reaction while also requiring low energy input and ensuring safety. Interestingly, advanced functional porous materials (AFPMs) like covalent organic frameworks (COFs), metal–organic frameworks (MOFs), porous organic polymers (POPs), covalent triazine frameworks (CTFs), metal–organic polyhedra (MOP) and hydrogen bonded organic frameworks (HOFs) have surfaced as promising photocatalysts for effective photocatalysis. These materials exhibit a tunable pore size, high surface area, and robust framework, all of which facilitate mass transfer, adequate active sites, and efficient recycling. In this review, we have discussed the different strategies applied in recent literature to improve the photocatalytic efficiency of these materials towards photocatalytic H_2O_2 synthesis. This review provides an extensive summary and discussion of the latest applications of AFPM-based photocatalysts in H_2O_2 photosynthesis. The historical background and fundamental principles underlying photocatalysts for photocatalytic H_2O production are briefly outlined. This is followed by a detailed classification and discussion of the strategies reported to enhance photocatalytic performance. The review addresses the challenges and future prospects of AFPM-based photocatalysts for light-driven H_2O_2 production.

Received 27th February 2026
Accepted 3rd May 2026

DOI: 10.1039/d6sc01670g

rsc.li/chemical-science

Introduction

Hydrogen peroxide (H_2O_2), first prepared by Thenard in 1818, is a product of a reaction between barium peroxide and nitric acid.[1] Also known as oxygenated water, H_2O_2 is a non-planar molecule with C_2 symmetry and enantiomerism, attributed to its 95° dihedral angle between its two O–H bonds. Besides being the smallest and simplest chiral molecule, H_2O_2 can act as both a strong oxidant across a wide pH range and a reducing agent capable of reducing stronger oxidising compounds such as $Ce(SO_4)_2$, $KMnO_4$, Cl_2, NaClO, *etc.*[1] Additionally, the derivatives of H_2O_2, such as hydroxyl radicals ($^{\bullet}OH$), can break down nearly all types of organic pollutants or damage essential components within microbial cells, leading to the removal of organic contaminants or the elimination of harmful microorganisms.[2,3] Initially, H_2O_2 was known for bleaching natural dyes and was synthesised from barium peroxide. Gradually, researchers found applications of H_2O_2 in various fields. The significant timeline of H_2O_2 towards various applications includes the following: (a) 1888: its first medical use for treating numerous diseases, (b) 1891: first report as a disinfectant,[4] (c) 1920: reports of using an intravenous injection of H_2O_2 for treating influenza pneumonia during the first World War,[5] (d) 1967: protective action of H_2O_2 against ischemia-reperfusion (IR) injury,[6] (e) 1980: intravenous infusion of H_2O_2 for oxidative therapy,[7] (f) H_2O_2 as an alternative to chlorine as a bleaching agent in paper production,[8] and (g) as a terminal oxidant towards industrial synthesis of propene epoxide (PO).[8] Today, H_2O_2 has been established as one of the most essential chemicals globally.[9] It is recognised as a versatile and sustainable reagent. With the improvement of technologies, it is more dedicatedly applied in chemical synthesis, paper and pulp bleaching, food processing, biomedical therapy, disinfection, wastewater treatment, metal mining and processing, *etc.* (Scheme 1a).[10–12] Furthermore, H_2O_2 is an eco-friendly and safe energy storage medium, offering an energy density of 2.1 MJ kg^{-1} at 60 wt%, making it ideal for applications in H_2O_2 fuel cells and cutting-edge power technologies. The H_2O_2 fuel cell, with a voltage of +1.09 V *vs.* NHE (standard hydrogen electrode), is similar in performance to the methanol fuel cell (+1.21 V) and the H_2 fuel cell (+1.23 V), making it an environmentally benign alternative as an energy carrier.[13] The increasing use of H_2O_2 has led to a rise in global demand, reaching a market volume of 270 000 tons in 2023, with projections to grow to 400 000 tons by 2032 (Scheme 1b).[14] Due to the various intriguing properties and versatile

[a]*Department of Chemistry, Indian Institute of Science Education and Research (IISER) Pune, 411008, India*

[b]*Centre for Water Research (CWR), Indian Institute of Science Education and Research (IISER) Pune, 411008, India. E-mail: sghosh@iiserpune.ac.in*

applications, the market value of H_2O_2 was estimated at $5.2 billion in 2023. According to the report, this is expected to grow to $8.8 billion by 2032 (Scheme 1b).[15]

The first commercial production of H_2O_2 was achieved by 1909 *via* an electrochemical method using H_2SO_4. A major advancement in H_2O_2 production emerged in the 1930s with the development of oxidation-based synthetic routes, which were subsequently scaled up for industrial application during the 1940s. The oxidation process was proven to be economically more preferred over the electrolytic process, and two processes, namely isopropyl oxidation and anthraquinone oxidation (AO), were developed for the large-scale production of H_2O_2. Today, the rising global demand for H_2O_2 is mainly satisfied using the AO process developed by IG Farben (now BASF).[1,8] The AO process primarily involves the hydrogenation of 2-ethylanthraquinone to form 2-ethylanthrahydroquinone and its oxidation further using a Pd or Ni catalyst. The AO process demands hydrogen in high purity and oxygen or air for non-catalytic oxidation. Consequently, the AO process could produce H_2O_2 with up to 60–70% w/w strength. However, the AO process is less atom-economic and energy-intensive, with an energy requirement of ~13 000 Btu lb^{-1} (8.1 kWh kg^{-1}).[17] On the other hand, the isopropyl oxidation process has significant drawbacks for industrial H_2O_2 production, as it requires large quantities of raw materials and faces challenges in isolating H_2O_2 with high purity.[18] Apart from the oxidation process, the direct synthesis of H_2O_2 is also well known. It can produce ~61 moles per kilogram of catalyst (kg cat) per hour by reacting H_2 and O_2 at high pressure and using a Pd–Sn catalyst.[19–21] However, the explosive nature of H_2 and O_2 under high pressure and the requirement for novel metal catalysts have limited the industrial-scale synthesis.[19,22] Therefore, with the significant limitations of conventional methods, there is significant focus and research to explore and develop eco-friendly alternatives for producing H_2O_2, addressing both the rising demand and the need for environmentally benign H_2O_2 production methods. A schematic of the timeline for the production of H_2O_2 using different techniques is provided in Scheme 1c.[16] Towards developing sustainable alternative processes for H_2O_2 production, electrochemical and photocatalytic techniques have gained significant interest. In electrochemical techniques, H_2O_2 can be produced by the reduction of O_2 in H_2O under ambient conditions, also well known as a two-electron oxygen reduction reaction ($2e^-$ ORR). It offers numerous benefits, including safe operation, a clean production process,

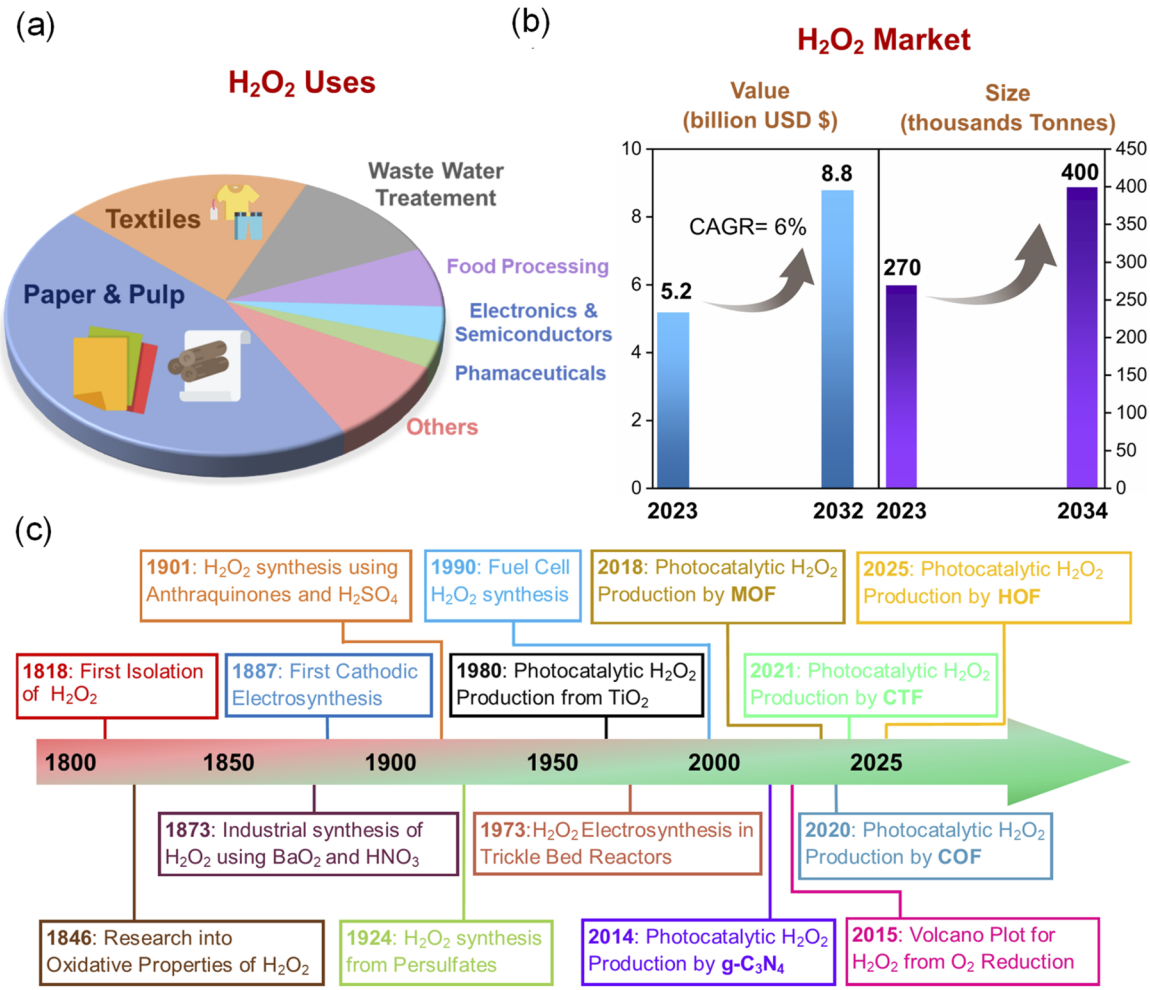

Scheme 1 (a) Pi diagram showing various uses of H_2O_2.[14] (b) Summary of the expected market value.[14,15] (c) Schematic timeline for the synthesis of H_2O_2 using different techniques.[16]

simple reactions under ambient conditions, and low energy consumption. However, the electrochemical $2e^-$ ORR is often hindered by a high overpotential due to slow kinetics and is also influenced by the competing four-electron pathway that leads to the production of H_2O. Significant research is going on for its development towards H_2O_2 production. Various efficient electrocatalysts have been reported that include metal oxides,[23,24] single-atom catalysts (SACs),[25–27] carbon materials,[28,29] porous materials,[30] *etc*. On the other hand, the photocatalytic production of H_2O_2 using solar energy is one of the most sustainable methods of producing H_2O_2. Sunlight, a clean and abundant source, provides more than 1.19×10^{17} J of energy to the Earth per second. In nature, green plants and certain organisms are well known to harness solar energy to convert carbon dioxide into carbohydrates through photosynthesis. Motivated by the conversion of solar energy to chemical energy is well-known chemistry today and is applied towards the production of valuable chemicals such as ammonia,[31] water splitting,[32–34] organic chemicals,[35–37] CO_2 reduction,[38,39] *etc.* The photocatalytic production of H_2O_2 has also gained significant interest recently and is developing as a promising alternative to conventional methods, especially targeting the decentralised production and *in situ* utilisation. The photocatalytic H_2O_2 production from abundant H_2O and O_2 as raw materials offers high product selectivity, high atom economy, and less waste production. The photosynthesis of H_2O_2 proceeds through an oxygen reduction reaction (ORR) and a water oxidation process (WOR). However, the photocatalytic production of H_2O_2 using water and oxygen is thermodynamically not feasible as it has a high ΔG value of ~117 kJ mol^{-1}. Therefore, developing an efficient photocatalyst is essential for the photocatalytic production of H_2O_2, and research in this area is gaining significant interest.

Mechanistic pathway towards photocatalytic H_2O_2

The photocatalytic production of H_2O_2 over functional porous materials typically involves three key steps: (i) light absorption, which excites electrons and generates photoinduced charge carriers, (ii) migration of these electrons from the valence band (VB) to the conduction band (CB), leaving behind holes—the energy gap between the VB and CB is also known as bandgap energy (BE)—and (iii) redox reactions between the remaining photogenerated carriers and surface-adsorbed O_2 and H_2O molecules, leading to H_2O_2 formation. For a photocatalyst to be efficient towards the desired photocatalytic reaction, the energy of the incident light must be equal to or exceed that of the photocatalyst, so that the electron and hole pairs can be photoexcited and separated into the CB and VB, respectively.

The production of H_2O_2 could be achieved through the ORR and WOR concomitantly. The ORR, leading to the formation of H_2O_2, typically proceeds through either a direct one-step $2e^-$ pathway or an indirect two-step, single-electron reduction (eqn (1), Scheme 2) or *via* a direct one-step, two-electron reduction (eqn (2), Scheme 2).[40] In the direct one-step ORR, the adsorbed oxygen is reduced by two electrons, and its combination with

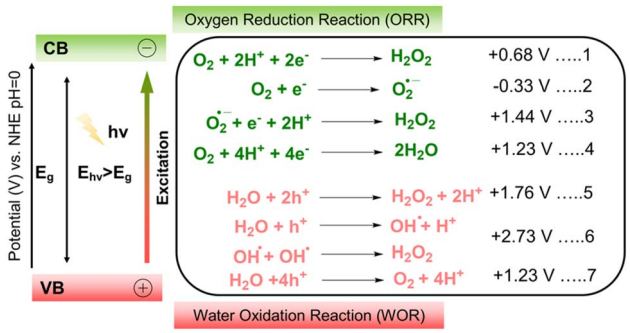

Scheme 2 Schematic illustration and energy diagram of the photocatalytic production of H_2O_2 over a photoactive COF-based material *via* the ORR pathway or WOR pathway, where potentials are given against the normal hydrogen electrode (NHE) at pH = 0.

two protons produces H_2O_2 directly (eqn (1), Scheme 2). The thermodynamic potential for procuring the direct $2e^-$ ORR pathway is 0.68 V. In the indirect two-step ORR pathway, the absorbed oxygen is first reduced with one electron to form the superoxide radical ($^{\bullet}O_2^-$) (eqn (2), Scheme 2). This is also the rate-determining step that requires a potential of −0.33 V. The superoxide formed then combines with one electron and two protons to produce H_2O_2 (eqn (3), Scheme 2). Additionally, the $2e^-$ ORR for H_2O_2 production competes with the $4e^-$ ORR pathway to H_2O (eqn (4), Scheme 2), which is thermodynamically more favourable due to its more positive potential (+1.23 V) compared to the $2e^-$ ORR (+0.68 V). Since the ORR pathway depends on photogenerated electrons, their rapid recombination with holes can significantly reduce the efficiency of H_2O_2 formation. The use of sacrificial agents such as methanol, ethanol, or benzyl alcohol can selectively scavenge photogenerated holes, suppress electron–hole recombination, and thereby enhance the overall photocatalytic performance. Similar to the ORR pathway, H_2O_2 can also be generated *via* the WOR route, in which photogenerated holes at the VB participate in the oxidation process leading to H_2O_2 formation. The WOR pathway for H_2O_2 production can be categorized into two mechanisms: (i) a direct one-step $2h^+$ oxidation process, in which H_2O is oxidized by two holes to generate H_2O_2 at a potential of 1.76 V (eqn (5), Scheme 2) and (ii) an indirect two-step pathway, where oxidation of H_2O at the valence band (eqn (6), Scheme 2) produces $^{\bullet}OH$ radicals that subsequently dimerize to form H_2O_2 (eqn (6), Scheme 2). However, the indirect route requires a much more positive potential (2.73 V), making it thermodynamically less favourable. In addition, the WOR can also proceed *via* $4h^+$ oxidation of H_2O to form O_2 at the VB (eqn (7), Scheme 2), and the generated O_2 may subsequently participate in a cascade $2e^-$ ORR process to yield H_2O_2.

Advanced functional porous materials (AFPMs) as photocatalysts

An ideal photocatalyst exhibits a broad light absorption range, a suitable band gap, efficient charge separation, long-term stability, abundant active sites, and low cost. The pioneering

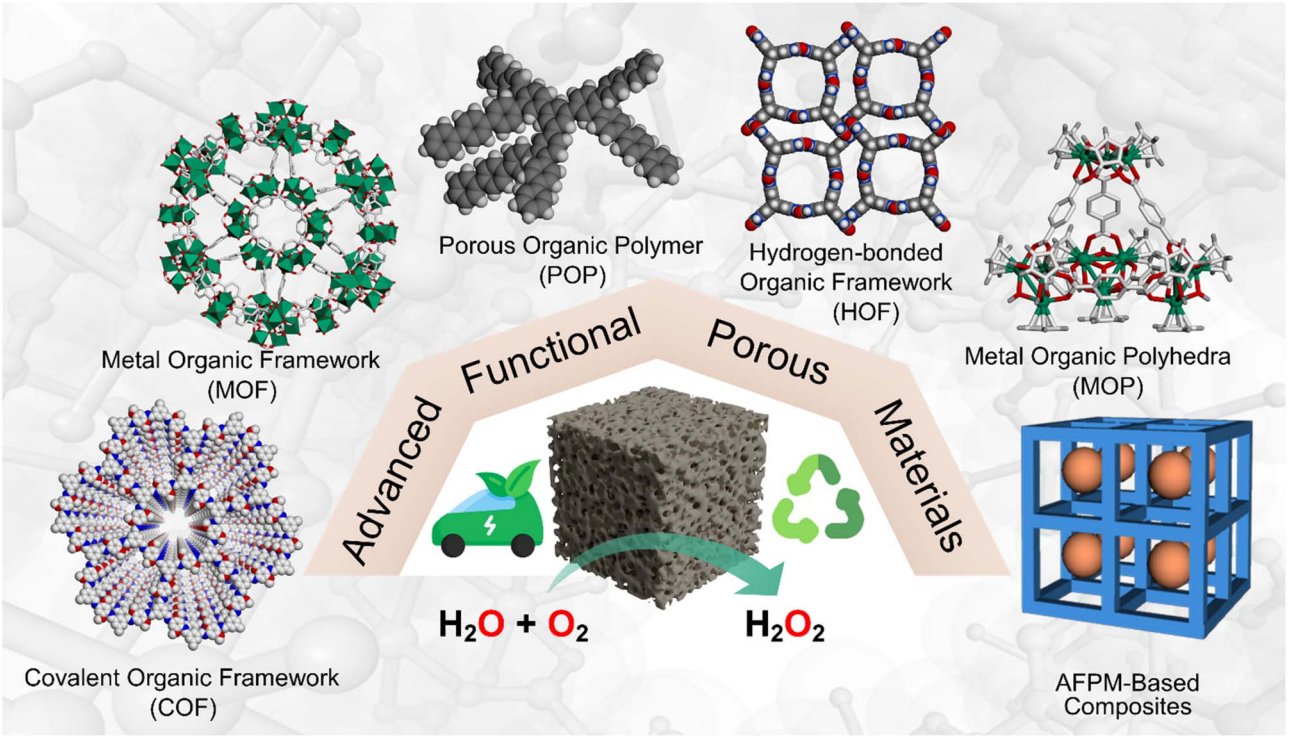

Scheme 3 Representation of various advanced functional porous materials discussed in this review for photocatalytic H_2O_2 production.

work on photocatalysis was reported by Fujishima and Honda in 1972, where titanium dioxide was demonstrated as an n-type semiconductor for water splitting under UV irradiation.[41] Since then, great efforts have been devoted to this research area, and various photocatalytic reactions have been carried out. A primary focus has been devoted to developing inorganic semiconductors such as metal oxides,[23] metal sulfides,[42,43] metal selenide quantum dots,[44] organic dyes,[45] *etc.* However, the practical applications of these photocatalysts are limited by the toxicity, high cost of rare metal components, and the inherent limitation of being non-recyclable. Additionally, many of them have a large band gap of approximately 3.2 eV and exhibit efficiency only under UV-light irradiation, which limits their use under visible light, resulting in low photocatalytic efficiency and photocurrent quantum yield. Metal-free organic semiconductors such as graphitic carbon nitride (g-C_3N_4) have shown promising efficiency under visible light irradiation. Apart from being metal-free, these materials also possess intriguing properties, such as being earth-abundant, having an appropriate band gap of approximately 2.7 eV, and exhibiting high thermal and chemical stability.[46,47] The suitable band structure also makes them ideal for constructing a type II heterojunction combined with other photoactive materials with large band gaps.[48] However, g-C_3N_4 has limited structural diversity and is typically synthesised through thermal polycondensation, which involves calcinating nitrogen-containing molecules at a temperature exceeding 600 °C.[49] In the quest for better photocatalysts, researchers are becoming more interested in exploring the photocatalytic performance of advanced functional porous materials (AFPMs). AFPMs refer to materials constructed from organic and/or inorganic building block units through various forces, such as coordination bonds, covalent and hydrogen bonds, *etc.* They exhibit standard features, including a high specific surface area, a periodic nanoporous structure, and tunable supramolecular structures. Following reticular chemistry, there have been reports of new types of porous materials that include metal–organic frameworks (MOFs), covalent-organic frameworks (COFs), porous organic polymers (POPs), covalent triazine frameworks (CTFs), metal–organic polyhedra (MOPs), and hydrogen-bonded organic frameworks (HOFs). Owing to their large surface area, these materials have been widely explored for separation and gas storage. However, research has also been propelled towards demonstrating their potential as efficient photocatalysts particularly towards H_2O_2 production (Scheme 3).

Advantages of AFPM-based photocatalysts

In contrast to traditional semiconductors, functional porous materials exhibit common characteristics and several distinct advantages that make them particularly beneficial for photocatalysis. The main advantages of AFPMs are: (1) a high surface area, which enables efficient mass transport, and their large pore channels, which allow molecules to pass through, resulting in more accessible active sites where substrates can bind and react. (2) Enhanced light-harvesting capability, where π-conjugated frameworks and chromophoric or semiconductive units enhance light harvesting by enabling broad visible-light absorption. (3) Tunable pore structure and morphology, where hierarchical porosity could

be introduced to enhance selective diffusion of solvents, mass transport, and better accommodation of reactants/products. (4) Tunable electronic structure, which can be tuned through functional groups or donor–acceptor units to adjust the bandgap, charge separation, and redox properties. (5) High functionalisation flexibility that enables diverse post-synthetic modifications for easy incorporation of catalytic sites, creation of polar environments, and tuning of surface charge. (6) Structural stability and reusability of many AFPMs arising from their chemical robustness and thermal stability, enabling long-term cycling without loss of activity. With all these intriguing properties, AFPMs have been extensively applied to photocatalysis, especially MOFs and COFs. The pioneering work of Zecchina's group in 2004 showed Zn_4O_{13} clusters in MOF-5 to behave similarly to ZnO quantum dots (QDs).[50] In 2007, Garcia and coworkers reported the first application of MOFs in photocatalysis using MOF-5 as a photocatalyst for phenol degradation.[51] Extensive research has been carried out after that, and the progress of MOFs as a photocatalyst has been summarised in many reviews.[52–54] Similarly, the first report of COFs towards photocatalysis was recorded in 2010 by Müllen and coworkers, where COFs have been identified as a novel poly(azomethine) network (ANW) and explored towards photocatalytic H_2 evolution.[55] Recent advances in using COFs as photocatalysts have been summarised in various reviews.[56,57] Regarding photocatalysis, MOFs that are constructed *via* metal nodes coordinated to organic ligands have large band gaps, which are not feasible for photocatalytic reactions or require high energy to generate electron–hole pairs. Conversely, COFs present a significant opportunity to address the aforementioned challenges at the photocatalyst level. Furthermore, the metal-free nature makes it a more favourable catalyst in terms of environmental considerations. However, the synthesis complexity and photostability are major challenges in using COFs as photocatalysts. POPs are also popular photocatalysts for a wide range of photocatalytic applications.[58,59] However, their amorphous nature is a major challenge, as non-crystalline materials typically exhibit poorer photocatalytic performance due to the defects in the structure which disrupt conjugation and hinder efficient charge separation and migration. Various types of AFPMs exhibit distinct characteristics in terms of monomer structure, preparation methods, and optical properties, and each presents its own set of challenges. Different approaches enhancing the performance of AFPMs have been proposed, which include methods such as ligand functionalization, mixed-metal/linker strategies, metal ion/ligand immobilisation, metal nanoparticle loading, semiconductor coupling, composite synthesis, *etc.* In this review, we discuss the photocatalytic applications of various AFPMs, with a focus on H_2O_2 production, and relate their photocatalytic performance to the structural and electronic properties of their compositional components.

AFPM-based photocatalysts for H_2O_2 production

As the demand for H_2O_2 continues to rise and the search for environmentally friendly production methods intensifies, several well-known semiconductors, such as metal oxides and g-C_3N_4, have garnered significant attention towards photocatalytic H_2O_2 production.[23,60] Metal oxides such as TiO_2 serve as a benchmark photocatalyst for H_2O_2 production through two-electron oxygen reduction under UV/visible light irradiation. Due to the wide band gap of TiO_2, it has often been combined with other materials to form a composite appropriate for H_2O_2 photosynthesis. Modifications such as Au–Ag or Pd cocatalysts enhance charge separation and selectivity for H_2O_2 production on TiO_2 and achieve yields up to 3.6 mM.[61] Similarly, $BiVO_4$ has also shown efficiency for H_2O_2 production through $2e^-$ ORR pathways due to the favourable alignment of its conduction band edge.[62] Similar to metal oxides, modified metal sulfides have also shown promising efficiency for H_2O_2 production. 2D layered materials such as g-C_3N_4 also serve as the standard metal-free benchmark for photocatalytic H_2O_2 production, achieving ~20–30 μmol h^{-1} (pure water/O_2) *via* the $2e^-$ ORR due to its suitable conduction band (−0.4 to −1.0 V *vs.* NHE) for $^{\bullet}O_2^-$ formation, though limited by the poor WOR (VB ~+1.7 V) and recombination, yielding an apparent quantum yield (AQY) of ~0.5–2% at 420 nm.[63] Beyond conventional photocatalysts, lignin, one of the most abundant renewable aromatic biopolymer resources, has also recently been reported as an effective photocatalyst for H_2O_2 production.[64] In the past few years, there has been a notable increase in research focused on using porous materials for photocatalytic H_2O_2 production. The statistical data obtained by searching by using phrases "Photocatalytic Production of Hydrogen Peroxide" or "H_2O_2" and "Porous" or "Frameworks" as the title in the Web of Science database are shown in Fig. 1. Tremendous developments have been made in enhancing the photochemical efficiency of AFMPs towards light-driven H_2O_2 production, and are well documented in various reviews.[30,65–69] While previous reviews

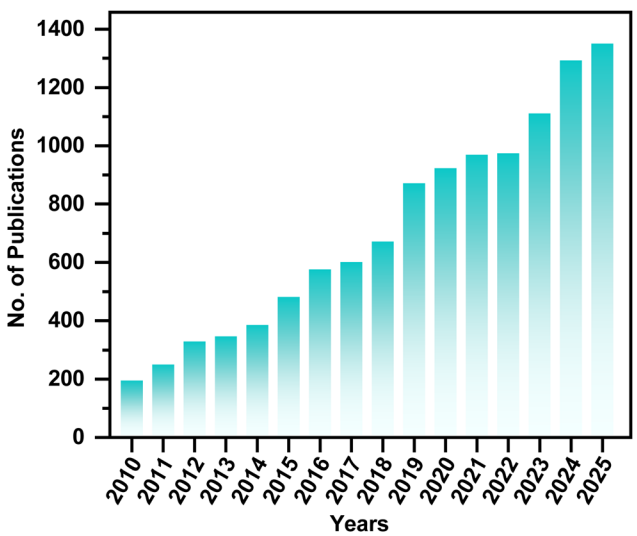

Fig. 1 Bar chart showing the number of articles per year concerning photocatalytic hydrogen peroxide production by advanced functional porous materials (accessed 21 January 2026). The statistical data were obtained by searching using the phrases "Photocatalytic Production of Hydrogen Peroxide" or "H_2O_2" and "Porous" or "Frameworks" in the Web of Science database, and the numbers correspond to the final publication year.

have extensively documented and discussed the progress of porous materials in photocatalytic H_2O_2 production, they typically focused on a single type of AFPM. In contrast, detailed reviews that collectively examine the progress and advances across all functional porous materials remain limited. Capitalising on this opportunity, the present review provides a unified and critical discussion of photocatalytic H_2O_2 production using a broad range of porous frameworks, including COFs, MOFs, POPs, CTFs, HCPs, HOFs, MOPs, and their composite systems. Considering the large volume of publications in this field and the fact that many earlier advances have already been comprehensively covered in previous reviews, this manuscript focuses on literature published between 2024 and 2025. Furthermore, the review highlights the key opportunities and challenges associated with AFPM-based photocatalysts, with particular emphasis on the synthetic techniques of AFPM photocatalysts, scalability toward practical applications, long-term photostability, long-term H_2O_2 production, and efficiency limitations. All AFPMs have been discussed as individual topics/subtopics for the readers. The review also provides perspectives on and recommendations for the future progress of this field.

Covalent organic framework (COF)-based photocatalysts for H_2O_2 production

COFs are porous materials composed of organic building blocks connected by strong covalent bonds. The covalent bonds are formed due to reactions like condensation, resulting in highly ordered, crystalline structures with large surface areas and tunable pore sizes (Fig. 2a). Since the pioneering work by Yaghi and co-workers[70] in 2005, they have attracted significant interest in terms of synthesis and applications.[71–73] Owing to their well-defined[74] structures, high crystallinity, permanent porosity, unlimited tenability, metal-free nature, and appreciable stability, COFs have been established as a promising material for catalysis,[75,76] capture and separation,[77,78] energy materials,[79,80] bioapplication,[81] sensing,[82,83] pollutant degradation,[84] CO_2 reduction,[85] *etc.* In particular, enhanced charge separation, excellent light-harvesting capabilities, conjugated structures, semiconductor nature, and an opportunity to tune the band gap have made COFs an interesting photocatalytic material. The semiconductor behaviour of COFs was first reported by Jiang *et al.* for a boronic ester COF.[86] Later, in 2014, Stegbauer *et al.* explored the efficiency of a hydrazine-based COF in producing hydrogen from pure water upon irradiation with visible light, marking the first application of a COF as a photocatalyst.[74] COFs exhibit various intrinsic features that make them ideal for photocatalytic applications, including their crystalline, porous structure for efficient charge transport, extended π-conjugation for enhanced light absorption, and a high surface area that provides abundant active sites. Their modular design enables the precise tuning of electronic properties through the incorporation of functional groups, while excellent chemical and thermal stability ensure durability during photocatalytic reactions. To date, extensive research has reported the use of COFs as efficient metal-free heterogeneous photocatalysts for various applications, including CO_2 reduction, organic transformations, H_2 evolution, ammonia synthesis, and pollutant degradation.[87,88] The photocatalytic application of COFs towards H_2O_2 production was pioneered by Van Der Voort and coworkers in 2020, with a series of 2D imine-based COFs.[89] Since then, various strategies have been implemented to improve the photocatalytic efficiency of COFs. To be precise, donor–acceptor optimisation, functional group incorporation, linkage modification, topological and structural modification and post-synthetic modification (PSM) are some of the important areas that can severely impact the photocatalytic efficiency of COFs (Fig. 2b). These strategies have been meticulously discussed as subtopics in this review.

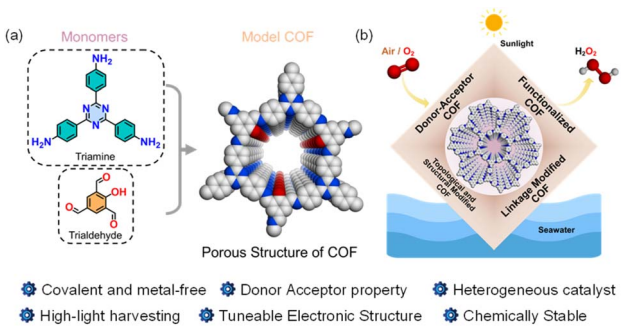

Fig. 2 (a) Model reaction for COF formation through a condensation reaction. (b) Application of COFs, discussed in this review, to enhance photocatalytic H_2O_2 production.

Donor–acceptor (D–A) COFs for photocatalytic H_2O_2 production

The donor–acceptor (D–A) architecture is an inherent property of COFs. The monomers, often comprising aromatic and π-electron-rich moieties, typically act as donors, while functionalities containing electron-deficient groups generally serve as acceptors. The alternating arrangement of D–A units in COFs enables band gap tunability, enhances charge transport, and promotes efficient electron–hole separation, collectively leading to improved photocatalytic performance.[90] D–A moieties within the framework also create a strong push–pull effect that promotes efficient charge separation and transfer. This effect lowers the electrostatic attraction between photogenerated carriers, thereby improving the overall charge-separation efficiency. Furthermore, COFs designed with D–A configurations exhibit a markedly lower exciton binding energy compared to their symmetric counterparts.[91] The strong intraframework charge-transfer interactions shift the electron density from the donor units toward the acceptor domains upon photoexcitation, generating a built-in electric field that spatially separates charge carriers. This separation reduces the coulombic attraction between electrons and holes, thereby facilitating rapid exciton dissociation into free carriers. Consequently, D–A COFs display enhanced charge mobility, suppressed recombination,

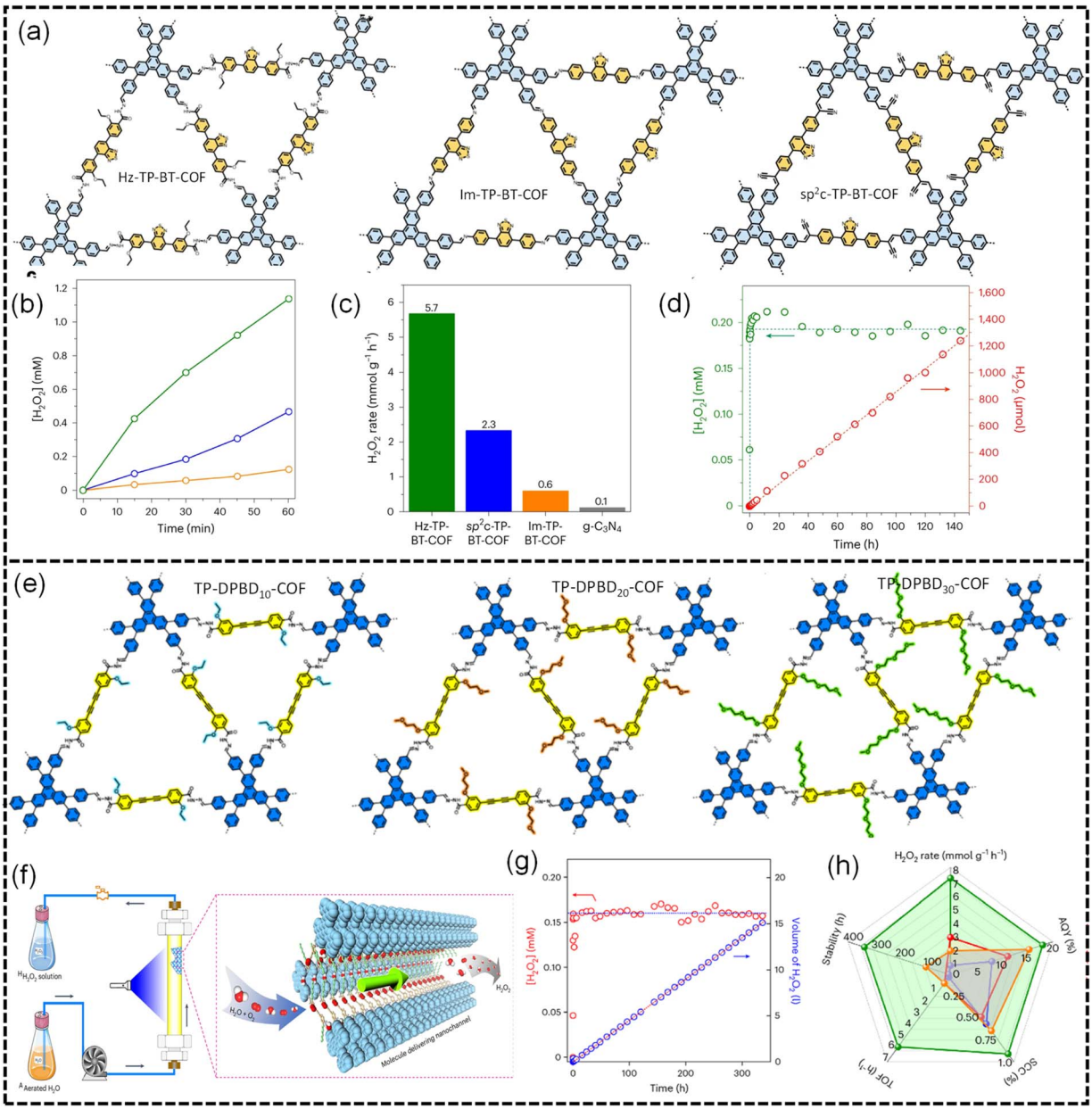

Fig. 3 (a) Structural representation of Hz-TP-BT-COF, Im-TP-BT-COF, and sp^{2}c-TP-BT-COF. (b) and (c) Comparison of photocatalytic H_2O_2 production of the synthesised catalyst with the benchmark g-C_3N_4. (d) Continuous H_2O_2 production up to 6480 mL within 140 h with Hz-TP-BT-COF. (Reproduced and reprinted with permission from ref. 93. Copyright 2024, Springer Nature.) (e) Structural representation of TP-DPBD$_{10}$-COF, TP-DPBD$_{20}$-COF, and TP-DPBD$_{30}$-COF. (f) Schematic representation of continuous photocatalysis in a flow reactor set up and WOR and ORR active sites in TP-DPBD$_{30}$-COF. (g) Schematic illustration of the production of H_2O_2 over 336 h through continuous photocatalysis in a flow reactor. (h) Graph for overall performance of TP-DPBD-COF towards H_2O_2 production. (Reproduced and reprinted with permission from ref. 94. Copyright 2024, Springer Nature.)

and improved photocatalytic efficiencies. Various D–A COFs have been reported recently that possess superior activity towards photocatalytic H_2O_2 production. For instance, considering the large π-conjugated structure, excellent light-harvesting abilities, and electron donor capabilities of pyrene moieties, Van Der Voort and their group reported the synthesis of four novel pyrene-based COFs.[92] The π-electron-rich pyrene acts as a donor, and its combination with an appropriate electron acceptor monomer has been found to be efficient towards H_2O_2 production, with a rate of 1242 μmol g^{-1} h^{-1} in the biphasic system (benzyl alcohol and water). The biphasic system has also been advantageous as it successfully inhibited the breakdown of H_2O_2 and facilitated efficient photocatalytic generation of H_2O_2.

Modulating the D–A property of COFs through linkage chemistry toward H_2O_2 production has been thoroughly examined by Jiang *et al.* Using a hexaphenyl triphenylene donor and a benzothiadiazole acceptor, they constructed hexavalent COFs

featuring hydrazone, imine, or cyano-vinylene linkages (Fig. 3a).[93] These materials possess sites that enable both the $2e^-$ ORR and $4e^-$ WOR, allowing concurrent formation of H_2O_2 and O_2. Among the linkages, the hydrazone bridge provided the most favourable characteristics, including superior stability, higher polarity, and abundant adsorption sites for water and oxygen (Fig. 3b). As a result, the Hz-TP-BT-COF delivered the highest H_2O_2 production rate (5.7 mmol g^{-1} h^{-1}), significantly outperforming the imine-linked (0.6 mmol g^{-1} h^{-1}) and vinylene-linked (2.3 mmol g^{-1} h^{-1}) analogues (Fig. 3c) without sacrificial agents alongside an apparent quantum yield (AQY) of 17.5% and a TOF of 4.2 h^{-1} at 420 nm. All synthesised COFs also show better performance towards photocatalytic H_2O_2 production compared to the benchmark g-C_3N_4 catalyst (Fig. 3c). The hexavalent hydrazone-linked COF also demonstrated the continuous photosynthesis of H_2O_2 in flow reactors with air-saturated water, reporting a record-high yield of 6480 mL of H_2O_2 over 144 h (Fig. 3d). Building on their earlier success with hydrazone-linked hexavalent COFs, the same group advanced their H_2O_2 photosynthesis strategy by designing a new series of hexavalent D–A COFs through precise tuning of π-frameworks and pore environments.[94] In this design, diphenylbutadiyne units replaced benzothiadiazole as the electron-accepting component. Besides serving as an active site for the $2e^-$ oxygen-reduction process, the hydrophobic diphenylbutadiyne motif discourages water adsorption and promotes spontaneous oxygen enrichment within the pores. The overall hydrophobicity of the COFs was further modulated by extending the ether side chains on the linker (Fig. 3e). Under visible light in pure water, the resulting COFs delivered H_2O_2 at rates of 7.2, 5.9, and 3.4 mmol g^{-1} h^{-1} for the TP-$DPBD_{30}$-COF, TP-$DPBD_{20}$-COF, and TP-$DPBD_{10}$-COF, respectively, consistent with the $2e^-$ ORR mechanism. When exposed to natural sunlight, the TP-$DPBD_{30}$-COF maintained a high activity of 3.4 mmol g^{-1} h^{-1}. Their practical potential was demonstrated in a continuous-flow reactor (Fig. 3f), which produced 15.1 L of H_2O_2 solution (0.16 mM) over two weeks/336 hours, highlighting the scalability of this COF-based system (Fig. 3g). The overall performance of TP-DPBD-COF has been shown through a radar plot (Fig. 3h), which highlights the production, solar-to-chemical conversion (SCC), AQY, stability, and turnover frequency (TOF) during photocatalytic H_2O_2 production. Tuning the D–A properties of a COF by introduction of a heteroatom is one of the well-known strategies. The thiophene-S units are well known for the ORR,

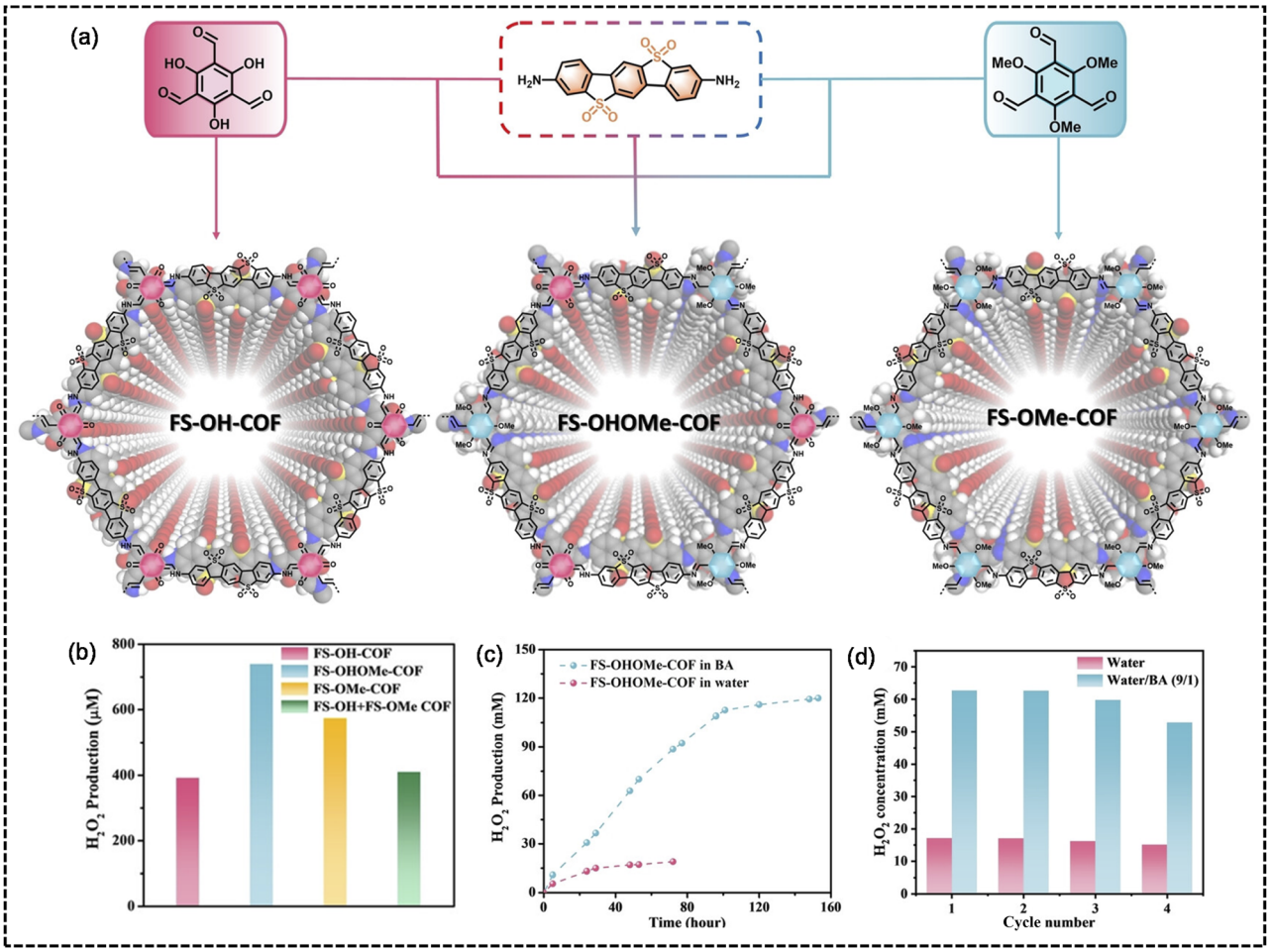

Fig. 4 (a) Synthesis scheme and structure of FS-COFs. (b) H_2O_2 production comparison of different FS-COFs. (c) Long-term stability of FS-OHOMe-COF in benzyl alcohol (BA) and water over 160 h. (d) Performance of recycled FS-OHOMe-COF in benzyl alcohol (BA) and water over four cycles. (Reproduced and reprinted with permission from ref. 99. Copyright 2024, Wiley-VCH GmbH.)

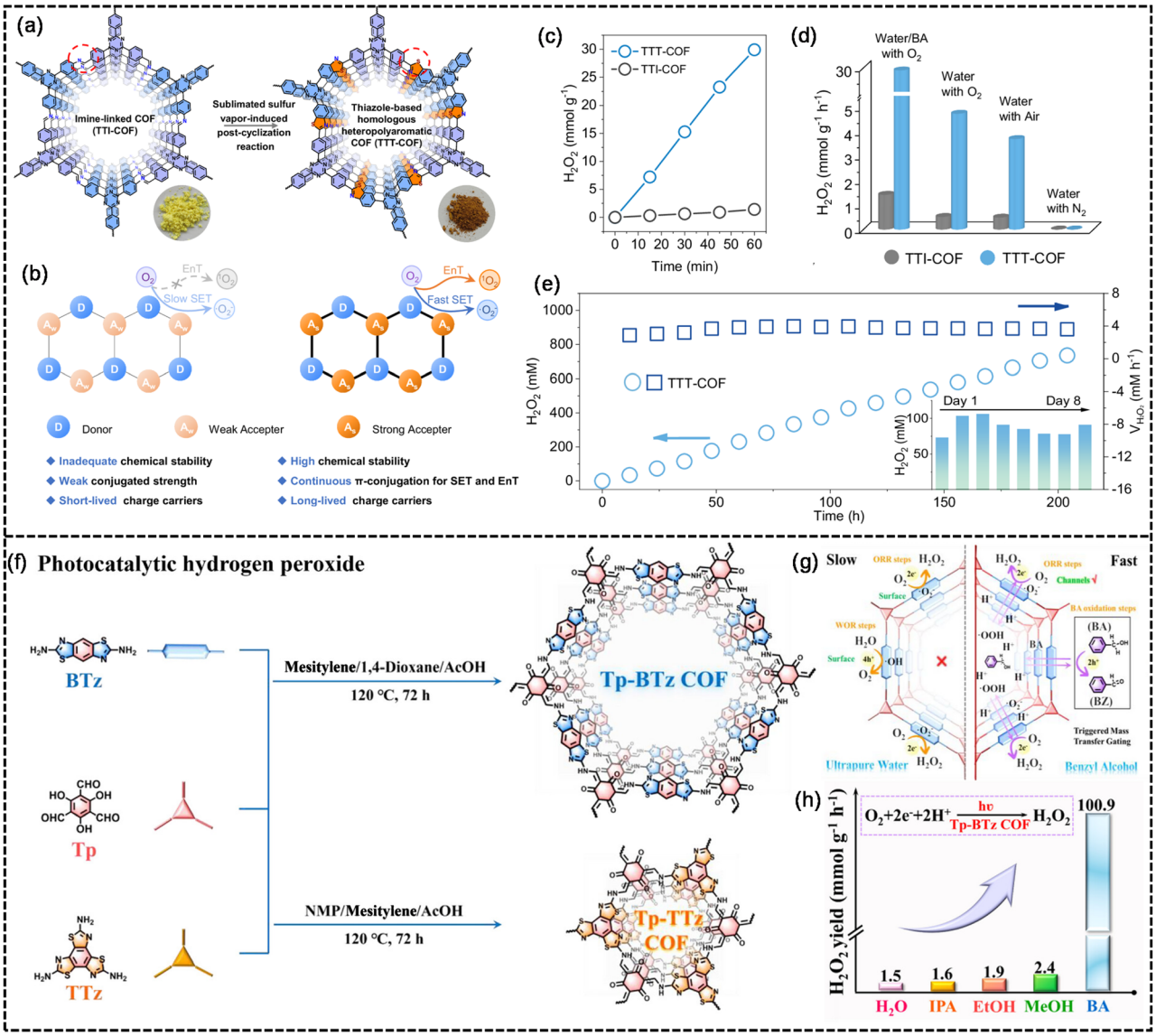

Fig. 5 (a) Schematic illustration of synthesis of thiazole-based homologous heteropolyaromatic COFs. (b) Representation of D–A moieties and the structural advantages of homologous heteropolyaromatic COFs. (c) Time-dependent photocatalytic activity of TTI-COF and TTT-COF for H_2O_2 production. (d) Photocatalytic H_2O_2 production comparison of TTI-COF and TTT-COF under different conditions. (e) Long-term H_2O_2 production of TTT-COF (inset: daily yield over eight days). (Reproduced and reprinted with permission from ref. 100. Copyright 2025, Springer Nature.) (f) Schematic illustration of the synthesis of Tp-BTz COF and Tp-TTz COF. (g) H_2O_2 production through mass-transfer gating (MTG). (h) Photocatalytic H_2O_2 production with Tp-BTz COF in different solvents. (Reproduced and reprinted with permission from ref. 101. Copyright 2025, Wiley-VCH GmbH.)

and its increased density within the COF enhances the ORR efficiencies.[95] The study performed by Wang *et al.* demonstrates the photocatalytic efficiency of the benzenetrithiophene (Btt)-based COF towards H_2O_2 production.[96] Three D–A COFs (TpaBtt, TapbBtt, and TaptBtt) were obtained by combining sulphur-rich Btt-based aldehyde with different types of triphenylamine derivatives (Fig. 4a). The synthesised COFs acquired a dual D–A structure that contributes an appropriate energy band position and a feasible intermediate anion towards H_2O_2 photosynthesis. Under visible light irradiation, TaptBtt with a triazine core produced H_2O_2 at a high rate of 2111 μM h^{-1} in pure water and air with an SCC of 0.296%. Similarly, Cao *et al.* reported that BBT-ACN COF-1, synthesised *via* Knoevenagel condensation between benzotristhiophene (BTT) and benzo[1,2-*d*;4,5-*d*′]bisthiazole (BBT), exhibited higher efficiency for photocatalytic H_2O_2 production than BBT-ACN COF-2, which was formed by coupling conjugated pyrene aldehyde with BBT.[97] Both COFs are sp^2-carbon-linked and have distinct D–A properties. BBT-ACN COF-1 features a D–A structure with BBT as the acceptor and BTT as the donor, whereas BBT-ACN COF-2 adopts a π–A architecture with pyrene as the π-unit and BBT as the acceptor. The use of thiophene-containing COFs for photocatalytic H_2O_2 production has also been reported by Yue *et al.*[98] By regulating the N-heteroatom in the framework, they have

synthesised two thiophene COFs (TD-COF and TT-COF). The regulation of N atoms has brought differences in their wettability, as the TD-COF is superhydrophilic and the TT-COF has a hydrophobic nature. Consequently, the TD-COF demonstrated H_2O_2 production of 4060 and 3364 μmol g^{-1} h^{-1} in deionised water and seawater, respectively, both of which are higher than those of the TT-COF. The mechanistic pathway revealed the photocatalytic production of H_2O_2 through the indirect $2e^-$ ORR and direct $2e^-$ WOR dual pathways, where thiophene is likely the photo-reduction unit, while benzene is the probable photo-oxidation unit. Beyond simple D–A assemblies in COFs, incorporating multiple D–A moieties has been shown to further enhance the photochemical efficiency. As shown by Shu *et al.*, the multiple donor–acceptor–acceptor (D–A–A) type FS-OHOMe-COF shows high efficiency for H_2O_2 production compared to FS-OH-COF and FS-Ome-COF, which have simple D–A units (Fig. 4a).[99] The sulfone group present within the COF linker serves as an active site and enhances stability by strengthening interlayer forces. Furthermore, compared to the pristine COF mixed ligand strategy, the synthesised FS-OHOMe-COF structure features extended π–π conjugation, long excited-state lifetime, low exciton binding energy, and high photostability. The H_2O_2 production rate of FS-OHOMe-COF was measured to be 1.0 mM h^{-1} in O_2-saturated water under visible light irradiation, which is higher than that of its pristine counterpart (Fig. 4b). Furthermore, an AQY of 9.6% at 420 nm and an SCC of 0.58% were also observed. Most reported photocatalysts generate only very low H_2O_2 concentrations, typically below 2 mM, far from the levels needed for practical use. In contrast, the FS-OHOMe-COF demonstrated steady and long-term accumulation of H_2O_2, achieving 19 mM in pure water after 72 h of irradiation. When benzyl alcohol was added, the concentration further increased to 120 mM after 153 hours, although part of this enhancement may arise from autocatalytic H_2O_2 formation associated with BA (Fig. 4c). Furthermore, the recyclability up to four cycles has been demonstrated by the FS-OHOMe-COF in both pure water and BA (Fig. 4d). The importance of the S-atom towards improving various properties of the COF photocatalyst has also been demonstrated by Cheng and coworkers.[100] They constructed a heteropolyaromatic TTT-COF by introducing thiazole units through a post-cyclisation reaction (Fig. 5a), which resulted in three key improvements (Fig. 5b): (i) markedly higher chemical stability, (ii) a fully extended π-conjugated framework that supports efficient single-electron and energy-transfer processes, and (iii) increased intramolecular polarity that strengthens the D–A character and promotes charge separation. Owing to these features, the TTT-COF shows far superior stability, conjugation, and photocatalytic performance compared to its imine-linked counterpart, TTI-COF. Consequently, using 10% benzyl alcohol, the TTT-COF produces H_2O_2 at a rate of 29.9 mmol g^{-1} h^{-1}, which is about 20 times higher than that of the imine-linked COF and superior to many state-of-the-art photocatalysts (Fig. 5c and d). The TTT-COF shows excellent durability, operating continuously for over 200 h with no significant loss in photocatalytic activity (Fig. 5e). Thiophene-based COFs are generally effective for H_2O_2 production. Notably, when the thiophene density was tuned using bis- and tris(thiazole) amines, the bis(thiazole)-based COF showed higher H_2O_2 production efficiency as reported by Qiao *et al.*[101] Two COFs—Tp-BTz and Tp-TTz (Fig. 5f)—were assessed their H_2O_2 production using a mass-transfer-gating (MTG) (Fig. 5g) strategy based on sacrificial agents. The MTG approach improves interfacial reactions by easing mass-transport constraints, increasing access to catalytic sites, scavenging photogenerated holes, and providing protons for downstream coupling steps. Introducing benzyl alcohol (BA) into the system activated a catalytic mode-switching behaviour, dramatically boosting performance. Under 10% BA and O_2-saturated conditions, the Tp-BTz COF delivered a record H_2O_2 production rate of 100.9

Table 1 Summary of representative D–A COF photocatalysts for H_2O_2 photosynthesis[a]

Sl. no.	Catalyst	Reaction conditions	Cat. dosage (mg) & solvent volume (mL)	H_2O_2 yield (μmol g^{-1} h^{-1})	AQY	SCC	Ref.
1	Py–Py COF	H_2O : BA (9 : 1)	10 mg & 20 mL	1242	4.5% @ 420 nm	—	92
2	Hz-TP-BT-COF	H_2O	3 mg & 15 mL	5700	17.5% @ 420 nm	—	93
3	TP-$DPBD_{30}$-COF	H_2O	2.5 mg & 15 mL	7200	18% @ 420 nm	0.91%	94
4	FS-OHOMeCOF	H_2O	10 mg & 20 mL	1100 μM h^{-1}	9.6% @ 420 nm	0.58%	99
5	TaptBtt-COF	H_2O	15 mg & 50 mL	1407	4.6% @ 450 nm	0.296%	96
6	BBT-ACN-COF-1	H_2O	5 mg & 50 mL	2500	3.12% @ 420 nm	—	97
7	TD-COF	H_2O and O_2	1 mg & 4 mL	4620	—	0.15%	98
8	TTT-COF	H_2O : BA (9 : 1)	5 mg & 45 mL	29 905	12% @ 400 nm	0.32%	100
9	Tp-BTz-COF	H_2O : BA (9 : 1)	5 mg & 20 mL	100 864	18% @ 420 nm	1.47%	101
10	COF-JLU92	H_2O : BA (1 : 1)	5 mg & 50 mL	39 283.3	15.4% @ 420 nm	2.35%	104
11	TT-T-COF	H_2O : BA (9 : 1)	5 mg & 25 mL	10 066	19.2% @ 420 nm	—	105
12	TMT-TT-COF	H_2O and O_2	10 mg & 30 mL	1952	—	—	102
13	Tf-TAPT-COF	H_2O and O_2	10 mg & 50 mL	2700	2.48% @ 420 nm	—	103
14	TTF-BT-COF	H_2O and O_2	5 mg & 10 mL	2.76 mM g^{-1} h^{-1}	11.19%@ 420 nm	0.49%	108
15	JUC-165	BAm, O_2 and ACN	5 mg & 10 mL	22 800	15.7%	1.09%	109
16	COF-2	Seawater	5 mg & 50 mL	6930	2.5% @ 420 nm	0.26%	111
17	TACOF-1-COOH	H_2O and O_2	2.5 mg & 18 mL	3542	5.7% @ 420 nm	0.55%	112

[a] Light irradiation: $\lambda > 420$ nm; BA: benzyl alcohol; BAm: benzyl amine; ACN: acetonitrile.

mmol g^{-1} h^{-1}, outperforming state-of-the-art photocatalysts and exhibiting 1.8-fold higher activity than the Tp-TTz COF (Fig. 5h). Also, the AQY of these COFs at 420 nm were calculated to be 18.0% and 16.5%, and the SCC efficiency evaluated using a solar simulator (AM 1.5G), yielded values of 1.47% and 0.72% for Tp-BTz COF and Tp-TTz COF, respectively. The sulfur-containing thiophene unit has moreover served as an electron-accepting site for the reduction of oxygen during H_2O_2 production. However, the electron donor strength of sulfur-containing moieties with the COF has also been explored and found to be efficient for H_2O_2 production. Van Der Voort and coworkers[102] report the synthesis of three D–A COFs (TMT-TT, TMT-N, and TMT-BT) by combining the triazine (TMT) unit with an aldehyde containing either thienothiophene (TT), naphthalene (N), or benzothiazole (BT) moieties, where the TT unit, with its two sulfur groups, exhibited the highest donor strength, followed by N and BT, with the electron-donating ability following the order: TT > N > BT. Therefore, with the D–A property in synthesised COFs, the H_2O_2 production rates in the O_2-purged pure water system were measured to be 1952, 1742, and 748 μmol g^{-1} h^{-1} for the TMT-TT-, TMT-N-, and TMT-BT-COF, respectively. The presence of nitrogen can also play a significant role in improving charge-carrier transport. As shown by Zhang *et al.*, the systematic regulation of nitrogen atoms within the framework modulates the electron-accepting capacity of COFs.[103] Regulating the nitrogen content in COFs leads to a well-defined D–π–A architecture. A higher density of nitrogen atoms in the heterocyclic units strengthens charge migration along the π-conjugated pathway. As a result, these COFs can promote the ORR through both the π-bridge and acceptor centres, while the WOR proceeds at the donor sites. This synergistic division of functions greatly enhances their overall efficiency in photocatalytic H_2O_2 generation. Notably, the Tf-TAPT-COF with a triazine unit can produce H_2O_2 at a rate of 2700 mmol g^{-1} h^{-1} from water and O_2. The major achievements of the D–A COF photocatalyst for H_2O_2 production has been highlighted in Table 1.

Apart from sulfur- and nitrogen-containing COFs, oxygen-rich frameworks have also demonstrated notable efficiency in H_2O_2 photosynthesis. In particular, benzotrifuran-based COF-JLU92 (Fig. 6a) featuring electron D–A characteristics with a hydrazone linkage has been reported by Zhang *et al.* for photocatalytic H_2O_2 production.[104] The partially separated D–A π-stacks in the benzotrifuran-based COF promote efficient charge separation and provide active sites for O_2 reduction and H_2O oxidation. Also, the 1D heteroatom-rich pores within the framework enhance water transport and lower the energy barrier for oxidation, enabling high H_2O_2 production rates of up to 9800 μmol g^{-1} h^{-1} from water and oxygen with an AQY of 8.7% at 450 nm. Varying the ratio of water to benzyl alcohol from 9 : 1 to 1 : 1, the H_2O_2 production rate drastically increased from 17 089 to 39 284 μmol g^{-1} h^{-1} (Fig. 6b). The high yield of H_2O_2 in BA was also recently reported with the nitroxyl radical decorated TT-T-COF.[105] Owing to the presence of an unpaired

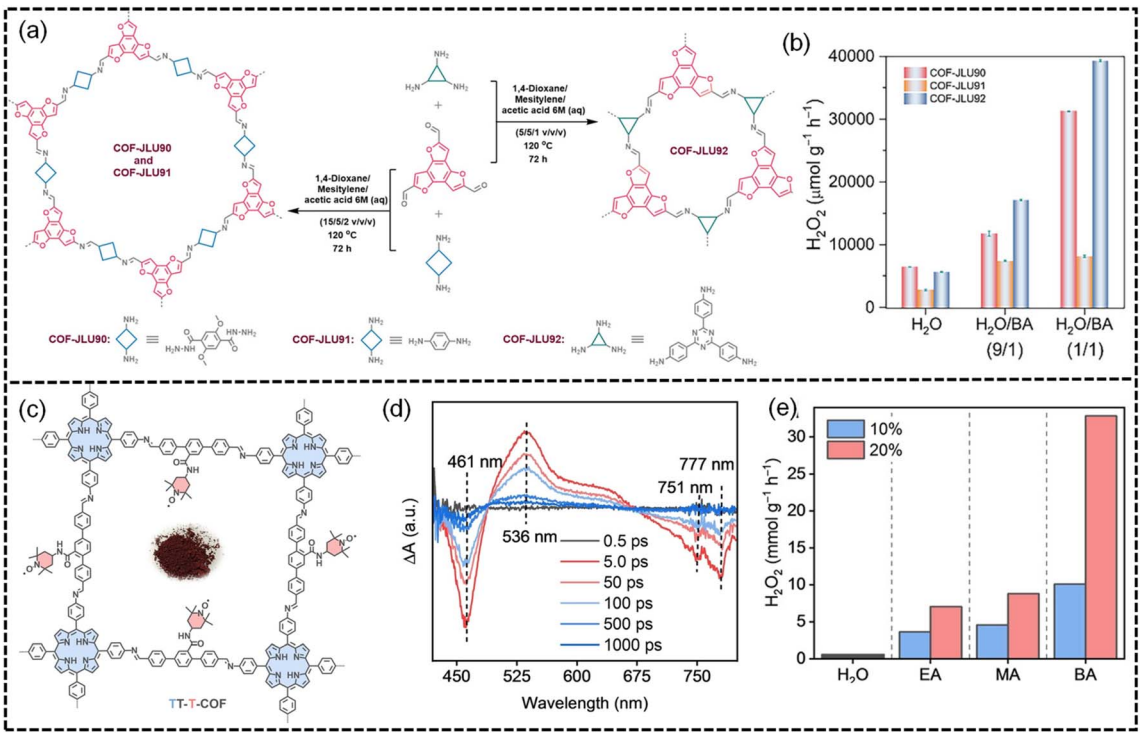

Fig. 6 (a) Schematic illustration of the synthesis of oxygen-rich COF-JLU. (b) Photocatalytic H_2O_2 production with COF-JLU in pure water and BA. (Reproduced and reprinted with permission from ref. 104 Copyright 2025, Wiley-VCH GmbH). (c) Schematic illustration of the synthesis of TEMPO decorated TT-T-COF. (d) Time-resolved kinetic measurements over a timescale of 0.5 ps to 1 ns revealing an intramolecular charge transfer process from TAPP to TPDA-TEMPO. (e) Photocatalytic H_2O_2 production with COF-JLU under different conditions. (Reproduced and reprinted with permission from ref. 105, Wiley-VCH GmbH).

electron in 2,2,6,6-tetramethylpiperidine-*N*-oxyl (TEMPO), it has been used as a nitroxyl radical mediator within the COF (Fig. 6c). The TEMPO-based COF TT-T-COF showed good crystallinity and had a Brunauer–Emmett–Teller (BET) surface area of 88.48 $m^2 g^{-1}$. The radical-based D–A architecture in the TT-T-COF promoted efficient separation of photogenerated electron–hole pairs, extends charge lifetimes, and enhances overall electron utilisation. However, COFs incorporated with TEMPO have band edges suitable for the ORR but not for the WOR ($2e^-$ or $4e^-$). Femtosecond transient absorption (fs-TA) studies reveal that the TT-T-COF undergoes ultrafast charge-separated state (CSS) formation (<5 ps) upon 365 nm excitation, as evidenced by characteristic ground-state bleaching (GSB, ~461 nm) and excited-state absorption (ESA, ~536 nm) signals (Fig. 6c). The rapid ESA evolution indicates efficient intramolecular electron transfer from the TAPP donor to the TEMPO acceptor within the D–A framework. Notably, incorporation of the redox-active TEMPO unit significantly prolongs the photogenerated electron lifetime (~671 ps), highlighting enhanced charge separation and carrier utilisation compared to conventional COFs. Time-resolved kinetic measurements excited at 365 nm over a timescale of 0.5 ps to 1 ns revealed an intramolecular charge transfer process from TAPP to TPDA-TEMPO (Fig. 6d). The photocatalytic H_2O_2 production rate of 10 066 and ~34 000 μmol g^1 h^1 in 10% and 20% BA under light irradiation >420 nm was noted for the TT-T-COF (Fig. 6d). *In situ* diffuse reflectance infrared Fourier transform spectroscopy (*in situ* DRIFTS) showed an increase in the intensity at 1178 cm^{-1}, 809 cm^{-1}, and 850 cm^{-1} corresponding to *OOH and HO–OH bonds. Combined theoretical and experimental (*in situ* DRIFTS) investigations demonstrate that the enhanced ORR activity and stability of the TT-T-COF arise from the participation of the nitroxyl radical (N–O$^\bullet$). The redox-active site modulates the local electron density and facilitates selective O_2 adsorption *via* a Yeager-type direct $2e^-$ ORR pathway.

COFs with different functional groups for photocatalytic H_2O_2 production

The profound opportunity to synthesise COFs with various functional groups represents one of the most important advancements in the field. Functional group modification in COFs involves altering the chemical groups attached to the framework to enhance its properties or tailor its functionality. Customisation of desired functional groups within the framework can enhance the electronic characteristics of COFs, boosting their ability to absorb visible light and improving the charge separation efficiency. The nature of substituents on COF linkers plays a decisive role in dictating both framework characteristics and catalytic behaviour. Fluorinated groups, for instance, can reshape the crystallinity, pore environment, and acid–base properties, ultimately influencing oxygen-reduction pathways and light-driven activity.[106] In contrast, hydroxyl functionalities help capture photogenerated holes and suppress charge-recombination events, thereby improving the durability.[107] Cyanide units steer the oxygen activation pathway by favouring the generation of singlet oxygen ($^1O_2$) instead of superoxide species.[113] Additionally, the functional modifications can increase the stability of COFs under various operational conditions, ensuring reliable performance over time. Moreover, the strategic addition or removal of groups facilitates efficient charge transfer, minimising the recombination of electron–hole pairs and increasing the production of H_2O_2.

The functionalization of COFs with heteroatoms (N, O, S, *etc*.) has a profound effect that enhances the photocatalytic activity.[110] The presence of heteroatoms alters the electronegativity of adjacent carbon atoms, potentially making these carbon atoms catalytically active as well. Moreover, the inherent hierarchy in electronegativity among the three heteroatoms significantly influences the resulting framework characteristics. In addition to the type of heteroatom present, its density and spatial arrangement within the framework also play critical roles in modulating the charge-transfer dynamics of COFs.[114] Some studies show that COFs containing nitrogen-rich triazine, heptazine, can rationally induce the electrophilicity and results in more efficient ORR, forming H_2O_2.[115] The effect of different amounts of nitrogen in COFs on photocatalytic H_2O_2 production has been demonstrated by Zhang *et al.*[116] Two photoactive COFs (COF-JLU51 and COF-JLU52) were synthesised *via* a Schiff base condensation reaction between [1,2,4]-triazolo-[1,3,5]-triazine (TTT) and triphenylbenzene as a building block. COF-JLU51 and COF-JLU52 have a nitrogen content of 23.01 wt% and 26.79 wt%, respectively. TTT moieties have strong electron-withdrawing ability, and their combination with electron-donating triphenylbenzene imparts optimum electron D–A characteristics to COF-JLU51. Consequently, the photochemical activity of COF-JLU51 is higher than that of COF-JLU52. The H_2O_2 production rates of 4260.3 μmol g^{-1} h^{-1} and 3033.3 μmol g^{-1} h^{-1} were observed for COF-JLU51 and COF-JLU52, respectively. However, in a biphasic system containing water and benzyl alcohol in a ratio of 9 : 1, COF-JLU52 could produce H_2O_2 at a rate of 7624.7 μmol g^{-1} h^{-1} with an AQY of 18.2% at 420 nm. The SCC efficiency of COF-JLU51 and COF-JLU52 was reported to be 0.19% and 0.12%, respectively. Similarly, the influence of thiophene and high nitrogen content in the COF towards enhanced photocatalytic activity has been reported by Zeng and co-authors by demonstrating the N-site engineering strategy on the thiophene-containing COF.[117] Through the Schiff base condensation of various N-heterocycle (pyridine, pyrimidine, and triazine) units with a thiophene building unit, five COFs were synthesised. Among them, the TTA-BT-COF and TTA-TF-COF were multicomponent COFs as both triphenyltriazine aldehyde and triphenyl triazine-NH_2 reacted with the thiophene moiety. The multicomponent TTA-TF-COF, which has more N-sites, was efficient towards photocatalytic H_2O_2 production with a maximum rate of 3343 μmol g^{-1} h^{-1} in pure water and air. These results suggest a direct correlation between the nitrogen atom density in the COF and photocatalytic H_2O_2 production. However, recent studies indicate that not only the nitrogen density but also its spatial positioning within the framework plays a crucial role in governing the efficiency of H_2O_2 formation. The effect of adjacent N in the COF skeleton towards photocatalytic H_2O_2 production has been

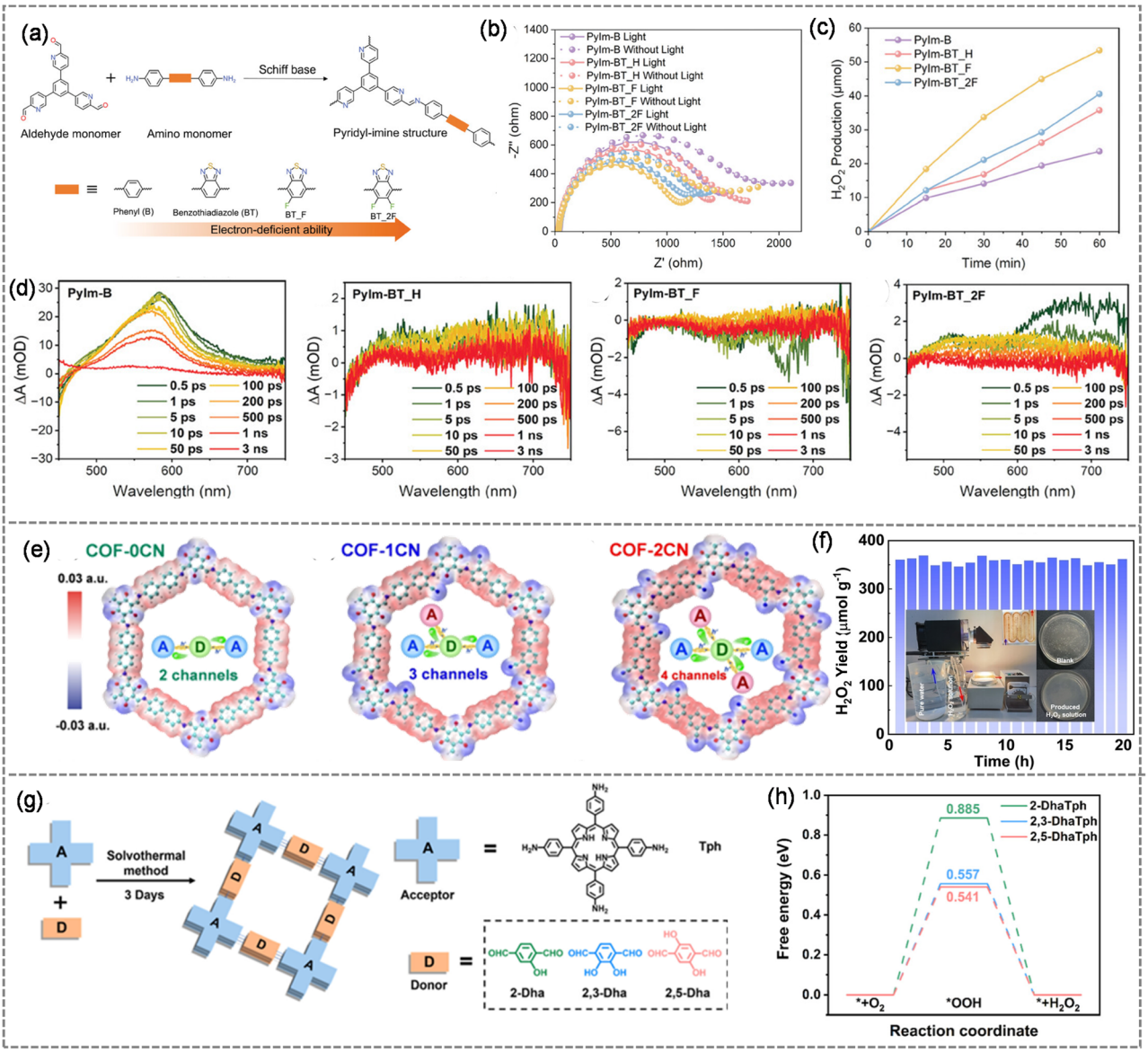

Fig. 7 (a) Synthetic pathway of the pyridyl-imine COF and the structure of synthesised COFs with regulated F-atoms. (b) Nyquist plots of PyIm-COFs. (c) Time-dependent photocatalytic H_2O_2 production with the pyridyl-imine COF. (d) Fs-TSA plots of PyIm-COFs. (Reproduced and reprinted with permission from ref. 119. Copyright 2025, Wiley-VCH GmbH.) (e) Structure of cyanide decorated COFs, highlighting their D–A moieties. (f) Long-term photocatalytic H_2O_2 production using COF-2CN *via* flow catalysis, and the inset shows the reaction setup for flow catalysis. (Reproduced and reprinted with permission from ref. 120. Copyright 2023, Wiley-VCH GmbH.) (g) Schematic illustration of the synthesis of three hydroxyl-functionalized D–A COFs. (h) The Gibbs free energy spectra of the $2e^-$ ORR process on hydroxyl-functionalized D–A COFs. Reproduced and reprinted with permission from ref. 121. Copyright 2025, American Chemical Society.

demonstrated by Zhao and co-authors.[118] Three COFs, namely, BD-COF, Bpy-COF and PyIm-COF, were synthesised *via* a Schiff base condensation reaction by reacting pyrene-NH_2 with various aldehydes that contain either 1,1′ biphenyl (BD) or 2,2′ bipyridine (Bpy) or 3,3′ bipyridine (PyIm). The photocatalytic H_2O_2 production was evaluated using pure water under Xe light irradiation without any sacrificial agent. The H_2O_2 production with the PyIm-COF was found to be 5850 μmol g^{-1} h^{-1}, which is the highest amongst Bpy-COFs (3060 μmol g^{-1} h^{-1}) and BD-COFs (670 μmol g^{-1} h^{-1}). The AQY and SCC of PyIm-COF were 3.70% at 420 nm and 0.28% under AM 1.5 G simulated sunlight. The theoretical investigation shows that the pyrimidine unit is responsible for the enhanced separation of the photogenerated electron–hole pair, which prevents the recombination and strong adsorption of O_2 on the adjacent N-atoms.

It is well known that H_2O_2 formation proceeds through a $2e^-$ ORR pathway; the electrophilicity of the COF and the nature of its oxygen-adsorption sites are crucial determinants of its photocatalytic efficiency. Rationally introducing electrophilic functional groups such as fluorine, vinylene, and cyanide has also been shown to improve the photocatalytic H_2O_2 generation performance. For instance, Zhao *et al.*[119] have synthesised

pyridyl-imine functionalized D–A COFs (PyIm-B and PyIm-BT_X, where X = H, F or 2F), by regulating the electronegative fluorine atoms (Fig. 7a). The different F-atoms within the framework regulated the electron-deficient nature of the acceptor moiety. The electrochemical impedance spectra (Fig. 7b) show the lowest electrochemical impedance and smallest charge-transfer resistance for PyIm-BT_F, followed by PyIm-BT_2F, PyIm-BT_H, and PyIm-B. These results demonstrate that tuning the D–A configuration effectively modulates photoinduced charge separation and transport in PyIm-COFs, with PyIm-BT_F showing superior optical and electrochemical performances due to its monofluorinated benzothiadiazole unit. Consequently, PyIm-BT_F achieved the highest H_2O_2 production rate of 5342 μmol g^{-1} h^{-1}, surpassing both PyIm-BT_H (3577 μmol g^{-1} h^{-1}) and PyIm-BT_2F (4061 μmol g^{-1} h^{-1}) (Fig. 7c). The COF exhibited good structural integrity and sustained photoefficiency during stability tests conducted for up to 10 h. The photoexcited carrier dynamics were evaluated through femtosecond transient absorption spectroscopy (fs-TAS), where all PyIm-COFs displayed ultrafast excited-state absorption (ESA) signals after photoexcitation (Fig. 7d). PyIm-B exhibited a strong ESA band at 580 nm, indicating a high excited-state population. In contrast, BT-functionalized COFs (PyIm-BT_H, PyIm-BT_F, and PyIm-BT_2F) showed negative peaks at 740 nm, attributed to photoinduced emission from interfacial charge transfer between Py and BT units. These results confirm that the D–A architecture enhances charge transfer and suppresses electron–hole recombination. Although PyIm-BT_2F contains more fluorine atoms, the superior activity of PyIm-BT_F suggests that an optimal, rather than excessive, electrophilic character is essential for efficient H_2O_2 generation. Similarly, regulation of the cyanide moiety within the framework has been reported by Tong *et al.*, who synthesised three ketoenamine-based D–A COFs by regulating the number of CN groups (COF-*x*CN, where $x = 0, 1, 2$) (Fig. 7e).[120] The H_2O_2 photosynthesis performance of synthesised COFs in pure water and O_2 under visible light

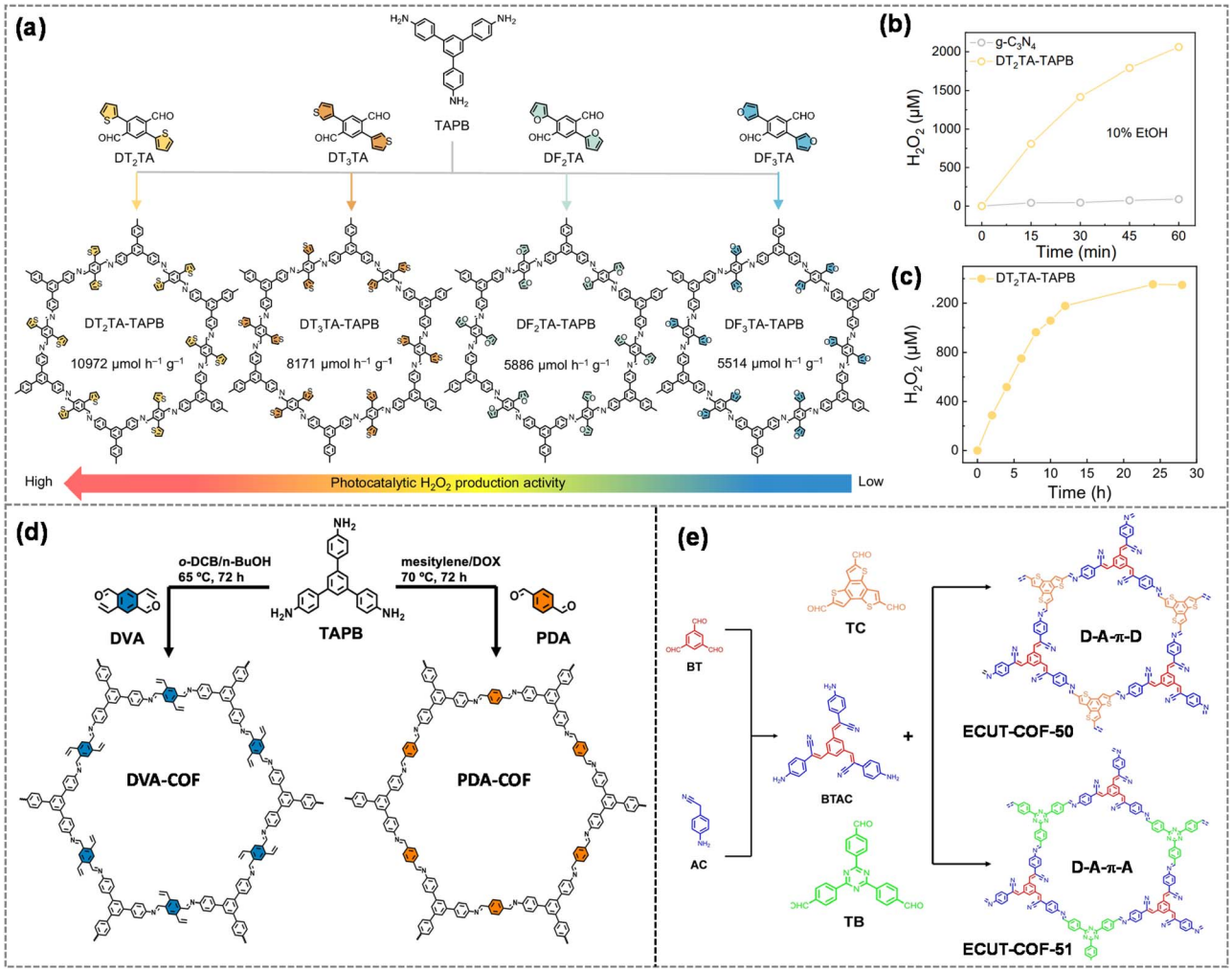

Fig. 8 (a) Schematic route for the synthesis of thiophene- and furan-decorated imine COFs. (b) Photocatalytic H_2O_2 production comparison of DT_2TA-TAPB and g-C_3N_4 photocatalysts. (c) Long-term photocatalytic H_2O_2 production plot with DT_2TA-TAPB. (Reproduced and reprinted with permission from ref. 122. Copyright 2025, Springer Nature.) (d) Schematic route for the synthesis of vinylene decorated COFs. (Reproduced and reprinted with permission from ref. 123. Copyright 2024, Wiley-VCH GmbH.) (e) Synthetic scheme for the synthesis of cyanide-functionalized D–A COFs. (Reproduced and reprinted with permission from ref. 124. Copyright 2024, Wiley-VCH GmbH.)

irradiation was studied, which showed an increasing production with increasing number of CN functional groups. Consequently, the highest production for COF-2CN (1601 mmol g^{-1} h^{-1}) was observed, followed by COF-1CN (573 mmol g^{-1} h^{-1}), and lastly COF-0CN (194 mmol g^{-1} h^{-1}). The remarkable efficiency of COF-2CN can be attributed to the presence of two CN groups within the framework, which activate the adjacent carbon atom, facilitating the formation of the key *OH intermediate that lowers the energy barrier for the rate-determining two-electron water oxidation step in H_2O_2 photosynthesis. H_2O_2 was also produced efficiently and stably at a rate of ≈716 μmol g^{-1} h^{-1} under visible-light irradiation over a 20 h photocatalytic operation in a continuous-flow reactor (Fig. 7f). The effect of regulating the number and position of hydroxyl (–OH) groups on photocatalytic H_2O_2 production has been investigated in porphyrin-based COFs by Liu *et al.* (Fig. 7g).[121] Three COFs, namely 2-DhaTph, 2,5-DhaTph, and 2,3-DhaTph, were synthesised, in which the porphyrin unit acts as the electron acceptor, while the hydroxyl-functionalized moiety serves as the electron donor. An increase in the number of –OH groups enhance the donor ability of the COFs, leading to improved photoefficiency. However, compared to 2,3-DhaTph with *para*-positioned hydroxyl groups, 2,5-DhaTph with *para*-positioned –OH groups exhibit higher crystallinity and better exposure of catalytically active sites. Consequently, 2,5-DhaTph showed a H_2O_2 production rate of 2103.1 μmol h^{-1} g^{-1}, 1.1 times higher than that of 2,3-DhaTph. DFT analysis revealed that 2,5-DhaTph exhibits the lowest energy barrier (0.541 eV) for the formation of the *OOH intermediate, which is the rate-determining step, compared to the other COFs (Fig. 7h). Similarly, incorporating thiophene and furan isomeric units into the side chains of COFs enables precise tuning of COF electronic structures, and photocatalytic activity was demonstrated by Tang *et al.*[122] Four COFs, namely DT_2TA-TAPB, DT_3TA-TAPB, DF_2TA-TAPB, and DF_3TA-TAPB, were synthesised by reacting 1,3,5-tris(4-aminophenyl)benzene (TAPB) and terephthaldehyde substituted with 2 or 3 thiophene or furan moieties (Fig. 8a). Thiophene isomer-functionalized COFs exhibited superior performance relative to their furan isomer-based counterparts, which can be attributed to a more favourably matched D–A architecture. Consequently, DT_2TA-TAPB achieved the H_2O_2 production of 10 972 and 8587 μmol g^{-1} h^{-1} in 10% ethanol and pure water, which are ∼23 and ∼41 times greater than those of benchmark g-C_3N_4 (Fig. 8b). The DT2TA-TAPB-COF also showed stable photocatalytic H_2O_2 production for 24 h under simulated natural conditions, followed by a steady plateau up to 28 h, indicating a dynamic formation-decomposition equilibrium (Fig. 8c).

The vital challenges in COFs, such as low charge-generation and -transfer efficiencies, as well as rapid charge recombination that severely hindered the H_2O_2 production, have also been addressed by anchoring the vinyl moieties within the COF skeleton. The recent work from Chen and group demonstrates the synthesis of two imine-based COFs, one decorated with a vinyl group (DVA-COF) and another without any functionalization (PDA-COF) (Fig. 8d).[123] Owing to the excellent π–π conjugated structure, abundant electronics, non-polar nature, and other characteristics of the vinyl group, the role of intralayer electron delocalisation and interlayer π–π stacking in charge generation and separation has been rationally studied. The photocatalytic performance of the synthesised COF towards H_2O_2 production has been studied in the two-phase water/benzyl alcohol (9 : 1, v/v) system. The vinyl containing DVA-COF could produce H_2O_2 photocatalytically at a rate of 84.5 μmol per h per 10 mg photocatalyst, which is higher than that of the non-functionalised PDA-COF (8.6 μmol per h per 10 mg photocatalyst). The AQY and SCC efficiency values for the DVA-COF were calculated to be 2.84% at 420 nm and ∼0.08% under AM 1.5G simulated sunlight, respectively. On investigation of the catalytic pathway, the vinyl group present in the COF was found to inhibit photogenerated electron–hole recombination. The DVA-COF showed excellent cycling stability over five irradiation cycles, with no noticeable changes in PXRD patterns. Continuous H_2O_2 production was maintained under light irradiation for 16 h, accompanied by nearly equimolar formation of H_2O_2 and benzaldehyde. The photo efficiency of COFs could also be rationally enhanced by functionalizing with various D–A moieties. For instance, Luo *et al.*[124] synthesised COFs by integration of the π-accepting cyanide functional group that acts as a π electron acceptor. Its combination with donor thiophene and acceptor triazine monomers yielded D–A–π–D (ECUT-COF-50) and D–A–π–A (ECUT-COF-51) frameworks, respectively (Fig. 8e). Interestingly, the D–A–π–D COF demonstrated significantly higher efficiency than the D–A–π–A counterpart, achieving a remarkable H_2O_2 production rate of 4742 μmol h^{-1} g^{-1} using only air and water. Furthermore, ECUT-COF-50 maintained consistent H_2O_2 production over 80 h of continuous operation without performance loss. Similarly, as hydroxyl moieties are known to enhance the hydrophilicity of COFs, Shen *et al.* demonstrated that synergistic functional group modification, which tunes electronic conjugation and intramolecular polarity, significantly enhances light absorption, charge separation/transfer, and interfacial water–oxygen affinity.[125] This was achieved by synthesising a series of imine-linked COFs (TT-COF-X) with electronically tunable substituents (X = –H, –OMe, –OH, –Br) (Fig. 9a). Photocatalytic H_2O_2 production proceeds *via* a dual-channel pathway involving $2e^-$ ORR and WOR pathways, highlighting 100% atom utilisation. Among the series, hydroxyl-functionalized TT-COF-OH delivered the highest H_2O_2 production rate (3406.25 μmol g^{-1} h^{-1}) (Fig. 9b) and an impressive AQY of 8.1%. It also exhibited efficient performance over a wide pH range and in real water matrices. fs-TA spectroscopy (460–800 nm) was used to probe the ultrafast exciton dissociation dynamics. The results show that a polarity-induced built-in electric field (BIEF) in TT-COF-OH enables a BIEF-mediated shallow trap state, facilitating exciton dissociation and suppressing electron–hole recombination, leading to a much longer average lifetime (τ_{avg} = 475.76 ps) compared to TT-COF-H (τ_{avg} = 76.32 ps). These results further reveal that the exciton binding energy (E_b) and charge-transfer resistance (R_{ct}) decrease with increasing BIEF intensity (Fig. 9c). A stronger BIEF introduces a trap state that promotes exciton dissociation and charge transport, thereby enhancing the exciton dissociation efficiency (σ_d). Mechanistic studies reveal that hydroxyl-induced electronic microenvironment regulation enhances conjugation for

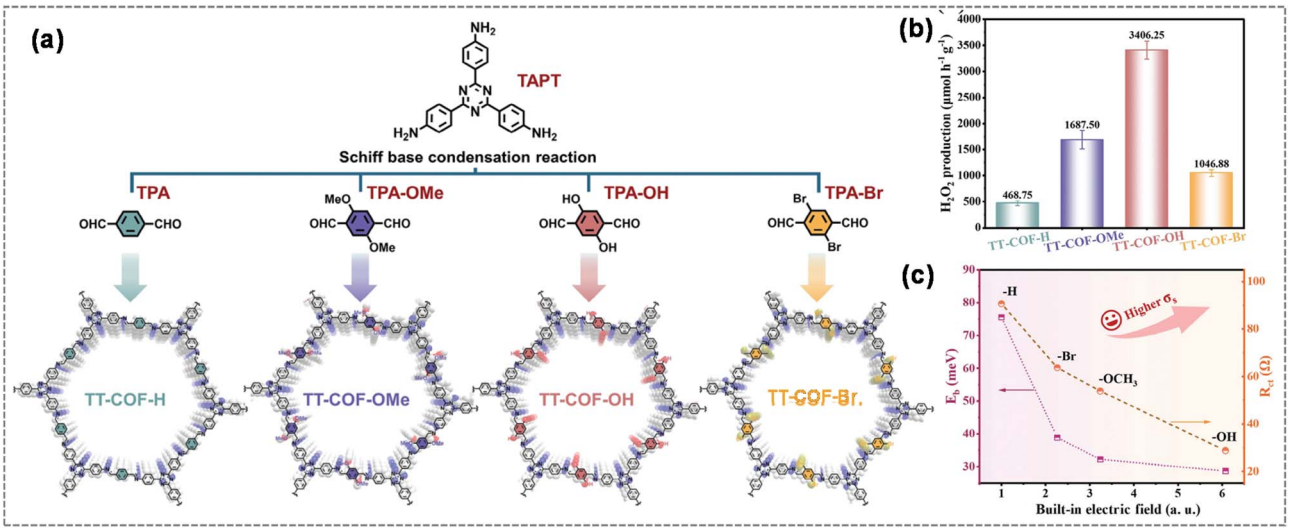

Fig. 9 (a) Synthetic route for the synthesis of different functionalized imine COFs. (b) Photocatalytic H_2O_2 production comparison of functionalized COFs. (c) Built-in electric field (BIEF) plot of functionalized imine COFs. (Reproduced and reprinted with permission from ref. 125. Copyright 2025, Wiley-VCH GmbH.)

improved light harvesting, generates a 6.01-fold stronger BIEF to accelerate exciton dissociation and charge transport, and promotes oxygen/water adsorption with faster interfacial electron transfer. The Schiff base condensation reaction between amines and aldehydes remains one of the most widely utilised techniques for synthesising COFs. However, a significant challenge encountered by researchers is the frequent hydrolysis of amine bonds formed through the condensation reaction, which leads to structural collapse. Notably, Bannerjee and co-workers addressed this challenge and markedly enhanced the stability of Schiff base-condensed COFs by using triformylphloroglucinol (Tp) as an aldehyde linker.[126] They demonstrated that the hydroxyl group adjacent to the formyl group in Tp facilitates irreversible keto–enol tautomerism, thereby inhibiting the hydrolysis of the amine bond. Although the availability of three hydroxyl groups in Tp provides stability to the COF, its irreversible tautomerism decreases the crystallinity of the COF and can hinder photocatalytic activity. Due to this, the decrease of the number of hydroxyl groups in Tp aldehyde has allowed for the partly reversible keto–enol tautomerism that enhances both the stability and crystallinity of the COF.[127,128] The effect of the number of hydroxyl groups on its photocatalytic activity has been recently explored by Kong *et al.*, and they reported the synthesis of four imine-based COFs (0H, 1H, 2H, and 3H-COF, Fig. 10a) with different numbers of hydroxyl functional groups (0–3).[129] The degree of keto–enol tautomerism in imine-linked COFs can be controlled by varying the number of –OH groups attached to the aldehyde precursors. This adjustment significantly influences the crystallinity and photocatalytic properties of the COFs. Among the four COFs studied, 1H-COF, which contains a single –OH group, exhibits the most ordered structure and the highest conjugation due to the predominant tautomerization. Additionally, the rearrangement between enol–imine and keto–amine linkages optimises its optical absorbance, electron push–pull effect, and water stability. This dynamic charge redistribution suppresses electron–hole recombination, resulting in a longer excited-electron lifetime for the 1H-COF, as confirmed by time-resolved photoluminescence (TRPL) measurements (Fig. 10b). As a result, the 1H-COF can produce H_2O_2 with a rate of 44.5 μmol h^{-1} in the presence of 10% IPA solution (Fig. 10c). The effect of keto–enol tautomerism on the photocatalytic efficiency of imine-based COFs has also been studied by Long and co-workers.[130] Intrigued by the role of anthraquinone moieties in mass production of H_2O_2, they have synthesised an imine-based COF (TpAQ-COF) by the Schiff base condensation reaction between 2,6-diaminoanthraquinone (AQ) and triformylphloroglucinol (Tp) (Fig. 10d). The anthraquinone moieties serve as the active sites for the selective two-electron ORR, promoting the separation and migration of photogenerated charges. Interestingly, the keto–amine form of the COF was found to be more efficient for H_2O_2 production than the enol–imine form, and by adjusting the condensation time, researchers could vary the ratio of the two forms, with the keto–amine form promoting better D–A coupling structures that favour the migration of photogenerated carriers. Consequently, the TpAQ-COF could produce H_2O_2 at the rate of 420 μmol g^{-1} h^{-1} with an AQY of 7.2% at 420 nm. The COF also showed good stability upon prolonged irradiation for 12 h, with steady production of H_2O_2. Motivated by the result, the same group has extended the research through synthesising a keto-form anthraquinone COF (K_f COF) *via* a mechanochemical route (Fig. 10e).[131] The K_f-COF could form H_2O_2 in alkaline medium (pH = 13) at a rate of 4784 μmol g^{-1} h^{-1}. At pH 13, K_f-AQ exhibited the highest H_2O_2 formation rate constant ($k_f = 31.39$ μM min^{-1}), while maintaining a moderate decomposition rate constant ($k_d = 0.031$ μM min^{-1}) (Fig. 10f). The highly alkaline environment promoted the formation of $OH^-(H_2O)_n$ clusters, which were adsorbed onto the keto moieties of the framework. This adsorption significantly lowered the energy barrier for hydrogen abstraction, facilitating their

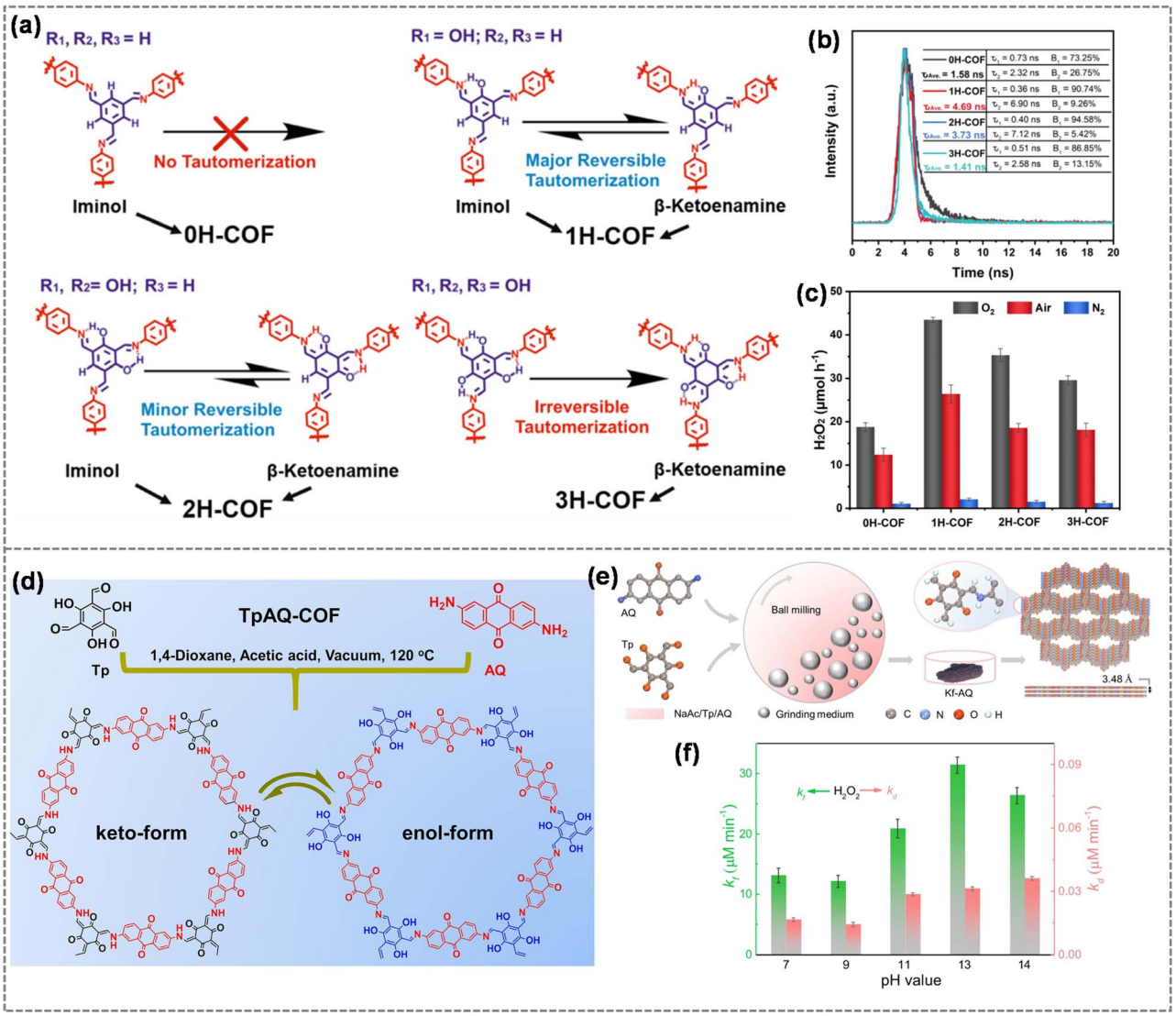

Fig. 10 (a) Illustration of iminol-to-ketoenamine tautomerism in XH-COFs *via* proton transfer. (b) TRPL spectra of ketoamine COFs. (c) Comparison of photocatalytic H_2O_2 production of ketoamine COFs. (Reproduced and reprinted with permission from ref. 129. Copyright 2023, Elsevier.) (d) Structure of the TpAQ-COF in its keto and enol forms. (Reproduced and reprinted with permission from ref. 130. Copyright 2023, Elsevier.) (e) Mechanochemical synthetic route for the Kf-AQ COF. (f) H_2O_2 formation and decomposition plot using the Kf-AQ COF in different pH solutions. (Reproduced and reprinted with permission from ref. 131. Copyright 2024, Springer Nature.)

dissociation into O_2 and active hydrogen species. The generated hydrogen subsequently reduced anthraquinone to anthrahydroquinone, which was then re-oxidised by O_2 to yield H_2O_2. The integration of the quinone unit in the COF has also demonstrated H_2O_2 production in the full pH range (pH 1–13), as demonstrated by Li *et al.*[132] Two COFs, Por-HQ-COF and Por-BQ-COF, have been synthesised from *p*-hydroquinone (HQ) and *p*-benzoquinone (BQ) moieties. Interestingly, under alkaline conditions, the Por-HQ-COF undergoes conversion to the Por-BQ-COF (Fig. 11a). In this transformed structure, the imidazole nitrogen in the Por-BQ-COF facilitates water molecule dissociation to generate protons and enhances the ORR, resulting in a notable H_2O_2 production rate of up to 1525 μmol g^{-1} h^{-1}. Furthermore, the Por-BQ-COF showed the k_f of 13.55 μM min^{-1} and the lowest k_d of 0.0165 μM min^{-1} at pH 13. The efficiency of quinoline-linked COFs has also been widely explored by Dong *et al.* Benzo[*f*]quinoline-linked COFs have been synthesised through a one-pot, three-component [4 + 2] cyclic condensation strategy.[133] This approach involves the reaction of aldehydes and aromatic amines using triethylamine as a readily accessible vinyl source, resulting in the formation of stable and highly photoactive benzo[*f*]quinoline-linked COFs (Fig. 11b). The high crystallinity, improved stability, and strong light-harvesting ability of these COFs contributed to their excellent performance in H_2O_2 photosynthesis. As a result, B[*f*]QCOF-1 exhibited exceptional photocatalytic activity, reaching an H_2O_2 production rate of 9025 μmol g^{-1} h^{-1} in pure water (Fig. 10e) without any sacrificial agent, accompanied by nearly equimolar formation of H_2O_2 and benzaldehyde. The major achievements of the

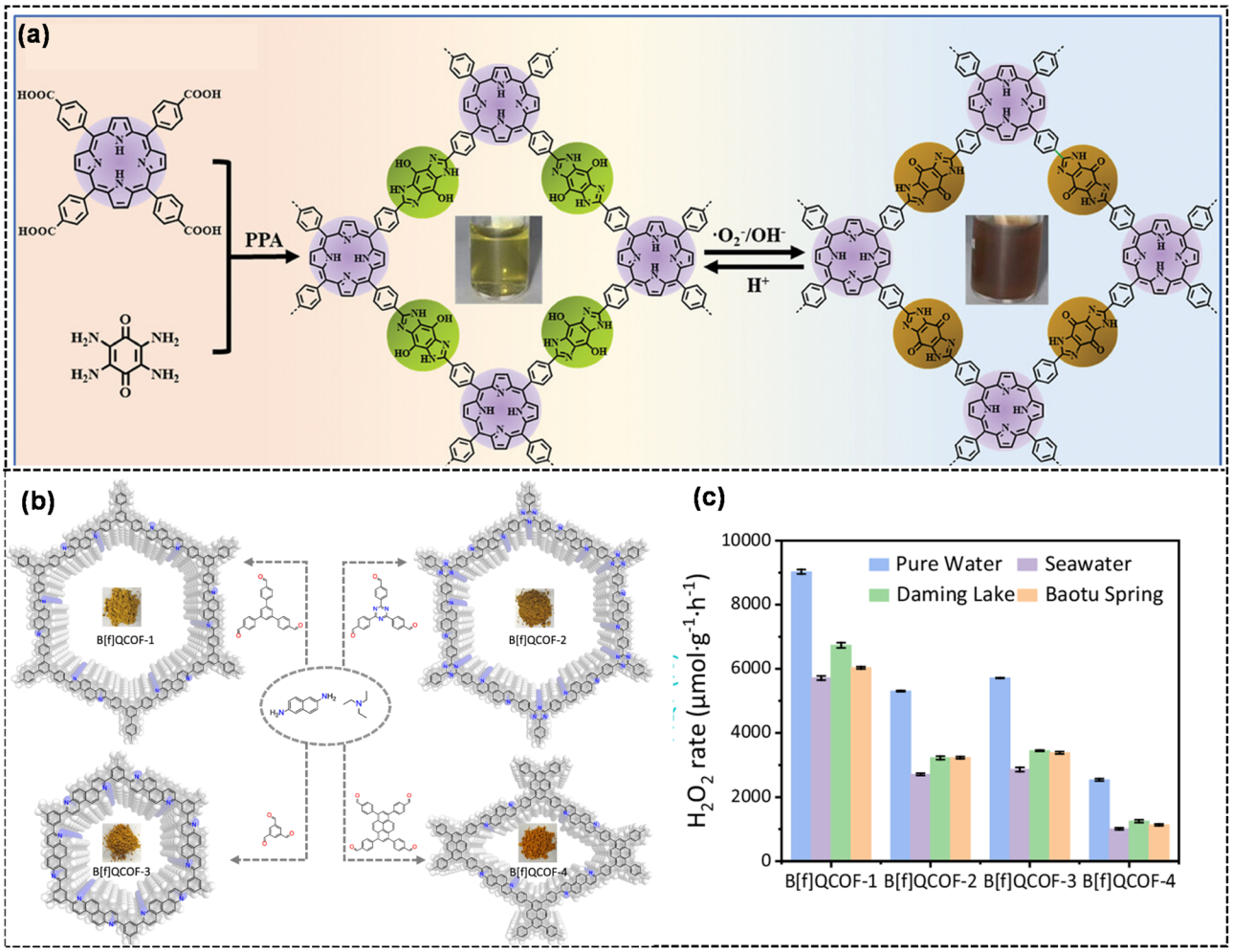

Fig. 11 (a) Synthetic route for the Por-HQ-COF and Por-BQ-COF. (Reproduced and reprinted with permission from ref. 132. Copyright 2024, Wiley-VCH GmbH.) (b) Synthesis scheme and structure of benzo[*f*]quinoline-linked COFs. (c) Photocatalytic H_2O_2 production with benzo[*f*] quinoline-linked COFs using different water samples. (Reproduced and reprinted with permission from ref. 133. Copyright 2024, Springer Nature.)

Table 2 Summary of the representative functionalization of COF photocatalysts for H_2O_2 photosynthesis[a]

Sl. no.	Catalyst	Reaction conditions	Dosage (mg) & volume (mL)	H_2O_2 yield (μmol g^{-1} h^{-1})	AQY	SCC	Ref.
1	HEP-TAPT-COF	H_2O and O_2	50 mg & 100 mL	87.50 μmol h^{-1}	—	0.65%	115
2	COF-JLU51	H_2O and O_2	5 mg & 50 mL	3388.3	6.4%	0.19%	116
3	TTA-TF-COF	H_2O	1 mg & 8 mL	3343	4.1% @ 420 nm	0.13%	117
4	PyIm-COF	H_2O	10 mg & 50 mL	5850	3.70% @ 420 nm	0.28%	118
5	PyIm-BT_F	H_2O : IPA = 9 : 1	10 mg & 50 mL	5342	2.7% @ 420 nm	—	119
6	COF-2CN	H_2O and O_2	12.5 mg & 50 mL	1601	6.8% @ 459 nm	0.6%	120
7	2,5-DhaTph	H_2O : EtOH = 9 : 1	10 mg & 50 mL	2103.1	0.15% @ 450 nm	—	121
8	DT_2TA-TAPB	H_2O and O_2	5 mg & 25 mL	8587	3.3% @ 380 nm	—	122
9	DVA-COF	H_2O : BA = 9 : 1, O_2	10 mg & 20 mL	8450[b]	2.84 @ 420 nm	0.08%	123
10	ECUT-COF-50	H_2O	5 mg & 50 mL	5382	11.2% @ 400 nm	0.68%	124
11	TT-COF-OH	H_2O	5 mg & 50 mL	3406	8.1% @ 400 nm	0.58	125
12	1H-COF	H_2O : IPA (9 : 1), O_2	30 mg & 30 mL	44.5	5.4% @ 420 nm	—	129
13	TpAQ-COF	H_2O and O_2	10 mg & 30 mL	420	7.4% @ 420 nm	—	130
14	Kf-AQ	H_2O (pH = 13), O_2	5 mg & 30 mL	4784	15.8% @ 400 nm	0.87%	131
15	POR-BQ-COF	H_2O (pH = 13), O_2	10 mg & 30 mL	1525	5.05% @ 420 nm	—	132
16	B[*f*]QCOF-1	H_2O	10 mg & 50 mL	9025	8.9% @ 450 nm	0.23%	133

[a] Light irradiation: $\lambda > 420$ nm, sunlight. [b] LED light; BA: benzyl alcohol; IPA: isopropanol.

functionalised COF photocatalyst for H_2O_2 production have been highlighted in Table 2.

Tuning of linkage in COFs for photocatalytic H_2O_2 production

Linkage engineering has emerged as a powerful strategy to enhance the photocatalytic performance of COFs for H_2O_2 production. The chemical nature of the linkages, such as imine, β-ketoenamine, hydrazone, azine, or imidazole, directly influences the COFs' electronic structure, charge separation efficiency, and interaction with oxygen molecules. By precisely tuning the linkage, researchers can modulate bandgaps, charge transfer pathways, redox potentials, and surface adsorption sites, all of which are critical for the two-electron ORR producing H_2O_2. Electron-rich linkages improve light absorption and facilitate exciton dissociation, whereas electron-deficient linkages enhance O_2 adsorption and promote selective $2e^-$ reduction over the competing $4e^-$ pathway. Additionally, robust linkages can also improve chemical stability, allowing sustained catalytic activity under aqueous and oxidative conditions. To

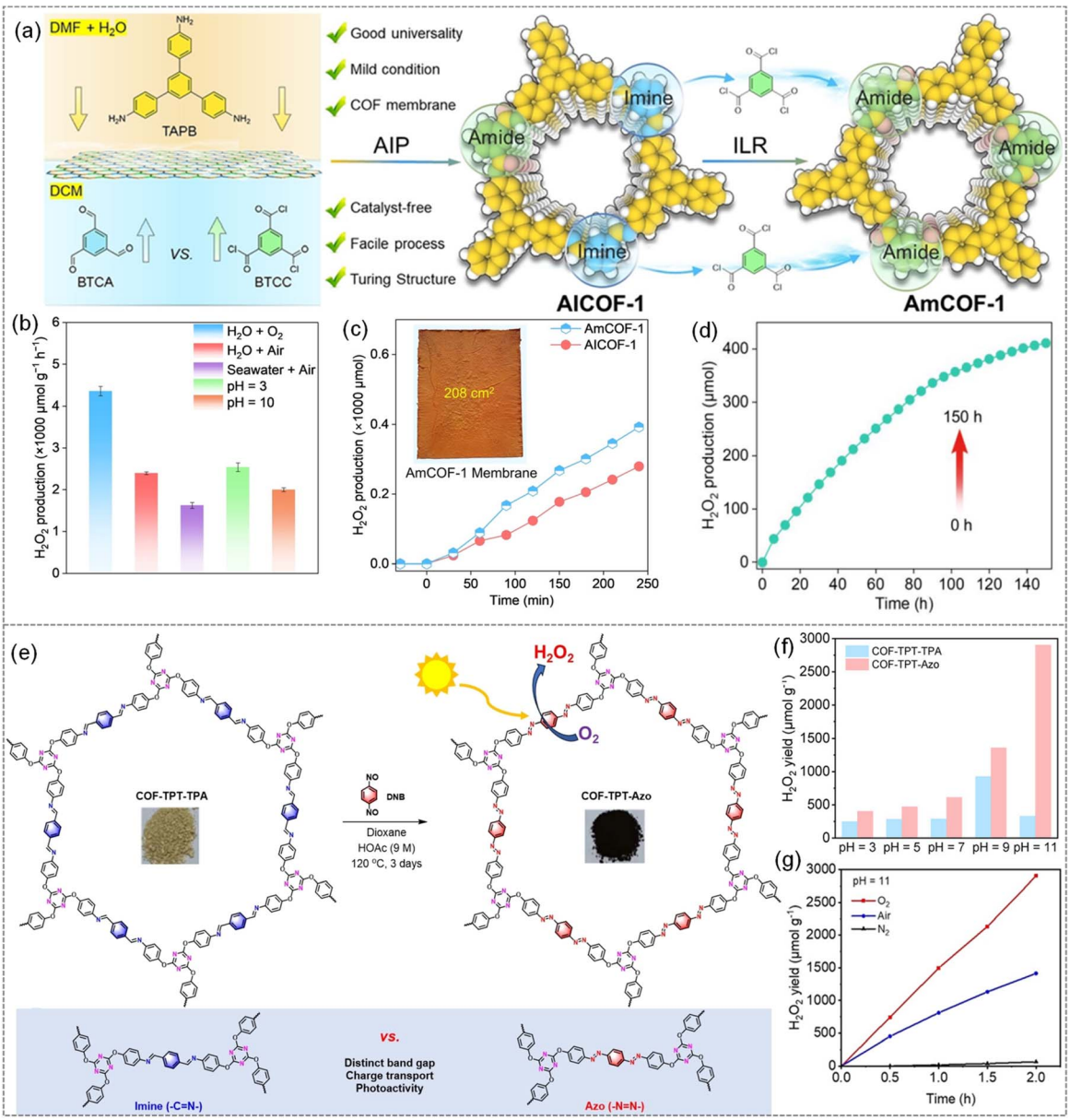

Fig. 12 (a) Illustration of synthesis of AmCOF-1 from AlCOF-1. (b) Photocatalytic H_2O_2 production of AmCOF-1 under different conditions. (c) Time course of H_2O_2 production using the membrane of AlCOF-1 and AmCOF-1 under natural light (inset: AmCOF-1 membrane). (d) Long term production H_2O_2 over 150 h with AmCOF-1. (Reproduced and reprinted with permission from ref. 136. Copyright 2025 Wiley-VCH GmbH.) (e) Synthesis scheme and structure of imine- and azo-linked COFs. (f) Photocatalytic H_2O_2 production comparison under different pH conditions. (g) Continuous H_2O_2 production with COF-TPT-Azo over 2 h under different conditions at pH 11. (Reproduced and reprinted with permission from ref. 137. Copyright 2024, Wiley-VCH GmbH.)

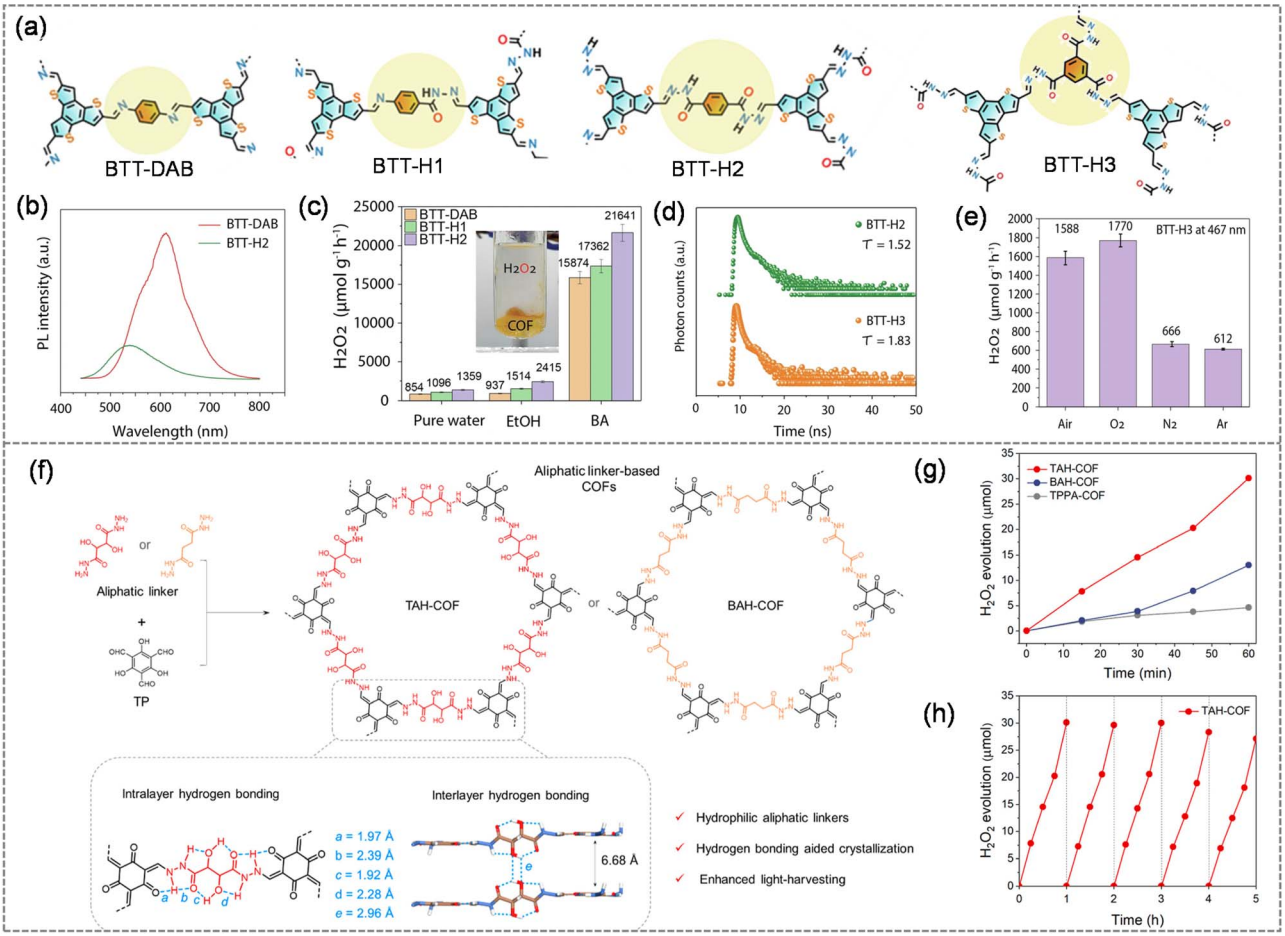

Fig. 13 (a) Structures of benzotrithiophene-based COFs with regulation of the hydrazone linkage. (b) PL spectra of benzotrithiophene-based COFs with and without hydrazone linkage. (c) Comparison of photocatalytic H_2O_2 production of benzotrithiophene-based COFs with different sacrificial electron agents. (d) TRPL data of BTT-H2 and BTT-H3 COFs. (e) Photocatalytic H_2O_2 production with BTT-H3 in different environments. (Reproduced and reprinted with permission from ref. 138. Copyright 2025, Springer Nature.) (f) Synthesis scheme and structure of COFs with an aliphatic linker. (g) Photocatalytic H_2O_2 production with aliphatic linker-based COFs. (h) Long-term photocatalytic H_2O_2 production with the TAH-COF. (Reproduced and reprinted with permission from ref. 139. Copyright 2025, American Chemical Society.)

elucidate how linkage positioning governs the photocatalytic performance and stability of COFs toward H_2O_2 production, Yang *et al.* systematically investigated the influence of *ortho* and *para* linkages in COFs. Six COFs were synthesised from *ortho*/*para*-substituted diamines (Bda, Pda, and Pzda) and Tp.[134] Pyridinic nitrogen favoured the $2e^-$ ORR, while β-ketoenamine carbons acted as $4e^-$ WOR active sites, making Pzda-based COFs the most efficient. Although *p*-COF-TpBda showed a high initial H_2O_2 rate (6434 μmol g^{-1} h^{-1}), it rapidly degraded, whereas *o*-COF-TpPzda maintained stable H_2O_2 production (4396 μmol g^{-1} h^{-1}) for 48 h. DFT revealed a lower ΔG for the rate-determining WOR step in *o*-COF-TpPzda, enabling faster hole consumption and enhanced stability, while largely preserving $2e^-$ ORR activity. Linkage chemistry also plays a key role in achieving crystalline, robust COFs while enabling functionalities such as band-gap modulation and redox activity. Mou *et al.* reported azole-linked COFs synthesised from pyrene aldehyde and heteroatom-substituted phenylenediamines, yielding thiazole (TZ-COF), oxazole (OZ-COF), and imidazole (IZ-COF) frameworks.[135] These azole linkages introduce electron-donating conjugation within a D–π–A architecture, enhancing visible-light absorption and charge transport. Femtosecond transient absorption revealed the longest excited-state lifetime for the TZ-COF (5.94 ps), followed by the OZ-COF (3.74 ps) and IZ-COF (1.86 ps), indicating more efficient charge separation with thiazole linkages. Accordingly, the O_2 production activity follows the order: TZ-COF > OZ-COF > IZ-COF. A distinct difference in efficiency and stability between reversible imine-linked COFs (AICOF-1) and irreversible amide-linked COFs (AmCOF-1) has been demonstrated by Li *et al.* for photocatalytic H_2O_2 production.[136] They have synthesised the self-standing membrane of crystalline COFs for photocatalytic H_2O_2 production. In brief, AICOF-1 was synthesised using an ingenious autocatalytic interfacial polymerisation (AIP) strategy. Subsequently, AICOF-1 was converted into a fully amide-linked crystalline membrane (AmCOF-1) *via* a traditional irreversible linker renovation (ILR) reaction with acyl chlorides, yielding COFs with well-defined Turing structures (Fig. 12a). This

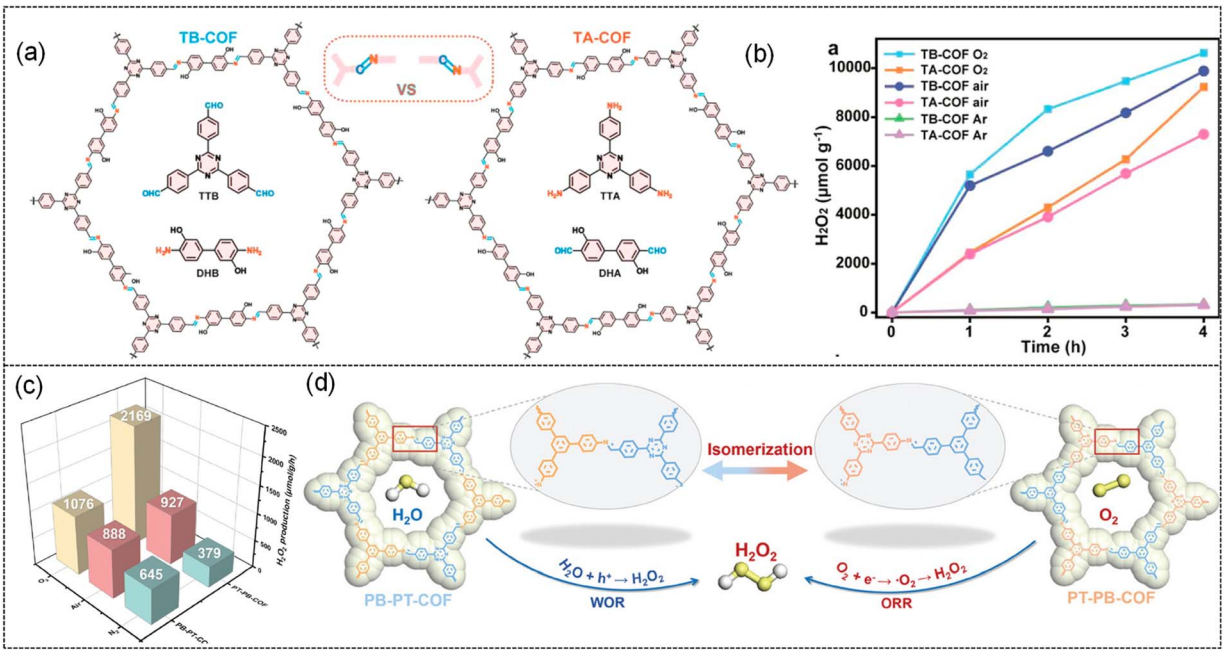

Fig. 14 (a) Illustration of synthesis of isomeric TA-COF and TB-COF. (b) Time-dependent H_2O_2 synthesis with isomeric COFs in different atmospheres. (Reproduced and reprinted with permission from ref. 140. Copyright 2025, American Chemical Society.) (c) Comparison of photocatalytic H_2O_2 production with PB-PT-COF and PT-PB COF. (d) Structures of isomeric PB-PT-COF and PT-PB COF, highlighting their pathways for the production of H_2O_2. (Reproduced and reprinted with permission from ref. 141. Copyright 2024, Wiley-VCH GmbH.)

approach offers several advantages, including broad applicability, a simple and catalyst-free synthesis at ambient temperature, and the ability to produce large, free-standing membranes with diverse Turing patterns. Given the robust nature, efficient electron-withdrawing ability, and potential π-electron segregation effect of the amide units, the authors have demonstrated the photocatalytic efficiency of AmCOF-1 membrane towards H_2O_2 production in various media, including pure water, seawater, and solutions with high pH and low pH (Fig. 12b). The photocatalytic H_2O_2 production reached up to 4353 μmol g^{-1} h^{-1} in O_2-saturated H_2O. Furthermore, a large-area (16 cm × 13 cm) self-standing AmCOF-1 membrane showed stable H_2O_2 production for 4 h under natural sunlight (Fig. 12c). The AmCOF-1 membrane also shows remarkable stability over 150 h under sunlight without sacrificial agents (Fig. 12d), which was further verified by PXRD of recovered samples. In a similar direction, Zhao and co-workers compared the photocatalytic performance of azo-linked and imine-linked COFs for H_2O_2 production.[137] They rationally synthesised two COFs, an imine-linked COF (COF-TPT-TPA) and an azo-linked COF (COF-TPT-Azo) *via* Schiff-base polycondensation (Fig. 12e). Remarkably, despite differing by only a single atom (–N=N–*vs.*–C=N–) COF-TPT-Azo shows a much narrower band gap, improved charge transport, and enhanced photoactivity compared to its imine counterpart. Consequently, COF-TPT-Azo was found to produce H_2O_2 at a rate of 1498 μmol g^{-1} h^{-1} in O_2-saturated alkaline solution of pH = 11 under visible light irradiation (λ > 420 nm), which is 7.9 times higher than that of imine-based COF-TPT-TPA (Fig. 12f). COF-TPTAzo showed remarkable H_2O_2 production in alkaline solution both under O_2 and air (Fig. 12g). DFT studies show that the HOMO is distributed in the N=N group, while the LUMO is on the same azobenzene units. Therefore, the N=N groups in COF-TPT-Azo and C=N groups in COF-TPT-TPA play an important role in light absorption and promote the photocatalytic oxidation.

The effect of hydrazone linkages and their density has recently been studied by Pachfule *et al.*[138] They synthesised a series of D–A thiophene-based COFs (BTT DAB, BTT-H1 and BTT-H2) and regulated the hydrazone density (0–2) (Fig. 13a). This gradual variation enabled a direct comparison of how hydrazone density affects photocatalytic behaviour. The introduction of hydrazone linkages decreased e–h recombination, as indicated by the decreased PL (Fig. 13b). The production of H_2O_2 was observed to vary directly in proportion to the number of hydrazone linkages. As a result, BTT-DAB, BTT-H1, and BTT-H2 produced H_2O_2 at a rate of 854, 1096, and 1359 μmol g^{-1} h^{-1} from water and air under irradiation of 467 nm light, respectively. BTT-H2 also delivered a dramatically higher output of 21 641 μmol g^{-1} h^{-1} in the presence of benzyl alcohol as a sacrificial agent (Fig. 13c). Motivated by the results, the authors also synthesised the BTT-H3 COF with three hydrazone linkages (Fig. 13a). An increase in hydrazone density increased the lifetime of the photogenerated electron, as indicated by the TRPL plot (Fig. 13d). BTT-H3 delivered H_2O_2 production of 1588 μmol g^{-1} h^{-1} from water and air (Fig. 13e), higher than that of BTT-H2. COF BTT-H3 also produced up to 550 μmol g^{-1} h^{-1} H_2O_2 under natural sunlight, highlighting its potential for practical solar-driven applications. It is well known that COFs have traditionally been built from aromatic linkers because their π–π

Table 3 Summary of the representative linkage modification on COF photocatalysts for H_2O_2 photosynthesis

Sl. no.	Catalyst	Reaction conditions	Dosage (mg) & volume (mL)	H_2O_2 yield (μmol g^{-1} h^{-1})	AQY	SCC	Ref.
1	*o*-COFTpPzda	H_2O and O_2	5 mg & 40 mL	4396	—	0.46%	134
2	TZ-COF	H_2O : BA (1 : 1) and O_2	15 mg & 30 mL	4951	0.6% @ 475 nm	0.036%	135
3	AmCOF-1	H_2O and O_2	Membrane based	4353	8.72% @ 420 nm	—	136
4	COF-TPT-Azo	H_2O (pH 11) and O_2	10 mg & 40 mL	1498	—	—	137
5	BTT-H3	H_2O and O_2	5 mg & 10 mL	1770	17.7% @ 467 nm	2.02%	138
6	TAH-COF	H_2O	5 mg & 50 mL	6003	7.72% @ 500 nm	0.66%	139
7	TB-COF	H_2O	1 mg & 8 mL	5186 4111[a]	3.45% @ 420 nm	1.08%	140
8	PT-PB-COF	H_2O and O_2	5 mg & 20 mL	2169	0.74%	0.055%	141
9	COF-Tfp-BDDA	H_2O and O_2	10 mg & 20 mL	880	—	—	142

[a] Light irradiation: $\lambda > 420$ nm, sunlight; BA: benzyl alcohol.

stacking promotes high crystallinity and provides continuous π-channels for efficient exciton and charge transport.

Despite these advantages, aromatic linkers are often hydrophobic, which reduces water affinity and limits the efficiency of COFs in aqueous photocatalytic systems. To overcome this challenge, Zhu and co-workers demonstrated that aliphatic linkers can also form crystalline COFs and show subsequent enhancement in their hydrophilicity by reacting with aliphatic linkers such as tartronic acid dihydrazide (TAH) or butanedioic acid dihydrazide (BAH) with 1,3,5-triformylphloroglucinol (TP) that resulted in two hydrazone-linked COFs, termed TAH-COF and BAH-COF (Fig. 13e).[139] These two COFs are crystalline and have a BET surface area of 703 m^2 g^{-1} and 530 m^2 g^{-1} for the TAH-COF and BAH-COF, respectively. These aliphatic linkers create dense hydrogen-bonding networks that stabilise the framework, enhance crystallinity, and ensure good compatibility with water while maintaining strong visible-light absorption. As a result, the COFs display narrow optical band gaps (~1.9 eV) and high photocatalytic activity, with the TAH-COF delivering an impressive H_2O_2 production rate of 6003 μmol g^{-1} h^{-1} without sacrificial agents (Fig. 13f). The aliphatic TAH-COF also showed notable structural integrity following photocatalysis, as highlighted by the nominal difference in PXRD before and after photocatalysis (Fig. 13g). The influence of linkage orientation on photocatalytic H_2O_2 production has also been clearly illustrated through the work of Yue *et al.*[140] Two isomeric COFs: TB-COF and TA-COF, were constructed with identical building blocks but opposite imine-bond orientations (Fig. 14a). Although the structural difference between the two frameworks is subtle, their photocatalytic behaviours diverge sharply. The orientation present in the TB-COF generates a larger dipole moment and promotes more efficient charge separation, which together account for its markedly higher H_2O_2 production compared to the TA-COF. Both COFs show notable H_2O_2 production both in O_2 and air-saturated water (Fig. 14b). The H_2O_2 production of TB-COF was measured to be 5186 and 4111 μmol g^{-1} h^{-1} in air-saturated water and natural seawater, respectively, which are higher than the values of TA-COF (2387 and 1640 μmol g^{-1} h^{-1}). A similar study was also reported by Zhou *et al.*, wherein they synthesised constitutional-isomerised COFs (PB-PT-COF and PT-PB-COF) by swapping monomers around imine bonds.[141] The two isomeric COFs have similar composition and pore sizes but different optoelectronic properties, leading to distinct photocatalytic efficiency. Consequently, under O_2-saturated conditions, the PB-PT-COF and PT-PB-COF generated 1076 and 2169 μmol g^{-1} h^{-1} H_2O_2, respectively. In contrast, when the reaction was carried out in N_2-saturated water, the PB-PT-COF delivered a higher activity (645 μmol g^{-1} h^{-1}) than the PT-PB-COF (349 μmol g^{-1} h^{-1}) (Fig. 14c). DFT calculations revealed that the PT-PB-COF has a stronger affinity for O_2 and activates it more effectively, thereby favouring H_2O_2 formation through the ORR pathway. The PB-PT-COF, on the other hand, interacts more strongly with H_2O, leading to H_2O_2 production primarily *via* the WOR pathway (Fig. 14d). The major achievements of the linkage modified COF photocatalyst for H_2O_2 production have been highlighted in Table 3.

Tuning the structural topology of COFs for photocatalytic H_2O_2 production

Topological structures, such as lattices, aggregations, and textural configurations, are fundamental in natural and synthetic systems.[143] In nature, these structures can be found in various biological, geological, and chemical systems.[144] The pursuit of designing and engineering topological structures at the molecular and atomic scales is driven by the potential to create materials with unprecedented precision and performance. At these small scales, the properties of materials can be radically different from those at the macro scale, often exhibiting enhanced or entirely new functionalities, such as improved strength, electrical conductivity, or catalytic activity. In reticular chemistry,[145] COFs with various topologies can be designed by manipulating the arrangement of building blocks through geometric control. This method enables the creation of highly ordered structures by linking organic molecules with covalent bonds, offering precise tuning of properties such as surface area, stability, and functionality. The impact of various factors, such as changes in linkage, functional groups, and D–A incorporation, on the optical and electronic properties of COFs for H_2O_2 production has been extensively studied. Recently, there has been growing interest in exploring how topological changes in COFs influence their performance in H_2O_2

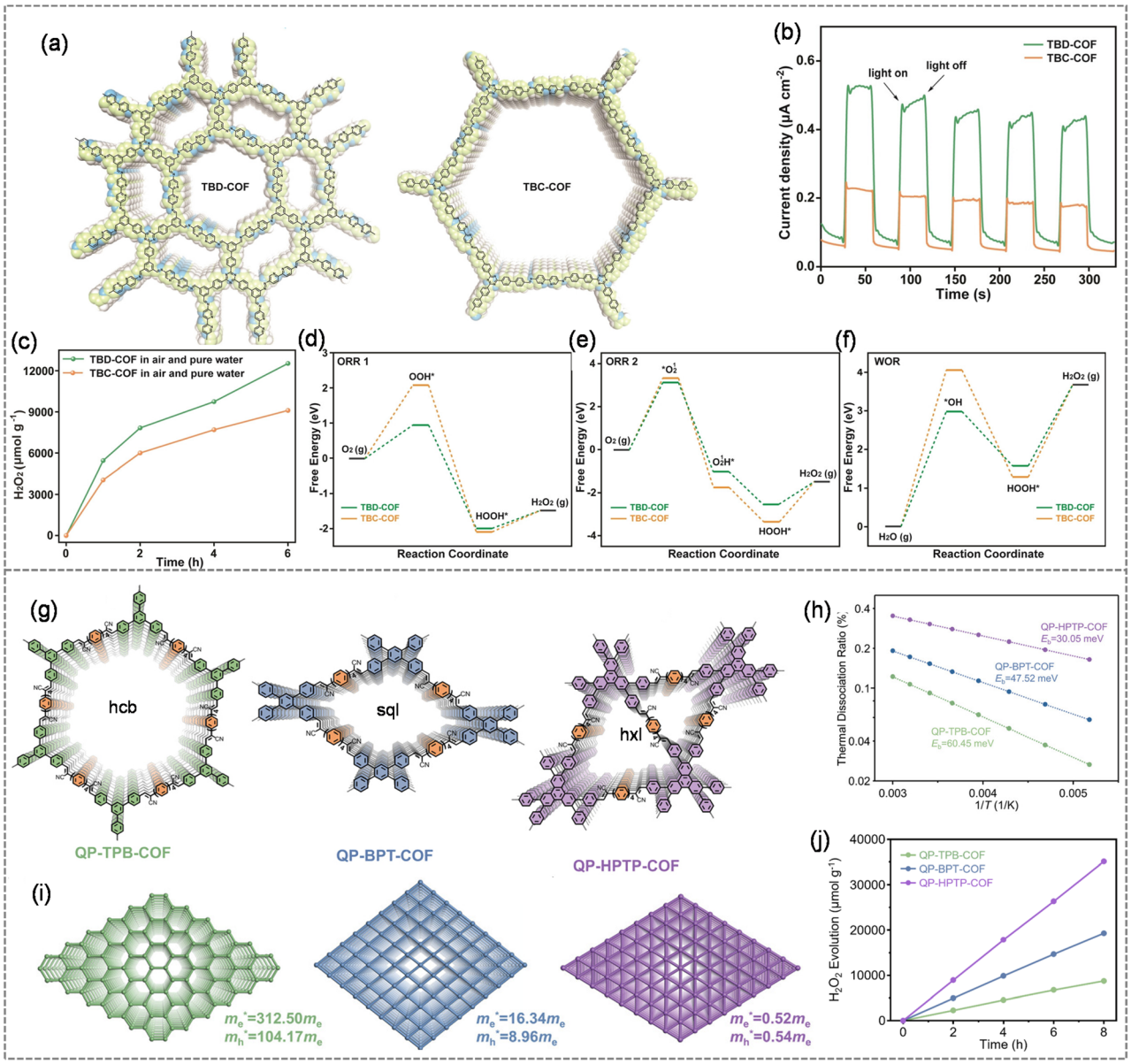

Fig. 15 (a) Structures of TBD-COF and TBC-COF. (b) Photocurrent plot of the TBD-COF and TBC-COF. (c) Photocatalytic H_2O_2 production comparison between the TBD-COF and TBC-COF. (d–f) Gibbs free energy diagrams of TBD-COF and TBC-COF for H_2O_2 photoproduction *via* the (d) O_2–$^{\bullet}O_2$···H_2O_2 pathway, (e) O_2–$^{\bullet}O_2^-$–$^1O_2$–H_2O_2 pathway, and (f) $2e^-$ WOR pathway. (Reproduced and reprinted with permission from ref. 146. Copyright 2024, Wiley-VCH GmbH.) (g) Structures of COFs with different topologies. (h) Exciton dissociation rates in COFs. (i) Schematic illustration of the correlation between the topology and effective mass (m_e^* and m_h^*) in different COFs. (j) Long-term H_2O_2 photoproduction over 8 h using the P-TPB-COF, QP-BPT-COF, and QP-HPTP-COF. (Reproduced and reprinted with permission from ref. 147. Copyright 2024, Wiley-VCH GmbH.)

production. For instance, Yue *et al.* investigated the impact of topology on the photocatalytic production of H_2O_2 in 2D COFs.[146] They synthesised two 2D COFs, TBD-COF and TBC-COF, which exhibit similar chemical components but different topologies (Fig. 15a). The TBD-COF exhibited a cpt topology with six-arm cores, while the TBC-COF displayed an hcb topology with three-arm cores. The topological differences have brought distinct variations in the photophysical properties of these two COFs. In addition, it has also influenced mass transport and charge transfer modulation, enhancing their photocatalytic performance for H_2O_2 production (Fig. 15b). On evaluating the catalytic activity towards light-driven H_2O_2 production, the TBD-COF outperforms the TBC-COF, producing H_2O_2 at a rate of 5448 and 4049 μmol g^{-1} h^{-1}, respectively, from air and pure water. When evaluated for photocatalytic H_2O_2 production, the TBD-COF exhibited superior performance to the TBC-COF, showing a steady increase in the H_2O_2 yield with prolonged irradiation, particularly beyond 6 h (Fig. 15c). The TBD-COF achieved a production rate of 5448 μmol g^{-1} h^{-1}, higher than that of TBC-COF (4049 μmol g^{-1} h^{-1}) using air and

pure water. The mechanistic investigation revealed the formation of H_2O_2 through three channels: two distinct $2e^-$ ORR routes involving superoxide (O_2–$O_2^{\bullet-}$·H_2O_2) and singlet oxygen species (O_2–$O_2^{\bullet-}$–$O_2{}^1$–H_2O_2), along with one $2e^-$ WOR pathway (H_2O–H_2O_2) (Fig. 15d–f). The photocatalytic generation of H_2O_2 is generally accompanied by its decomposition, typically following zero-order and first-order kinetics, respectively. For example, the TBD-COF and TBC-COF exhibited H_2O_2 formation rate constants (k_f) of 0.84 and 0.64 mM h^{-1}, respectively, while the corresponding decomposition rate constants (k_d) were 0.49 and 0.54 h^{-1}, respectively. Long-term irradiation studies further illustrate a characteristic production-decomposition interplay. The concentration of H_2O_2 increases steadily during the initial reaction period (up to 10 h), followed by a gradual decline as decomposition becomes dominant. This behaviour is often associated with photocatalyst fatigue or partial structural degradation under extended light exposure, induced by reactive oxygen species and accumulated charge carriers, which leads to reduced crystallinity and consequently shifts the balance toward faster H_2O_2 breakdown. The effect of topology on H_2O_2 production has also been meticulously studied by Xu *et al.*, where they have synthesised three 2D sp^2 carbon-linked π-conjugated COFs, such as QP-TPB-COF, QP-BPT-COF, and QP-HPTP-COF, having hcb, sql, and hxl topologies, respectively (Fig. 15g).[147] Compared to COFs adopting hcb or sql lattices, the hxl-topology QP-HPTP-COF stands out by exhibiting the lowest exciton binding energy (E_b), markedly reduced carrier effective masses, and the highest charge-transfer efficiency (Fig. 15h). To probe the topology-dependent electronic characteristics of COFs, the effective carrier masses (m^*) were evaluated through DFT calculations. Notably, the QP-HPTP-COF displayed remarkably lower electron and hole effective masses ($m_e = 0.52m_e$; $m_h = 0.54m_e$) relative to the QP-TPB-COF ($m_e = 312.5m_e$; $m_h = 104.17m_e$) and QP-BPT-COF ($m_e = 16.34m_e$; $m_h = 8.96m_e$) (Fig. 15i), suggesting a substantially higher intrinsic carrier mobility and, consequently, enhanced photocatalytic potential for the QP-HPTP-COF. Consequently, the photocatalytic tests conducted in O_2-saturated pure water under visible light irradiation revealed the highest efficiency for the QP-HPTP-COF with the hxl topology, followed by the QP-BPT-COF with the sql topology, and finally the QP-TPB-COF with the hcb topology. The respective H_2O_2 production rates for these materials were 4388, 1902, and 921 μmol g^{-1} h^{-1} (Fig. 15j). The QP-HPTP-COF also exhibited an AQE of 22.78% and an SCC of 1.41%, the highest reported SCC value among other COFs. The synthesis of 3D COFs with high surface areas, exposed active sites, and tunable frameworks has gained interest among researchers. However, synthesising 3D COFs overcomes various challenges, such as low-connectivity building units, low crystallinity, low yield, *etc.* With the use of a tetrahedral linkage, Omar M. Yaghi reported the first 3D COF in 2007.[148] Since then, various 3D COFs have been synthesised, and different types of topologies have been reported for 3D COFs.[149] The construction of 3D COFs generally demands linkers with predefined spatial orientation

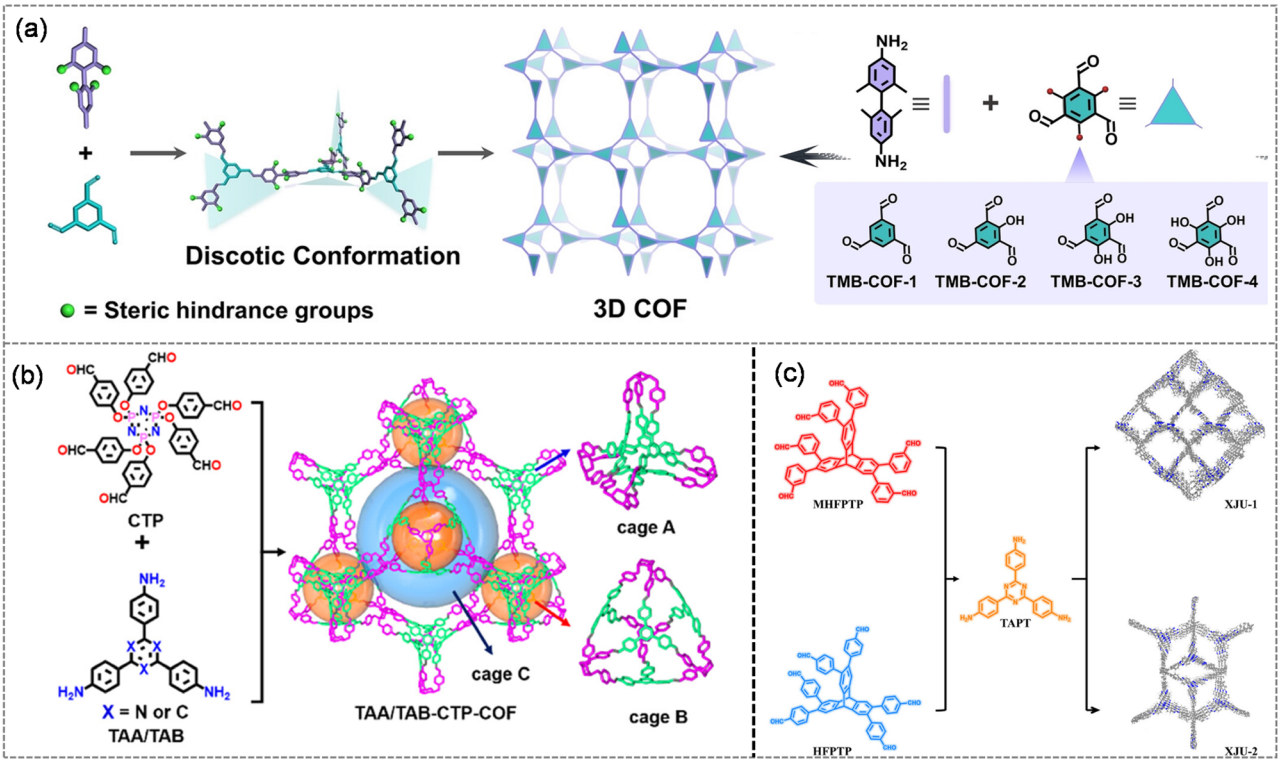

Fig. 16 (a) Schematic route to formation of 2D COFs using planar and linear monomers. (Reprinted with permission from ref. 151. Copyright 2024, Wiley-VCH GmbH.) (b) Schematic route to synthesis of 3D COFs. (Reprinted with permission from ref. 152. Copyright 2024, American Chemical Society.) (c) Synthetic scheme of 3D COFs XJU-1 and XJU-2. (Reprinted with permission from ref .153. Copyright 2025, Wiley-VCH GmbH.)

and high-connectivity nodes. In contrast to 2D COFs, only a limited number of frameworks have been realised, primarily due to the synthetic complexity, harsh reaction conditions, scarcity of suitable 3D linkers, such as tetrahedral, hexavalent triangular prisms, anti-triangular prisms, and octavalent cubic units, and the inherent crystallisation difficulty arising from multiple degrees of rotational freedom. Recently, progress has been made through strategies that exploit the torsional characteristics of linkers, where modulation of the torsion angle enables the formation of stable 3D COF networks.[150] In line with this approach, Zhu *et al.* demonstrated a successful synthesis of a 3D COF by utilising controlled molecular torsion to drive the 3D framework.[151] They deliberately chose 2,2′,6,6′-tetramethylbenzidine (TMB) as a linker where the four methyl groups introduce steric hindrance between the two phenyl rings, generating a stereoscopic disc-like conformation that preserves local planarity while promoting antiparallel stacking (Fig. 16a). Four COFs were subsequently synthesised by coupling TMB with a series of trialdehydes containing varying numbers of hydroxyl groups (ranging from 0 to 3) (Fig. 16a). The steric hindrance in TMB introduces an additional force that alters the torsion angles of the peripheral triangular units, directing the linear unit to connect with the trigonal unit and adapted 3D srs topology. By exploiting steric hindrance effects, these 3D COFs exhibit exceptionally high surface areas and well-defined pore architectures, which collectively promote greater exposure of catalytic sites and facilitate efficient mass transport. A clear structure–activity trend is observed: as the number of ketone-based active sites increases, the photocatalytic H_2O_2 production performance improves accordingly. Under pure water and O_2-saturated conditions, TMB-COF-1, TMB-COF-2, and TMB-COF-3 deliver H_2O_2 formation rates of 218, 1293, and 2621 μmol g^{-1} h^{-1}, respectively, while TMB-COF-4 achieves an impressive 5106 μmol g^{-1} h^{-1}. TMB-COF-4 also exhibited H_2O_2 photocatalytic production rate of 1396 μmol g^{-1} h^{-1} under pure water and air conditions. In comparison, the analogous 2D BZD-COFs demonstrate considerably lower activity under identical conditions. Collectively, these findings highlight the strong correlation between 3D framework design, active-site incorporation, and photocatalytic efficiency, emphasising that deliberate structural optimisation is a powerful strategy for advancing COF-mediated H_2O_2 production. Since topology strongly influences parameters such as pore arrangement, charge-transfer pathways, and crystallinity, different 3D COFs inherently exhibit diverse property profiles and performance behaviours. The photocatalytic performance of two topologically distinct 3D COFs for H_2O_2 production was recently reported by Liao *et al.* Two 3D COFs (TAA/TABCTP-COF) were obtained by reacting a trigonal antiprism (C3) monomer, denoted as CTP, with a planar amine linker monomer, denoted as TAA or TAB (Fig. 16b).[152] CTP has N, O, and P that can act as active sites for the WOR, whereas the amine linker has triazine (TAA) or benzene (TAB) in its core that acts as an acceptor to photogenerated electrons during the ORR. The triazine-containing COF, denoted as TAACTP-COF, produced H_2O_2 at a rate of 1041 μM h^{-1} from H_2O and O_2. In the presence of isopropanol as a sacrificial agent, the production rate increased to 2221 μM h^{-1}. The theoretical calculation showed that the distribution of the HOMO, mostly on the CTP ring, and the LUMO on TAA or TAB indicates CTP as an oxidising site for the WOR and TAA/TAB as a reducing site for the ORR. The unprecedented efficiency of 3D COFs over 2D COFs has also been recently reported by Lan *et al.* Two 3D COFs (XJU-1 and XJU-2) using a hexadentate triptycene-based monomer and a tridentate triazine amine linker were synthesised (Fig. 16c).[153] The two COFs are isomeric, having a difference in the linkage position. The 3D COFs exhibit high crystallinity with a ceq topology. The two COFs have distinct photochemical properties, and in the presence of benzyl alcohol, XJU-1 and XJU-2 demonstrated impressive photocatalytic activity for H_2O_2 production, achieving rates of 34 777 μmol g^{-1} h^{-1} and 11 922 μmol g^{-1} h^{-1}, respectively. In the absence of a sacrificial agent, the production reached up to 7453 and 8124 μmol g^{-1} h^{-1} for XJU-1 and XJU-2, respectively. The larger pore aperture of XJU-1 relative to XJU2 promotes faster mass diffusion and more efficient O_2 activation, resulting in enhanced H_2O_2 output. Mechanistic studies (radical quenching, EPR, and RDE) confirmed ORR-dominated H_2O_2 formation in both COFs, where XJU-1 follows a mixed $1e^-/2e^-$ ORR process, while XJU-2 mainly adopts a direct $2e^-$ pathway. DFT results further attributed the performance differences to topology-dependent charge separation and strong O_2 binding at multiple active sites. The reduced singlet–triplet energy gap (ΔE_{S-T}) and orthogonal triptycene structure additionally favour $^1O_2$ formation, collectively accelerating H_2O_2 evolution. The study underscores how the 3D COF topology governs ORR selectivity and boosts the photocatalytic H_2O_2 production efficiency. The synthesis of COFs with connectivity up to four is well known, and its synthesis procedure has been generalised. However, designing 3D COFs with high connectivity (≥8) is challenging and scarce. The higher number of connectivity often correlates with high stability of the framework; therefore, it is desirable to synthesise highly connected 3D COFs. Porphyrin units, known for their excellent light-harvesting capability, have been strategically employed as linkers in COF design for photocatalytic H_2O_2 generation. Upon protonation of the pyrrole nitrogen, the porphyrin macrocycle undergoes pronounced geometric distortion both within and out of the molecular plane, which can significantly influence charge separation and exciton dynamics. Leveraging this structural tunability, Jiang *et al.* synthesised two three-dimensional porphyrin-based COFs (Por-COF-cya) featuring vinyl linkages through an aldol condensation reaction.[154] Por-COF-cya adopts a first-ever-reported cya topology that has the interconnectedness of 8-connected and 3-connected nodes (Fig. 17a). The incorporation of porphyrin units into the Por-COF-cya framework imparts favourable photophysical and chemical stability. Moreover, the electron-deficient triazine moieties enable efficient encapsulation of the electron-donating tetrathiafulvalene (TTF) species within the hierarchical pores *via* electrostatic attraction and host–guest interactions. This results in the formation of a donor–acceptor architecture (TTF@Por-COF-cya) that promotes rapid charge transfer and ultimately enhances photocatalytic H_2O_2 production. Consequently, the H_2O_2 yield in pure aqueous solution reached 2209

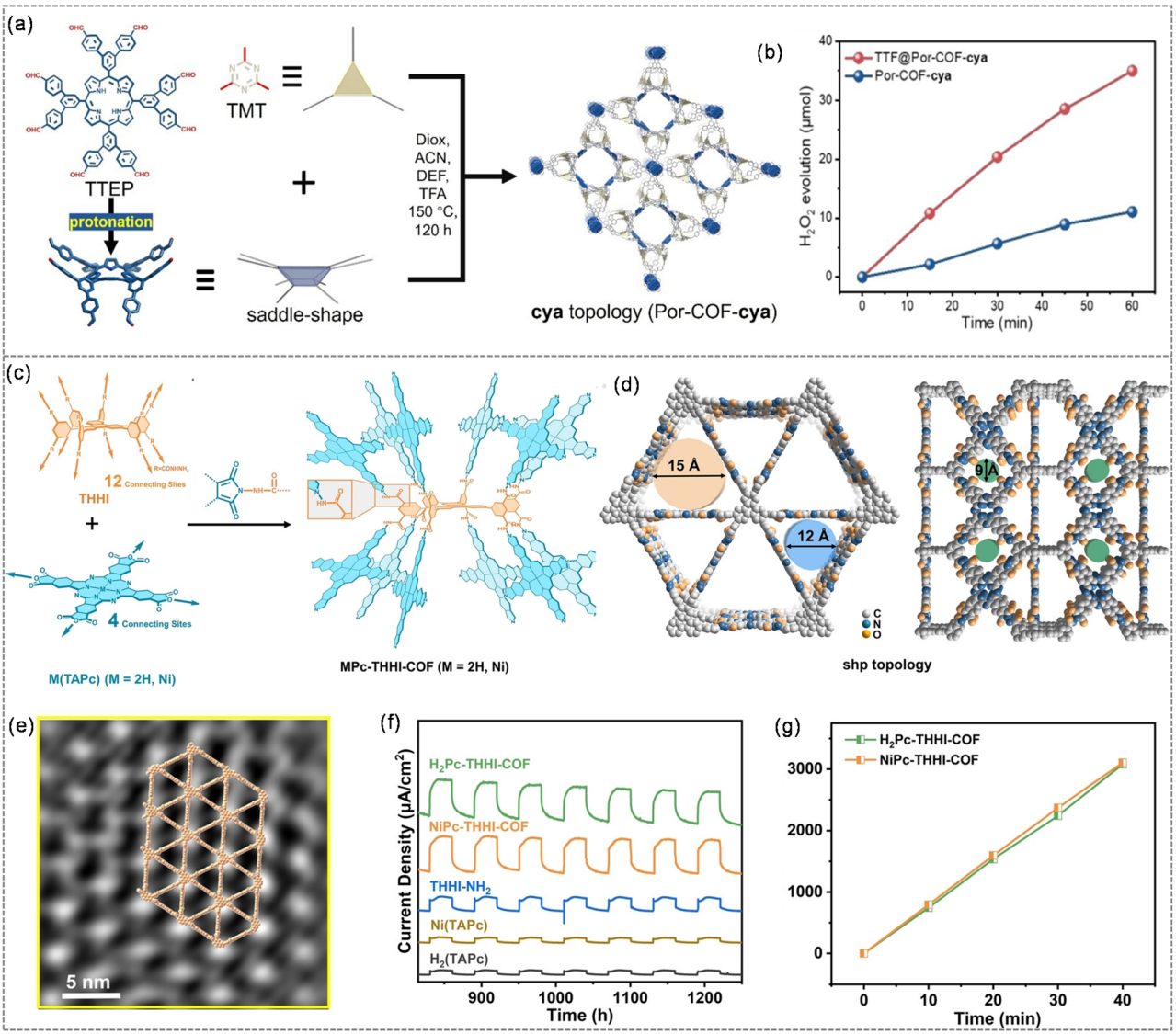

Fig. 17 (a) Synthetic scheme for cya topology-based Por-COF-cya. (b) Reaction kinetics for H_2O_2 production. (Reprinted with permission from ref. 154 Copyright 2024 Wiley-VCH GmbH). (c) Synthetic scheme of MPc-THHI-COF (M = 2H, Ni) with 12 connecting sites. (d) Simulated packing structures in MPc THHI-COF (M = 2H, Ni) along the *c* axis (left) and *a* or *b* axis (right). (e) HRTEM image of the H_2Pc-THHI-COF. (f) Comparison of photocurrent of different 3D THHI-COFs. (g) Kinetics for H_2O_2 production with the H_2Pc-THHI-COF and NiPc-THHI-COF. (Reprinted with permission from ref. 155. Copyright 2024, Wiley-VCH GmbH.)

and 6994 μmol g^{-1} h^{-1} with Por-COF-cya and TTF@Por-COF-cya, respectively (Fig. 17b). Analysis of H_2O_2 yields under different atmospheres, supported by isotope-labelling experiments, confirmed that 84% of the oxygen atoms in the generated H_2O_2 originated from the ORR pathway, while the remaining 16% were derived from the WOR route. DFT calculations identified two potential electrophilic sites in Por-COF-cya: the non-protonated porphyrin nitrogen and the triazine ring, where O_2 showed preferential adsorption at the triazine site, consistent with *in situ* DRIFTS results and confirming it as the primary ORR-active centre. Moreover, TTF@Por-COF-cya displayed lower O_2 adsorption free energy and reduced intermediate-conversion barriers compared to Por-COF-cya, facilitating $^*OOH$ formation and thereby enhancing the H_2O_2 production efficiency. A highly connected 3D COF for photocatalytic H_2O_2 production has also been reported by Wang *et al.*[155] They synthesised highly connected phthalocyanine-based (Pc-based) two 3D COFs MPc-THHI-COFs (M = H_2, Ni) with 12 connecting sites (Fig. 17c). These COFs were found to adopt a shp topology, featuring 1D triangular channels with diameters of 12 Å and 15 Å along the *c* axis, which are further interconnected by rhombohedral windows, each with a size of 9 Å along the *a* and *b* axes (Fig. 17d). The triangular channels similar to the open channel of the SHP networks of the COF can be visualised through HRTEM images, indicating the high crystallinity of the synthesised 3D COF (Fig. 17e). The synthesised 3D COFs exhibit a broadened visible light absorption range, a narrow optical band gap, and 3D interconnected

Table 4 Summary of representative topological and structural modifications on COF photocatalysts for H_2O_2 photosynthesis[a]

Sl. no.	Catalyst	Reaction conditions	Dosage (mg) & volume (mL)	H_2O_2 yield (mmol g^{-1} h^{-1})	AQY	SCC	Ref.
1	TBD-COF	H_2O	1 mg & 8 mL	5448	5.95% @ 420 nm	0.90%	146
2	QP-HPTP-COF	H_2O and O_2	30 mg & 10 mL	4388	22.78% @ 420 nm	1.41%	147
3	TMB-COF-4	H_2O and O_2	—	5106	—	—	151
4	TAA-CTP COF	H_2O and O_2	10 mg & 5 mL	1041 mM h^{-1}	—	—	152
5	XJU-1	H_2O : BA EtOH (9 : 1) and O_2	5 mg & 20 mL	34 777	9.7% @ 380 nm	—	153
6	TTF@Por-COF-cya	H_2O	5 mg & 50 mL	6994	14.98% @ 420 nm	—	154
7	H_2Pc-THHI-COF	H_2O and O_2	5 mg & 50 mL	4511	—	—	155

[a] Light irradiation: Xe lamp (λ > 420 nm); BA: benzyl alcohol.

nanochannels, which collectively enhance their photocatalytic performance. These features enable efficient H_2O_2 generation at a rate of 4511 and 4589 μmol g^{-1} h^{-1} from O_2-saturated H_2O *via* $2e^-$ ORR and WOR pathways, respectively, under visible-light irradiation (Fig. 17f). The major achievements of the topology and structural modified COF photocatalyst for H_2O_2 production have been highlighted in Table 4.

Microenvironment tuning in COFs for efficient H_2O_2 production

The term microenvironment usually refers to the local chemical and structural surroundings within and around the framework where catalytic reactions occur. The concept of microenvironment in COFs has emerged as a critical determinant of their functional behaviour, particularly in catalysis. Beyond framework composition, the confined pore space, including its topology, chemical polarity, electronic distribution, and host–guest interactions, collectively shapes how reactants diffuse, adsorb, and activate within the lattice. Despite being a well-defined and widely applied strategy in zeolite catalysis, microenvironment control in COF-based catalysts is only beginning to emerge, offering substantial room for advancement.[156] The modulation in the microenvironment dictates molecular diffusion, O_2 adsorption, charge separation, and intermediate stabilisation. By tailoring these confined reaction spaces, COFs can selectively promote the $2e^-$ ORR/WOR pathway while suppressing side reactions, enabling efficient H_2O_2 generation under mild conditions. In a recent report, Guo and co-workers revealed that Pauli repulsion combined with electron interactions leads to uneven electron distribution in COFs, creating selective O_2 binding sites that promote efficient photocatalytic H_2O_2 generation.[157] Two COFs were synthesised for further study, namely, TAPT-FTPB and TAPT-BPDB, with asymmetric and symmetric local electron distributions (Fig. 18a). Their findings indicate that TAPT-FTPB COFs, featuring a locally asymmetric electron distribution, exhibit enhanced oxygen adsorption capacity and stronger adsorption interactions, contributing to improved photocatalytic performance. Consequently, a H_2O_2 production of 3780 μmol g^{-1} h^{-1} was achieved (Fig. 18b) with an SCC of 1.22%. The TAPT-FTPB also shows long-term H_2O_2 production over 30 h and exhibits no degradation after ten continuous cycles (Fig. 18c). Similarly, Ding *et al.* reported a one-pot "grafting-to" approach to modulate the local electronic environment within a series of isoreticular multicomponent COFs (Fig. 18d).[158] By incorporating electron-donating or electron-withdrawing groups into the pore channels, they successfully converted photo-inert COFs into photoactive ones through the formation of intramolecular D–A architectures. Remarkably, the COF functionalized with electrophilic 2-aminothiazole delivered an impressive H_2O_2 production rate of 3701 μmol g^{-1} h^{-1} and attained an SCC efficiency of 0.13%. Recently, Zhang *et al.* reported the impact of microenvironment regulation in COFs on the overall photocatalytic activity by varying the number of nitrogen atoms within the framework.[159] An increased number of nitrogen atoms effectively modulated the local microenvironment and enhanced the electrophilicity of the COF. Among the series, the COF with the highest nitrogen content demonstrated superior performance, achieving efficient photogenerated charge separation and maximising H_2O_2 production from natural resources like sunlight and seawater. A remarkable H_2O_2 generation rate of 4881 μmol g^{-1} h^{-1} was attained. Typically, organic polymeric materials, including COFs, exhibit an exciton diffusion distance of only 5–10 nm, which is significantly smaller than the overall particle size of COFs.[160] As a result, it is believed that modifying the local structure within small domains of the COF, rather than across the entire particle, can more effectively enhance charge transfer and thereby improve the photocatalytic performance. To elucidate the structure–activity relationship governing H_2O_2 generation in COFs, Guo *et al.* synthesised a series of quinoline-based COFs bearing different functional groups—COFs-R (R = –OH, –OMe, –H, –Br, –CN)—using a multicomponent reaction (MCR) strategy (Fig. 18e).[161] Inspired by natural enzyme systems, where catalytic efficiency is finely tuned by microenvironmental regulation, the authors introduced these diverse functional groups into the COF. The quinoline backbone, resembling that of glucose oxidase, allows its catalytic behaviour to be modulated by the attached R-groups. The aldehyde and amine building blocks used to construct the framework both contain a triazine core, making these COFs inherently highly electrophilic. Thus, as the electron-donating strength of the substituents increases, the overall donor character of the framework is enhanced, leading to improved D–A charge-separation efficiency. As a result, H_2O_2 generation reaches up to 4458 μmol g^{-1} h^{-1}, with most electron-donating functional

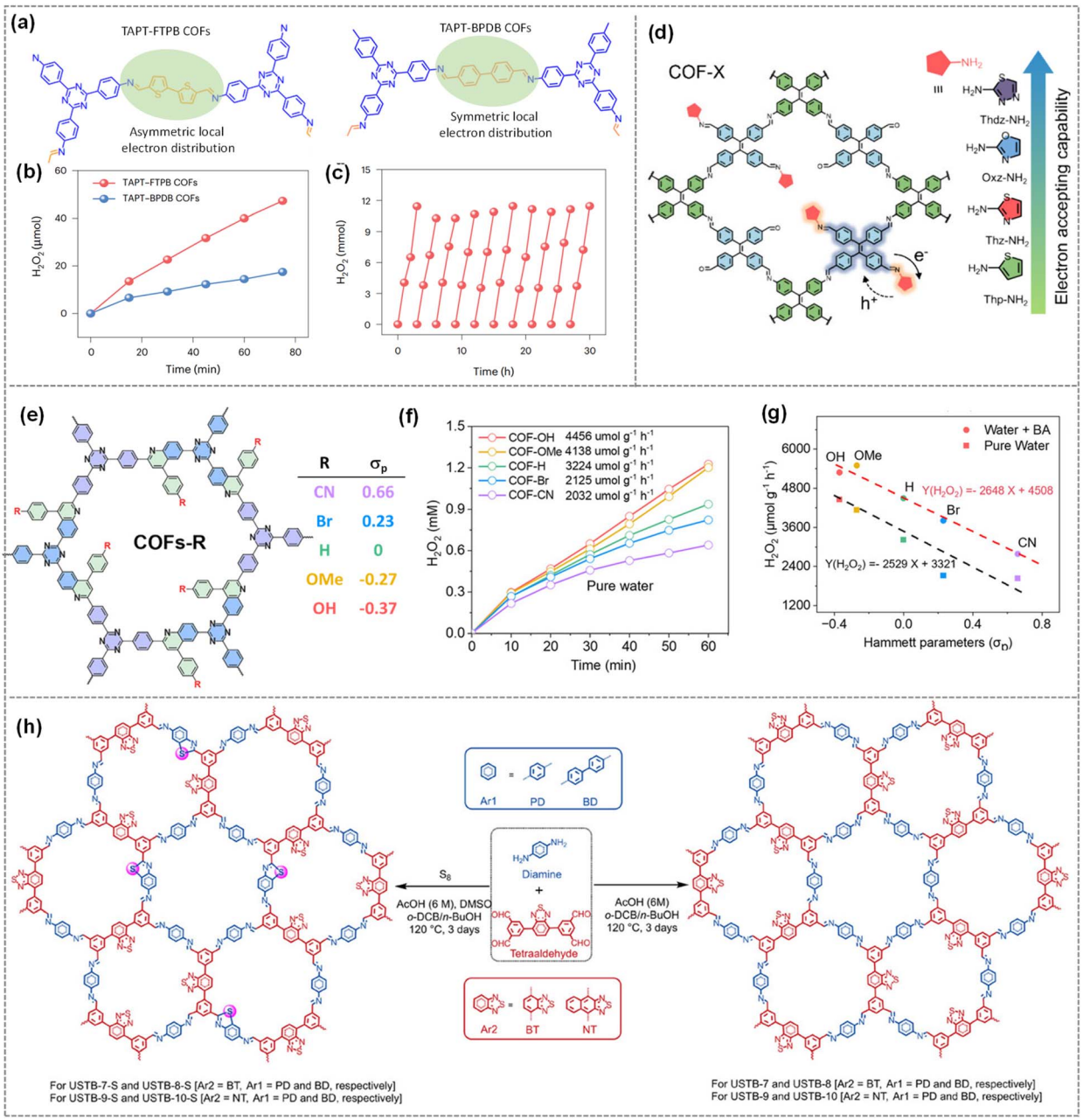

Fig. 18 (a) Structures of TAPT-FTPB-COF and TAPT-BPDB-COF highlighting symmetric and asymmetric local electron distributions. (b) Kinetics of the two COFs for H_2O_2 production. (c) Recyclability experiment of the TAPT-FTPB-COF over 30 h. (Reprinted with permission from ref. 157. Copyright 2025, Springer Nature.) (d) Schematic representation of the structure of the COF synthesised through the one-pot 'grafting-to' approach and its different functional groups. (Reprinted with permission from ref. 158. Copyright 2025, American Chemical Society.) (e) Structure of COFs-R synthesised through a multivariate reaction. (f) Photocatalytic H_2O_2 production comparison of COFs-R. (g) Hammett plot showing the relation between the photocatalytic performance of COFs-R and Hammett parameters. Reproduced and reprinted with permission from ref. 161. (h) Schematic representation of the synthesis of USTB-COF. (Reprinted with permission from ref. 162. Copyright 2024, Wiley-VCH GmbH.)

groups (COF-OH), and with most electron-withdrawing functional groups (COF-CN), it reaches only 2032 μmol g^{-1} h^{-1} (Fig. 18f). This was further evidenced by a similar performance trend in pure water, showing a negative correlation with the Hammett σ_p values of the –R group, irrespective of the presence or absence of a sacrificial agent (Fig. 18g). A change in the local structure of COFs was also achieved by Jiang *et al.* by conducting a three-component solvothermal reaction between diamines, thiadiazole-based tetraaldehydes, and sulfur (Fig. 18h).[162] The reaction yielded mixed USTB-*x*-S (x = 7–10) COFs, which are composed of approximately 90% imine and 10% thiazole linkages. Compared to their fully imine-linked D–A counterparts (USTB-7-10), the USTB-*x*-S series demonstrated significantly enhanced photocatalytic performance, with H_2O_2 production rates increased by 77–95% in pure water under O_2. Notably, USTB-10-S achieved a rate of 5041 μmol g^{-1} h^{-1}, which further

Table 5 Summary of representative microenvironment tuning of COF photocatalysts for H_2O_2 photosynthesis[a]

Sl. no.	Catalyst	Reaction conditions	Dosage (mg) & volume (mL)	H_2O_2 yield (mmol g^{-1} h^{-1})	AQY	SCC	
1	TAPT-FTPB	H_2O and O_2	10 mg & 10 mL	3780	—	1.22%	157
2	COF-Thz	H_2O	2 mg & 40 mL	3701	22.78% @ 420 nm	1.41%	158
3	N_3-COF	H_2O and O_2	10 mg & 50 mL	4820	1.5% @ 420 nm	0.413%	159
4	COF-OMe	H_2O : BA (9 : 1)	5 mg & 18 mL	5497	6.5% @ 420 nm	0.16%	161
5	USTB-10-S	H_2O : BA (1 : 1)	2.5 mg & 25 mL	16 152	4.98% @ 420 nm	0.06%	162

[a] Light irradiation: Xe lamp (λ > 420 nm); BA: benzyl alcohol.

increased to 16 152 μmol g^{-1} h^{-1} upon the addition of benzyl alcohol as a sacrificial agent. This work highlights that the minor local structural modifications in COFs can markedly improve charge separation, thereby boosting photocatalytic performance. The major achievements of the microenvironment tuned COF photocatalyst for H_2O_2 production have been highlighted in Table 5.

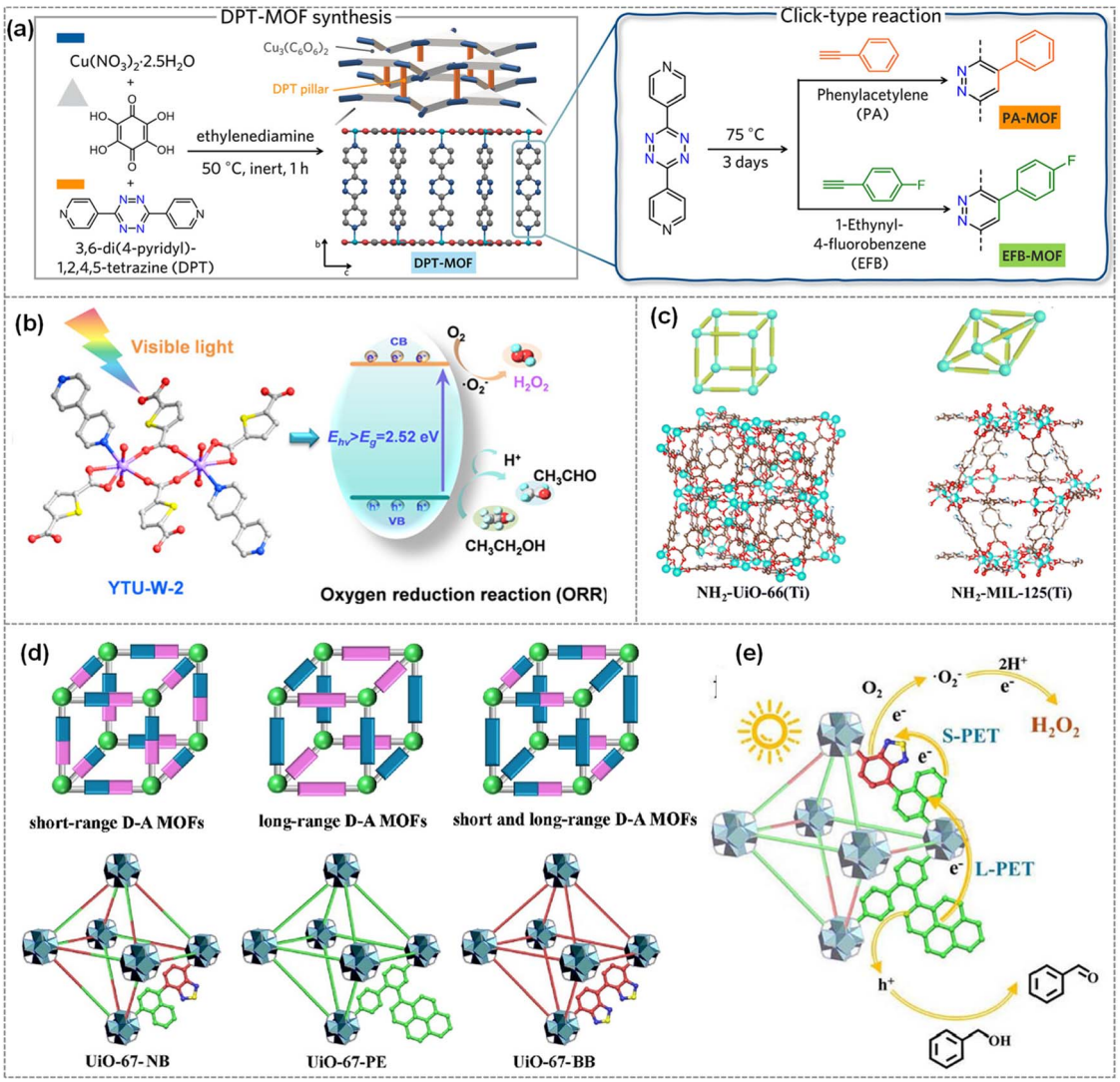

Fig. 19 (a) Schematic route for the synthesis of an electrically conductive MOF and its post-synthetic click reaction. (Reprinted with permission from ref. 181. Copyright 2024, American Chemical Society.) (b) Crystal structure of YTU-W2 and its band gap position towards H_2O_2 production. (Reprinted with permission from ref. 182. Copyright 2024, American Chemical Society.) (c) Isomeric structures of the Ti-based MOF: NH_2-UiO-66(Ti) and NH2-MIL-125(Ti). (Reprinted with permission from ref. 183. Copyright 2024, Royal Society of Chemistry.) (d) Illustration of the strategic installation of different donor and acceptor interaction modes and the structure of synthesised UiO-67-type D–A MOFs. (e) Catalytic pathway for H_2O_2 photoproduction *via* the two-step $2e^-$ ORR on UiO-67-PE/NB. (Reprinted with permission from ref. 187. Copyright 2025, American Chemical Society.)

Metal–organic framework (MOF)-based photocatalysts for H_2O_2 production

MOFs, significant class of crystalline porous materials, comprise metal ions or clusters and organic ligands. They have a large specific surface area, regular and controllable pore structures, and various chemical compositions and functionalities, including the ability to tune the metal centre.[163–166] By altering the kinds of ligands and/or metal nodes, it is possible to rationally tailor the chemical reaction conditions and electrical structures of active centres for specific purposes.[167,168] The increased porosity speeds up mass movement throughout the network of MOFs and encourages the exposure and accessibility of active sites. The high metal content, ordered crystallinity, large surface area, and adjustable pore size of MOFs have made them attractive candidates for various applications, such as catalysis,[169–171] gas storage and separation,[172–174] environmental remediation,[175,176] sensing,[177–179] biomedical applications,[180] *etc*. Towards photocatalysis, the intrinsic photocatalytic properties of MOFs arise from their tunable band structure, photoactive metal nodes, and π-conjugated organic linkers. These features enable efficient light harvesting *via* the antenna effect of linkers, which transfer energy to metal sites through linker-to-metal charge transfer (LMCT), mimicking semiconductor behaviour with adjustable band gaps for visible-light response. Their high porosity and large surface area provide abundant accessible active sites and facilitate mass transport of reactants, while the ordered crystalline framework promotes directional charge transport. Additionally, internal electric fields originating from polar structures or donor–acceptor architectures enhance charge separation and suppress electron–hole recombination. Strong metal–ligand coordination imparts chemical and photostability, and selective adsorption of substrates such as O_2, CO_2, or H_2O further improves catalytic efficiency and selectivity, making MOFs intrinsically well-suited for photocatalytic applications. Recently, Park *et al.* have synthesised copper-based electrically conductive MOFs and introduced a D–A moiety by integrating spatially separated electron D–A moieties *via* a click reaction (Fig. 19a).[181] After the click reaction in MOFs with phenylacetylene (PA) and 1-ethynyl-4-fluorobenzene (EFB), the researcher observed the tuning in the band positions that further aligned with the redox potential of photocatalytic H_2O_2 production. Fluorine incorporation facilitates efficient charge separation by suppressing electron–hole recombination, thereby maximising photocatalytic efficiency. The photosynthesis of H_2O_2 with synthesised MOFs has been explored in pure water and O_2 irradiated with a 300 W Xe lamp. The maximum yield was obtained for the clicked MOF with EFB, and the H_2O_2 production rate of 1676 μmol g^{-1} h^{-1} was reported with an AQY of 1.03% at 410 nm. Toward developing the pristine MOF as an efficient photocatalyst, Wang *et al.* developed an uranyl-organic framework named YTU-W-2 using a mixed ligand strategy where thiophene and pyridine ligands were used (Fig. 19b).[182] The introduction of mixed ligands has increased the photon absorption and carrier transfer into the framework. Furthermore, the H_2O_2 rate of 345 μmol h^{-1} g^{-1} has been reported in a 9 : 1 water and ethanol mixture. The structural effect of pristine MOF towards photocatalytic synthesis of hydrogen peroxide has also been recently studied by Zhang *et al.* by synthesising two isomeric Ti-based MOFs [NH_2-UiO-66(Ti) and NH_2-MIL-125(Ti)] (Fig. 19c).[183] The researchers reported the efficient electron transport of the Ti–O oxygen cluster as NH_2-MIL-125(Ti) has a shorter bond length than NH_2-UiO-66(Ti). Consequently, the photocatalytic activity of NH_2-MIL-125(Ti) was better than that of NH_2-UiO-66(Ti). Furthermore, the defective structure in the MOF was found to acquire more active sites that promote the photocatalytic activity, and the H_2O_2 production of defective NH2-MIL-125 was found to be efficient among all, with a production rate of 101 μmol g^{-1} h^{-1}. Similarly, Zhou and co-workers engineered MIL-125-NH_2, including coexisting (111) and (001) facets, facilitating the formation of a Z-scheme structure to enhance spatial charge separation.[184] A dual-channel pathway for synthesising H_2O_2 was identified, including the ORR on the (111) facets and OH^- oxidation on the (001) facet. The exposure degree of the (111) facet of MIL-125-NH_2 was systematically adjusted by varying the quantities of acetic acid modulator during the preparation process; an increase in acetic acid resulted in a greater exposure modulator during the preparation process; an increase in acetic acid resulted in a greater exposure of (111) facets.[185] The (111) facets may reduce charge transport resistance and extend the lifespan of photo-induced electrons and holes, resulting in an ideal H_2O_2 production rate of 925.8 μmol g^{-1} h^{-1} (visible light, triethanolamine as a sacrificial agent, and pure O_2), in the indirect ORR. In another study, Zhu and co-workers discovered self-assembled tetrakis(4-carboxyphenyl) porphyrin supramolecular photocatalysts that generate H_2O_2 solely from H_2O and O_2, achieving a production rate of 1.72 mM h^{-1} at 293 K, with quantum efficiencies of 14.9% at 420 nm and 1.1% at 940 nm.[186] The catalyst attains an SCC efficiency of 1.2% at 328 K under irradiation and heating with simulated sunlight. The findings indicated that photogenerated electrons and holes facilitate H_2O_2 generation by interacting with distinct active sites, such as the pyrrole N–H ring and carboxyl groups. They specifically suggest a hole-induced H_2O_2 generation method, which entails the photoconversion of –COOH to $-CO_3H$ groups on the catalyst, succeeded by thermal breakdown. Furthermore, after 20 cycles, the buildup of photocatalytic H_2O_2 reached about 50 mM, indicating the materials' strong recyclability. The regulation of D–A interaction mode in Zr-based UiO-67 MOF has been recently reported by Guo *et al.*[187] The author reports the synthesis of a family of UiO-67-type D–A MOFs, in which pyrene, benzothiadiazole, and naphthalene-benzothiadiazole linkers of identical length are co-assembled with Zr_4^+ nodes (Fig. 19d). The precisely tuned short-range (through-bond) and long-range (through-space) D–A interactions were appropriate for the photocatalytic H_2O_2 production from water and O_2 in a water/benzyl alcohol biphasic system. The mixed-linker UiO-67-PENB, the first example of a MOF combining both DA modes in one framework, exhibits an optimised band structure, enhanced charge separation, and suppressed recombination. Consequently, through an indirect two-step $2e^-$ ORR pathway, a high

Table 6 Summary of representative metal–organic framework (MOF) photocatalysts for H_2O_2 photosynthesis

Sl. no.	Catalyst	Reaction conditions	Dosage (mg) & volume (mL)	H_2O_2 yield (μmol g^{-1} h^{-1})	AQY	SCC	Ref.
1	EFB-MOF	H_2O and O_2	5 mg & 30 mL	1676	1.03 @ 410 nm	—	181
2	YTU-W-2	H_2O : EtOH (9 : 1)	10 mg & 50 mL	345	0.073 @ 420 nm	—	182
3	NH2-MIL-125	H_2O and O_2	15 mg & 50 mL	101	—	—	183
4	MIL-125-NH_2[a]	H_2O/TEA and O_2	5 mg & 20 mL	925.8	—	—	184
5	SA-TCPP[a]	H_2O and O_2	25 mg & 50 mL	0.66 mM h^{-1}	14.9% @ 420 nm	1.2%	186
6	UiO-67-PE/BB	H_2O : IPA (9 : 1)	10 mg & 50 mL	5141	4.24% @ 400 nm	—	187
7	Al-P(20AQ)	H_2O and O_2	0.5 g L^{-1}	163.2	4.8% @ 400 nm	0.11%	189

[a] Light irradiation: Xe lamp (λ > 420 nm) except visible light; BA = benzyl alcohol; TEA: triethanolamine.

H_2O_2 formation rate of 5141 μmol g^{-1} h^{-1} and an AQY of 4.24% at 400 nm were achieved. The MOF further demonstrated excellent structural and operational stability over 48 h and H_2O_2 accumulation up to ~32 mM. Comprehensive spectroscopic and electrochemical studies (UV-vis DRS, Mott–Schottky, EIS, photocurrent, PL, fs-TA, EPR, and *in situ* DRIFTS analyses) underpin the mechanistic pathway for H_2O_2 photoproduction as the synergistic photoinduced electron transfer from pyrene to the NB-based DA linker, followed by efficient O_2 reduction and effective hole scavenging by benzyl alcohol (Fig. 19e). This cooperative process enables UiO-67-PENB to outperform the single-mode D–A analogues UiO-67-NB and UiO-67-PEBB in H_2O_2 production and collectively accounts for the superior H_2O_2 photosynthesis performance to both single-mode D–A analogues (UiO-67-NB and UiO-67-PEBB). Toward sustainable H_2O_2 generation and its practical utilisation, Pal *et al.* demonstrated the use of MOFs as an emerging class of thermocatalysts capable of producing H_2O_2 by harvesting small temperature gradients under ambient conditions.[188] In their study, MOFs were immobilised onto carbon fibre fabrics (MOF@CFF) to construct antibacterial filtration systems activated by temperature cycling. Three representative MOFs (CuBDC, MOF-303, and ZIF-8) were evaluated and benchmarked against bismuth telluride (Bi_2Te_3), a well-known thermocatalytic material. Among them, ZIF-8 exhibited the highest H_2O_2 production efficiency under low temperature differences, leading to ~96% antibacterial efficacy against *Escherichia coli* and *Staphylococcus aureus*. This work highlights the potential of MOF-based thermocatalysts for thermoelectric-assisted H_2O_2 generation, offering a promising strategy for real-time water purification and disinfection. Tailoring the morphology and size of photocatalysts has emerged as an effective strategy to enhance H_2O_2 generation by improving charge carrier dynamics and tuning band energetics. For instance, Li and co-workers developed an ultrathin 2D Al-MOF nanosheet of 1 nm (Al-P(AQ)) through the co-assembly of porphyrin (TCPP) as an electron donor and anthraquinone-based ligands (AQCA) as an electron acceptor.[189] The resulting ultrathin framework significantly reduces the diffusion distance for photogenerated charge carriers, thereby facilitating rapid e^- and h^+ transport to the catalyst surface and improving the photocatalytic efficiency. Moreover, incorporation of AQCA alters the electronic structure of the MOF, inducing a downward shift in the LUMO level, narrowing the band gap, and enhancing the thermodynamic driving force for the ORR. The major achievements of the MOF photocatalyst for H_2O_2 production have been highlighted in Table 6.

Porous organic polymer (POP)-based photocatalysts for H_2O_2 production

Porous organic polymers (POPs) are a diverse class of materials known for their highly porous structures, which are constructed from organic monomers that primarily contain light elements such as C, H, O, N, B, *etc.*[190] POPs are primarily synthesised through the polymerisation of organic building blocks into macromolecular frameworks. POPs possess various properties that make them ideal for photocatalysis such as high porosity, large surface areas, and tunable extended π-conjugated structures that enable broad visible-light absorption and efficient exciton generation. Their lightweight nature, excellent chemical/thermal stability, and pre-designable D–A building blocks facilitate superior charge separation, reduced recombination, and precise modulation of band gaps and redox potentials for targeted photocatalytic reactions. Unlike COFs, POPs can be synthesised under milder conditions, feature irreversible covalent bonds that impart greater robustness, and avoid harsh crystallisation steps. POPs can be further classified into two categories based on their long-range order, such as crystalline and amorphous POPs.[191] COFs and covalent triazine frameworks (CTFs) are well-known crystalline POPs, and some examples of amorphous POPs are porous aromatic frameworks (PAFs), hypercrosslinked polymers (HCPs), polymers of intrinsic microporosity (PIMs), and conjugated microporous polymers (CMPs), *etc.* The high crystallinity in a material can significantly promote electron/hole separation, reduce their possible recombination, and enhance the photocatalytic activity.[192,193] Therefore, various reports could be seen regarding the development of crystalline POPs for the photosynthesis of H_2O_2, such as COFs, as discussed above. CTF is also a crystalline POP, distinguished by its aromatic C–N linkage (triazine unit) and lack of weak bonds. Strong aromatic covalent connections mainly impart CTFs with high nitrogen content and excellent chemical stability, which are valuable for various real-world uses and the intriguing heteroatom effect (HAE). Because of their unique qualities, CTFs are appealing for several uses, including energy storage, photocatalysis, heterogeneous catalysis, and gas separation and storage. CTFs may be divided into two groups based on the state of research: crystalline and

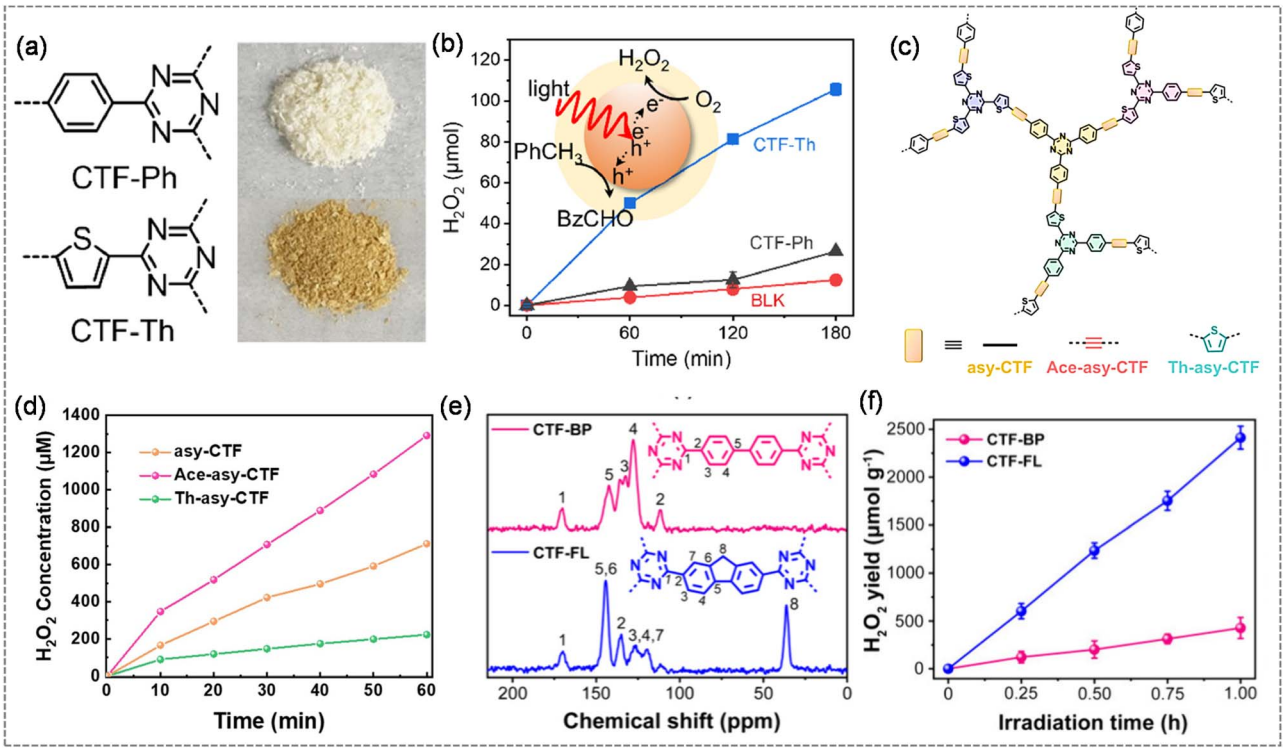

Fig. 20 (a) Donor–acceptor type covalent triazine frameworks, CTF-Ph and CTF-Th and (b) photocatalytic production of H_2O_2 in 50% toluene in acetonitrile under saturated O_2 conditions. (Reprinted with permission from ref. 199. Copyright 2023 Elsevier). (c) Schematic illustration of the stepwise charge transfer within the CTF and (d) time course of H_2O_2 evolution over CTFs (300 W xenon lamp with a 400 nm cutoff filter; light intensity: 100 mW cm^{-2}). (Reprinted with permission from ref. 200. Copyright 2024, American Chemical Society.) (e) ^{13}C CP-MAS NMR spectra of CTF-BP and CTF-FL and (f) time course of photocatalytic H_2O_2 production (λ > 420 nm, 300 W xenon lamp; 10 mg of catalyst in 100 mL of pure water; O_2-saturated, 25 °C). (Reprinted with permission from ref. 201. Copyright 2024, American Chemical Society.)

amorphous CTFs. The kind of monomers and the synthesis procedure have a significant impact on the characteristics of CTFs. In recent years, significant research has been done on synthesis techniques such as aldehyde–amidine condensation, trifluoromethanesulfonic acid-catalysed synthesis, amino-aldehyde synthesis, and ionothermal polymerisation.[194,195] CTFs are promising semiconductor candidates for photocatalysis, including the photodegradation of organic pollutants, the conversion of chemical molecules, the splitting of water, the reduction of CO_2, and more, due to their abundance of nitrogen, strong conjugated structure, and absorption of visible light.[196–198] By altering the phenyl and thiophene moieties, J. Byun and colleagues have synthesised two CTFs with adjustable D–A character, demonstrating that regulating the oxidative reaction medium significantly affects photocatalytic H_2O_2 generation (Fig. 20a).[199] The photocatalytic H_2O_2 generation ability of CTFs was assessed under both aqueous and non-aqueous conditions. The O_2 reduction process, in conjunction with toluene oxidation, is specifically made possible by CTF-Th, which has more thiophene donors. This results in a large generation of H_2O_2 up to 105 μmol, which is 4.7 and 2.5 times higher than those of H_2O (22.3 μmol) and H_2O/alcohol (42.4 μmol) oxidation, respectively (Fig. 20b). According to the theoretical computation, benzaldehyde and H_2O_2 can be produced simultaneously on CTF surfaces due to the binding affinities of toluene and O_2, respectively. Toluene and water layers form a dual-phase system that makes it easy to separate the two very pure products. Inspired by the sequential energy- and charge-transfer processes from PS II to PS I in natural photosynthesis, K. A. I. Zhang and colleagues developed and synthesised three CTF photocatalysts with stepwise charge transfer (Fig. 20c).[200] They created effective CTFs for high-efficiency photosynthesis of H_2O_2 from water and O_2 without the use of sacrificial agents by carefully designing linkers with different degrees of conjugation to act as electron transfer spacers and photocatalytic ORR centres between the four molecular donor–acceptor domains (M1–M4) in the asymmetric CTF framework. The acetenyl moiety improved the spontaneous O_2 adsorption in the CTFs compared to the heavily conjugated thiophene moiety. Because Ace-asy-CTF's acetylene moiety effectively lowers the energy barrier for the stepwise two-electron ORR, it has a higher photocatalytic H_2O_2 production efficiency than Th-asy-CTFs with strong conjugated thiophene units or asy-CTF without a spacer. This results in an enhanced photocatalytic H_2O_2 yield (2594 μmol g^{-1} h^{-1}, Fig. 20d) with an SCC of 0.48% without sacrificial agents. By creating and manufacturing two highly crystalline layered CTFs using 1,1′-biphenyl-4,4′-dicarbonitrile (BP-CN) and 9*H*-fluorene-2,7-dicarbonitrile (FL-CN) as the building blocks for the first time, Xu and colleagues created high-performance metal-free photocatalysts (Fig. 20e).[200,201]

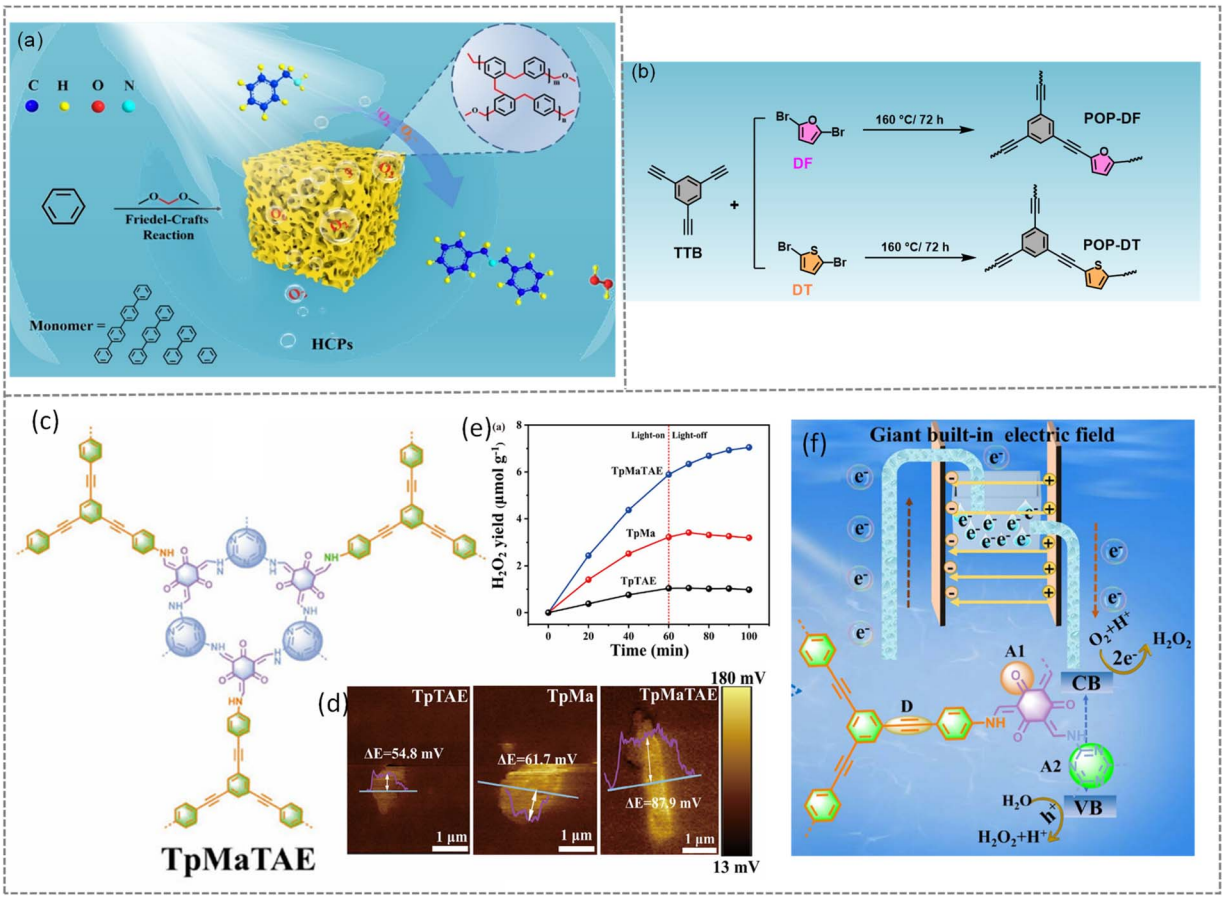

Fig. 21 (a) Schematic illustration of the synthesis of different HCPs for benzylamine oxidation and H_2O_2 production. (Reprinted with permission from ref. 204. Copyright 2024, Wiley-VCH GmbH.) (b) Schematic of the synthesis of POP-DT and POP-DF. (Reprinted with permission from ref. 205. Copyright 2024, Royal Society of Chemistry.) (c) Structural representation of TpMaTAE. (d) Surface potential values of TpMa, TpTAE, and TpMaTAE. (e) Photocatalytic H_2O_2 production with TpMa, TpTAE, and TpMaTAE when light is on and off. (f) Mechanism of H_2O_2 production and the built-in an electric field and the schematic of the synthesis of POP-DT and POP-DF. (Reprinted with permission from ref. 208. Copyright 2024, Wiley-VCH GmbH.)

The direct photosynthesis of H_2O_2 generation on the as-prepared crystalline CTFs with a locked-in coplanar conformation has been significantly improved by utilising logical control of the torsion angle in the basal plane of the CTFs (Fig. 20f). The exfoliated few-layer crystalline 2D triazine polymer nanosheets from the bulk CTF exhibit a remarkable SCC efficiency of 0.91% at a low catalyst concentration (0.5 g L^{-1}) and a noteworthy AQY of 16.8% at 420 nm, demonstrating an excellent photocatalytic H_2O_2 production rate of up to 5007 μmol g^{-1} h^{-1} from oxygen and water without sacrificial agents. A series of CTFs with different numbers of acetylene groups were reported by H. Xu and colleagues as metal-free photocatalysts for the generation of H_2O_2. Acetylene or diacetylene moieties may be added to CTFs to increase photocatalytic H_2O_2 production significantly.[202] The integrated carbon–carbon triple bonds, which are crucial for adjusting the electrical structures of CTFs and preventing charge recombination, impart this natural improvement. Additionally, the acetylene and diacetylene moieties can drastically lower the energy required to generate OH*, opening up a novel two-electron oxidation route that produces H_2O_2. After 24 h, the H_2O_2 generation of CTF-BDDBN with two acetylene centres was greater than that of CTF-EDDBN with one acetylene moiety (39 μmol) and CTF-BPDCN without an acetylene moiety (21 μmol). Li and colleagues demonstrated how to increase the electrical conductivity of CTF by ten times for excellent, highly conductive carbon quantum dots (CQDs) as an electron transport medium inside the CTF pores.[203] In pure water, without any sacrificial agent, the optimised CQD-CTF (0.5 wt%) shows a high H_2O_2 production rate of up to 1036 μmol g^{-1} h^{-1} under visible light, 4.6 times that of CTF. According to this study, the presence of CQDs will improve the performance of charge separation and migration with higher electronic conductivity. The greater negative zeta potential, which can significantly trigger the ORR process, may also increase the affinity of H^+. Additionally, photocatalysis increases the oxidation capacity, which benefits the WOR process. This work offers a novel approach to the practical H_2O_2 synthesis of low-conductivity organic semiconductors. Despite the challenges associated with amorphous POPs, such as low crystallinity, weak light absorption in the visible spectrum, poor separation of photogenerated carriers, and limited structural diversity, which hinder photocatalytic performance, there are only a few

Table 7 Summary of representative porous organic polymer (POP) photocatalysts for H_2O_2 photosynthesis

Sl. no.	Catalyst	Reaction conditions	Dosage (mg) & volume (mL)	H_2O_2 yield (μmol g^{-1} h^{-1})	AQY	SCC (%)	Ref.
1	CTF-Th	H_2O : IPA (9 : 1) and O_2	50 mg & 30 mL	43 μmol in 3 h	—	—	199
2	Ace-asy-CTF	H_2O and O_2	5 mg & 10 mL	2594	4.4% @ 420 nm	0.48	200
3	CTF-NSs	H_2O and O_2	10 mg & 100 mL	5007	16.8% @ 420 nm	0.91	201
5	0.5 CQD-CTF[a]	H_2O and O_2	5 mg & 20 mL	1036	1.03% @ 420 nm	0.21	203
6	QP-HCP	CH_3CN and BAm	10 mg & 20 mL	9300	—	—	204
7	POP-DT	H_2O and O_2	10 mg & 50 mL	2422.2	2.67% @ 400 nm	—	205
8	TEADP-POF	H_2O and O_2	30 mg & 50 mL	2136	2.39% @ 400 nm	—	206
9	TEAPYRI-COP	H_2O and O_2	30 mg & 50 mL	2884	3.27% @ 400 nm	—	207
10	TpMaTAE	H_2O and O_2	5 mg & 50 mL	6280	—	1.03	208
11	CTF-BTT	H_2O/BA and O_2	5 mg & 50 mL	74 956	7.61% @ 420 nm	0.66	209
12	CTF-DA-film-3[a]	H_2O and O_2	Thin film	8920	1.242% @ 450 nm	0.12	210
13	BPYTEA-POF	H_2O and O_2	30 mg & 20 mL	3446	—	—	211

[a] Light irradiation: Xe lamp (λ > 420 nm) except visible light; IPA: isopropyl alcohol; BAm: benzylamine.

reports focusing on their development for photocatalytic H_2O_2 production. For instance, Nie *et al.* have reported the photocatalytic efficiency of four HCP photocatalysts with different arene monomers towards photocatalytic H_2O_2 production.[204] A series of HCPs have been synthesised by a facile Friedel–Crafts alkylation reaction of different arene monomers, which include benzene (BE), diphenyl (DP), *p*-terphenyl (TP), and *p*-quaterphenyl (QP) (Fig. 21a). Amongst all, HCP with a QP group has the optimal separation and transfer efficiency of photogenerated e^-–h^+ due to the higher degree of conjugation of the QP monomer. The efficiency of synthesised HCPs has been evaluated towards photocatalytic H_2O_2 production in acetonitrile and benzylamine under blue LED irradiation. The H_2O_2 production rate for BE, DP, TP, and QP was observed to be 6.0, 6.8, 7.8, and 9.3 mmol g^{-1} h^{-1}, respectively. Recently, Wang *et al.* have reported the synthesis of two alkynyl-containing POP (POP-DT and POP-DF) *via* the Sonogashira cross-coupling reaction between the acetylene-based monomer and thiophene or furan monomer (Fig. 21b).[205] The authors report that the acetylene moieties in the framework acted as the oxygen-reducing active site, while the thiophene or furan ring functioned as the electron donor unit. Furthermore, the integration of acetylene and thiophene facilitated faster charge separation and improved charge transfer efficiency, thereby greatly enhancing the kinetic performance of the oxygen reduction reaction. Therefore, the H_2O_2 production rate of POP-DT, under visible light irradiation, reached 2422.2 μmol g^{-1} h^{-1}, which was 4.3 times higher than that of POP-DF, representing one of the best performances ever observed for polymeric photocatalysts. The coordination of the pyridine moiety with the acetylene-based monomer has also proved to be efficient for H_2O_2 photosynthesis. In this context, Wen *et al.* have synthesised TEADP-POF by reacting tris(4-ethynylphenyl)amine (TEA) with 2,5-dibromopyridine (DP) and TEADB-POF with dibromobenzene.[206] Triphenylamine functions as the electron-donating unit, while pyridine serves as the electron acceptor, enabling a push–pull effect within the 2D π-conjugated framework that facilitates charge separation and transfer. Consequently, H_2O_2 production at a rate of 2136 μmol g^{-1} h^{-1} was obtained with TEADB-POF from H_2O and O_2. Similarly, the same group investigated photocatalytic H_2O_2 production in conjugated organic polymers through active-site position engineering. In this approach, 2,5-dibromopyrazine and 3,6-dibromopyrazine were employed in place of DP to synthesise TEAPYRA-COP and TEAPYRI-COP, respectively.[207] TEAPYRI-COP, containing adjacent pyridazine nitrogen sites, exhibits stronger hydrogen-bonding with water compared to TEAPYRA-COP, where nitrogen atoms are positioned oppositely. This configuration facilitates O–H bond activation, enhances water oxidation to generate protons, and promotes efficient H_2O_2 formation *via* O_2 reduction. Additionally, the adjacent nitrogen sites in TEAPYRI-COP stabilise key intermediates through a low-energy six-membered transition state, improving the $2e^-$ ORR pathway. As a result, TEAPYRI-COP achieves a significantly higher H_2O_2 production rate (2884 μmol g^{-1} h^{-1}), approximately 3.5 times greater than that of TEAPYRA-COP under visible light without additives. The major achievements of the POP photocatalyst for H_2O_2 production have been highlighted in Table 7.

In a study, Zhu *et al.* reported the synthesis of TpMaTAE by multicomponent Schiff-base polycondensation of Tp-aldehyde, melamine (Ma), and 1,3,5-tris(4-aminophenyl)benzene (TAE).[208] The reaction resulted in a covalently integrated acetylene donor with dual acceptors (triazine and carbonyl) and yields an amorphous, high-surface-area, fibrous COP with a strong built-in dipole and enhanced O_2 adsorption (Fig. 21c). Band-structure analysis reveals visible-light absorption, suitable band edges for the $2e^-$ ORR/WOR, and reduced exciton binding energy. Also, Kelvin probe force microscopy (KPFM) and surface charge measurements confirm a much stronger internal electric field than in D–A analogues TpTAE and TpMa (Fig. 21d). Consequently, TpMaTAE achieves an H_2O_2 production rate of 5860 μmol g^{-1} h^{-1} from air and 7830 μmol g^{-1} h^{-1} (Fig. 21e) under AM 1.5G with SCC values of 1.03% and 93.1% for O_2 utilisation. Mechanistic analyses supported by experimental data reveal a stepwise single-electron $2e^-$ ORR *via* O_2- and one-step $2e^-$ WOR pathways (Fig. 21f). Spectroscopy (fs-TAS and TRPL), together with EIS, OCVD, and light-induced EPR, shows that the D–A_1–A_2 architecture significantly improves exciton dissociation and reduces charge-transfer resistance. These measurements also reveal prolonged charge-carrier lifetimes and

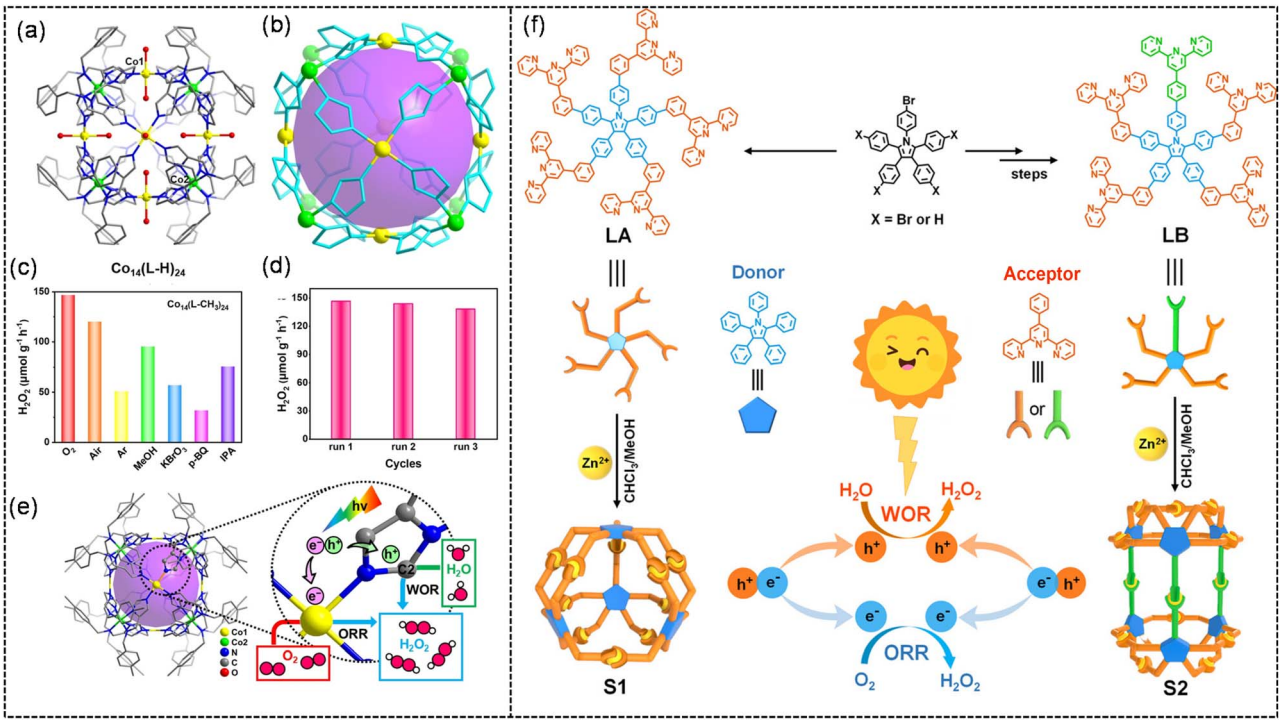

Fig. 22 (a) Crystal structure of $(Co_{14}(L\text{-}H)_{24})$, (b) polyhedral representation of $(Co_{14}(L\text{-}H)_2)$, (c) photocatalytic performances of H_2O_2 production by $Co_{14}(L\text{-}CH_3)_{24}$ in pure water and different atmospheres, and (d) recyclability of $Co_{14}(L\text{-}CH_3)_{24}$ after photosynthesis of H_2O_2. (e) Catalytic sites in $Co_{14}(L\text{-}CH_3)_{24}$ for the ORR and OER (Reprinted with permission from ref. 219. Copyright 2023, Wiley-VCH GmbH.) (f) Schematic representation for the synthesis of S1, S2, and their photocatalytic H_2O_2 production. (Reprinted with permission from ref. 220. Copyright 2025, Wiley-VCH GmbH.)

a higher density of stored electrons in TpMaTAE. In addition, *in situ* FTIR and dark H_2O_2 generation experiments confirm that the carbonyl groups function as electron reservoirs. This stored charge enables continued H_2O_2 formation even after the light is switched off.

Metal–organic polyhedra (MOP)-based photocatalysts for H_2O_2 production

Metal–organic cages (MOC) or metal–organic polyhedra (MOP) are an old but rarely explored subclass of AFPMs.[212,213] MOPs are attractive for their structural similarity to MOFs, except that they have to cap terminal groups that prevent indefinite extension into networks, making them discrete molecules.[214] From the standpoint of the metal cation or cations and the organic linkers used in their self-assembly, MOP has demonstrated synthetic flexibility. The interior cavity, allowing guest molecules to be absorbed, is a distinguishing feature of these materials. Consequently, coordination cages have found utility in a wide range of applications, including molecular recognition and separation, host–guest chemistry, catalysis, and biological applications.[215–218] In contrast to polymeric materials, MOP photocatalysts with well-defined active sites enable clear elucidation of structure–mechanism–performance relationships. Their photophysical properties can be precisely tuned through atomic-level modifications, leading to exceptional catalytic activity and attracting growing attention in recent years. MOPs are particularly advantageous due to their precisely controllable geometries, well-defined pore sizes, tunable electronic structures, and broad photoresponse windows. Furthermore, MLCT enhances the reactivity of the photoexcited states, while synergistic metal–ligand interactions promote efficient charge separation. Despite this, the photocatalytic applications of MOPs are less explored compared to other AFPMs. The first work with MOP for photocatalytic H_2O_2 production was reported in 2023, where Y. Q. Lan and co-workers reported two Co-MOCs $(Co_{14}(L\text{-}H)_{24}$ and $Co_{14}(L\text{-}CH_3)_{24})$ integrated with an imidazole-based ligand (Fig. 22a and b).[219] The photocatalyst's light absorbance is enhanced, and the recombination efficiency of photogenerated electrons and holes is decreased due to MOC functionalization. According to theoretical simulations, the CH_3 functionalized ligand is better suited to adsorb the important *OH and *HOOH intermediates produced by the WOR and ORR. $(Co_{14}(L\text{-}CH_3)_{24})$ exhibits a higher H_2O_2 generation rate of 146.60 μmol g^{-1} h^{-1} in O_2-saturated water, and subsequently, the MOP photocatalyst could produce a significant amount of H_2O_2 under different conditions such as air, MeOH and IPA (Fig. 22c). The catalyst can be recycled up to three cycles with a nominal decrease in the yield (Fig. 22d). Isotope tracing experiments and comparative studies show that for these two catalysts, the Co site acts as the reduction site, allowing the synthesis of H_2O_2 *via* the $2e^-$ two-step ORR route, while the imidazole site from the ligand acts as the oxidation site, producing H_2O_2 *via* the $2e^-$ two-step WOR pathway (Fig. 22e). More significantly, in these Co(II)-based supramolecular cages,

the imidazole site directly coordinates with the Co site, reducing the spatial separation between the oxidation and reduction sites and increasing the charge migration efficiency, which in turn increases the catalytic activity of photocatalytic H_2O_2 synthesis. Similarly, Xiao *et al.* present a novel supramolecular approach for photocatalytic H_2O_2 production using discrete, non-noble MOCs, overcoming key limitations of conventional polymeric and framework-based photocatalysts.[220] Unlike MOFs or COFs, these cages offer atomic-level control over active sites, enabling direct correlation between the structure, photophysical properties, and catalytic performance. Two Zn-based metallo-cages (S1 and S2) were rationally designed and synthesised with distinct electronic and photophysical properties (Fig. 22f). The atomic-level control over active sites and charge-transfer pathways, with S2, exhibits high structural stability, low exciton binding energy, ultrafast intramolecular electron transfer, and prolonged excited-state lifetimes, all of which promote efficient charge separation. A bottom-up nano-sizing strategy was further employed by dispersing MOCs in DMF to generate ultrasmall, well-dispersed catalytic particles, significantly enhancing substrate accessibility and reaction kinetics. The photocatalytic H_2O_2 production was carried out in a H_2O : DMF (9 : 1) solution using $Na_2C_2O_4$ as a sacrificial agent, and an exceptionally high H_2O_2 production rate of 77 401 μmol g^{-1} h^{-1} with an SCC efficiency of 0.97% was achieved. Mechanistic studies reveal that the cage architecture facilitates simultaneous $2e^-$ ORR and WOR pathways, while $Na_2C_2O_4$ suppresses charge recombination and provides a kinetically favourable route for superoxide radical formation, collectively overcoming bottlenecks for the ORR and enabling efficient and stable H_2O_2 production.

Hydrogen-bonded organic framework (HOF)-based photocatalysts for H_2O_2 production

Hydrogen-bonded organic frameworks (HOFs) are a class of porous crystalline materials formed by organic molecules linked through hydrogen bonding and other intermolecular forces.[221,222] Although HOFs were proposed as porous materials in the 1990s, it was not until 2010 that their permanent porosity was confirmed through gas sorption studies.[223,224] Most HOFs, constructed through weak intermolecular forces, generally exhibit lower stability compared to MOFs and COFs, which are built *via* coordination or covalent bonds. Nevertheless, the

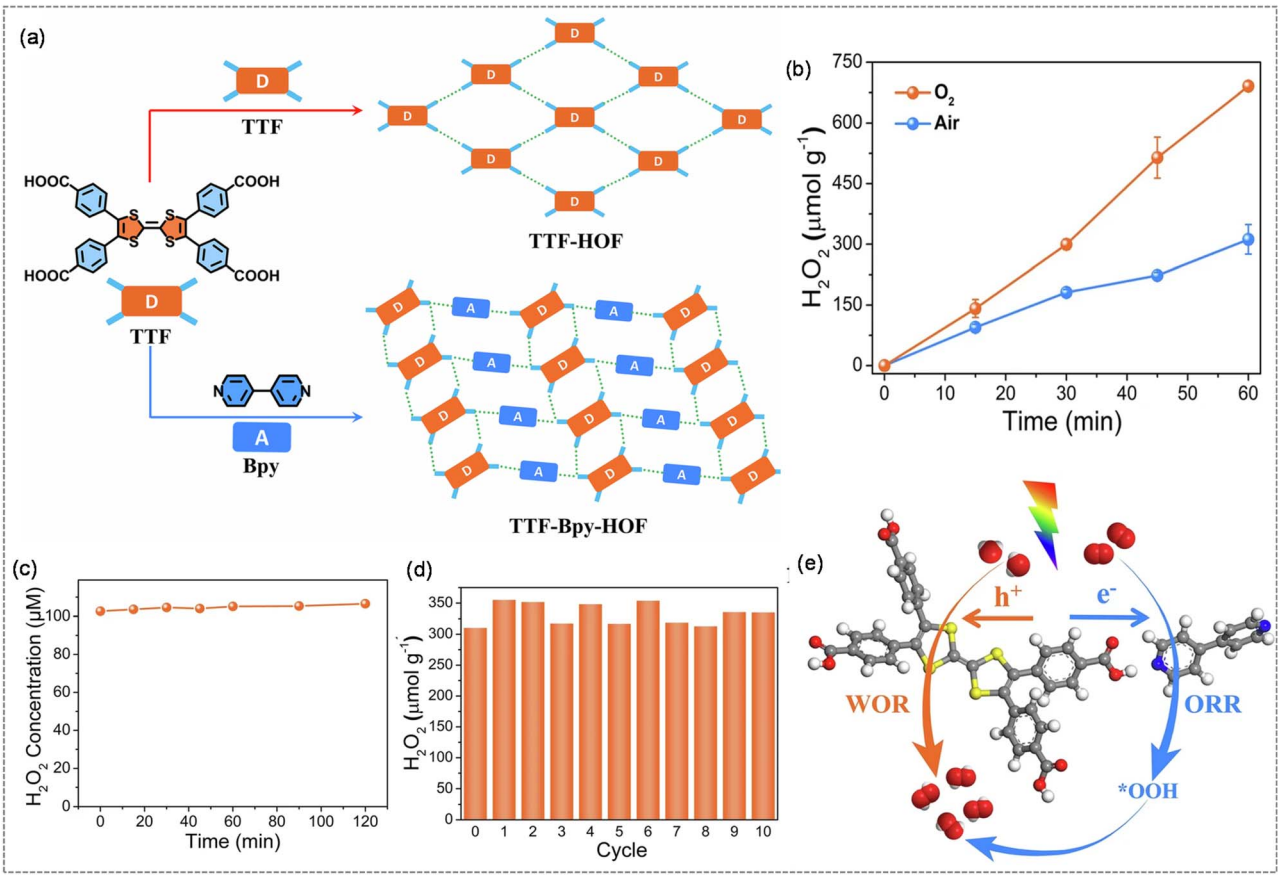

Fig. 23 (a) Schematic representation of D–A HOF synthesis. (b) Time-dependent production of H_2O_2 by the TTF-Bpy-HOF in an O_2 and air-saturated solution. (c) H_2O_2 decomposition study by the TTF-Bpy-HOF in reaction medium. (d) Recycle experiment of the TTF-Bpy-HOF for H_2O_2 photosynthesis over 10 cycles. (e) Schematic diagram of the photosynthesised H_2O_2 through the ORR and WOR pathways. (Reprinted with permission from ref. 228. Copyright 2025, Springer Nature.)

overall stability of HOFs can be significantly enhanced through synergistic effects of hydrogen bonding, π–π stacking, electrostatic interactions, and framework interpenetration.[225] The π–π stacking interactions in HOFs not only enhance structural stability but also play a functional role in facilitating efficient electron transfer. As a result, HOFs have emerged as promising photocatalysts for various applications, including H_2 production[226] and CO_2 reduction.[227] Recently, Zhong *et al.* have reported the D–A HOF (TTF-Bpy-HOF) towards photocatalytic H_2O_2 production from H_2O and O_2 by reacting electron-rich tetrathiafulvalene tetracarboxylic acid (TTF) and electron-deficient 4,4′-bipyridine (Bpy) as the electron-accepting units (Fig. 23a and b).[228] The TTF-Bpy-HOF demonstrated a significantly enhanced photocatalytic performance, achieving a maximum H_2O_2 production rate of 681.2 μmol g^{-1} h^{-1} (Fig. 23c). In contrast, the Bpy-free counterpart, TTF-HOF, exhibited much lower efficiency, with a production rate of only 74.4 μmol g^{-1} h^{-1}. The HOF demonstrated excellent recyclability, retaining its photocatalytic efficiency over 10 consecutive cycles, showcasing its structural integrity over prolonged H_2O_2 production. The photodecomposition of H_2O_2 over the TTF-HOF and TTF-Bpy-HOF was evaluated under light irradiation. The H_2O_2 concentration remained essentially unchanged over 2 h, confirming its stability in the presence of these materials under illumination. Mechanistic studies reveal that H_2O_2 formation in the HOF system proceeds *via* both the $2e^-$ ORR and WOR pathways. As illustrated in Fig. 23d, under visible-light irradiation, the TTF units in TTF-Bpy-HOF absorb photons, generating separated electron–hole pairs. The photogenerated electrons migrate to the Bpy moieties, while holes remain on the TTF units, enabling spatially separated redox reactions. Water oxidation proceeds on the TTF units *via* a direct $2e^-$ pathway to produce H_2O_2, whereas O_2 reduction occurs on the Bpy units through a two-step $2e^-$ process involving $^{\bullet}O_2^-$ intermediates, ultimately yielding H_2O_2.

AFPM-based composites for photocatalytic H_2O_2 production

One of the key advantages of functional porous materials is the vast potential for post-synthetic modification (PSM), thanks to their rigid framework and large surface area.[229] Functionality that cannot be directly incorporated into functional porous materials during *de novo* synthesis can be introduced through post-synthetic modification (PSM) strategies. In the case of COFs, there are current strategies for the PSM COF involving (i) incorporation of a variety of active metal species by using metal complexation through coordination chemistry, (ii) covalent bond formation between existing pendant groups and incoming constituents and (iii) chemical conversion of linkages. (iv) A monomer truncation strategy for the internal functionalization of COFs sometimes assists post-synthetic modification. Current strategies for post-synthetic modification (PSM) of COFs include (i) encapsulation of various active species without covalent threading, (ii) formation of covalent bonds between functional groups of COFs and active species, (iii) chemical conversion of linkages into desired active sites and (iv) the use of a monomer truncation strategy to assist in the functionalization of COFs. In PSMs, COFs can be utilised as a host or template to encapsulate or wrap other substances, such as metal nanoparticles, organic molecules, or other porous materials, and the material synthesised is generally referred to as COF composites. These composites leverage the unique properties of COFs while enhancing the functionality by including complementary substances. The resulting COF composites often exhibit synergistic properties beneficial for desired applications.[229] Cong *et al.* have reported the synthesis of two novel polyimide COF (MPa-COFs/CQDs and MNd-COFs/CQDs) composites using different types of dianhydrides and carbon quantum dots (CQDs) *via* a one-pot hydrothermal method.[230] The CQDs on COFs were loaded by treating the synthesised COF with D(+) glucose and heating it in a Teflon-lined stainless-steel autoclave at 160 °C for 3 h. After the introduction of CQDs, both photocatalytic and electronic properties of polyimide COFs were boosted, and suppression of photoinduced electrons and holes recombination was also noticed. The photocatalytic activity of two COF composites for H_2O_2 production was evaluated using pure water and O_2 under visible light irradiation, and the highest production yield of up to 540 μmol g^{-1} h^{-1} was observed for MPa-COFs/CQDs-2. The synthesis of the COF composite with the desired heterojunction has also been a topic of interest for many researchers. As organic semiconductors, COFs can be combined with suitable inorganic semiconductors to form various types of heterojunctions, significantly enhancing redox capacity regarding thermodynamics and -kinetics.[231] In that context, Wong *et al.* have combined the D–A conjugated TpMA-COF with an inorganic semiconductor CdS by the hydrothermal method and report the formation of S-scheme heterojunctions.[232] The formation of the heterojunction enhanced the photocatalytic activity of the composites. To optimise the catalyst, various amounts of CdS were loaded onto the COF, with the resulting catalysts being named CT-5, CT-10, CT-15, CT-20, and CT-30. The photocatalytic activity of the COF composite material towards H_2O_2 production was evaluated using pure water under simulated sunlight. The H_2O_2 production yield of CT-10 was found to be the highest, with a production rate of up to 608.41 μmol L^{-1} in 90 min. Similar work has also been reported by Xia *et al.* by constructing a heterojunction on the TpPa-1 COF through the incorporation of $ZnIn_2S_4$ nanosheets on the COF.[233] The COF composite, $ZnIn_2S_4$/TpPa-1, with a hierarchical heterostructure, could produce H_2O_2 at a rate of 516 μmol L^{-1} under visible light irradiation, which is almost three times higher than that of individual COF and $ZnIn_2S_4$ catalysts. In a quest for synthesising COF composites with improved photocatalytic activity, Wang *et al.* have incorporated tungsten oxide (WO_3) into the Tp-TAPB-COF and report the formation of the WO_3/Tp-TAPB composite bearing a Z-scheme heterojunction.[234] The Z-scheme heterojunction has promoted the separation of useful e^-–h^+ pairs, and the overall composites have enhanced light absorption properties. To get the optimum catalyst, the amount of WO_3 was varied from 5 mg to 40 mg and named *X*WO_3/Tp-TAPB, where $X = 10$, 20, 30, and 40, respectively. The photocatalytic activity of different COF

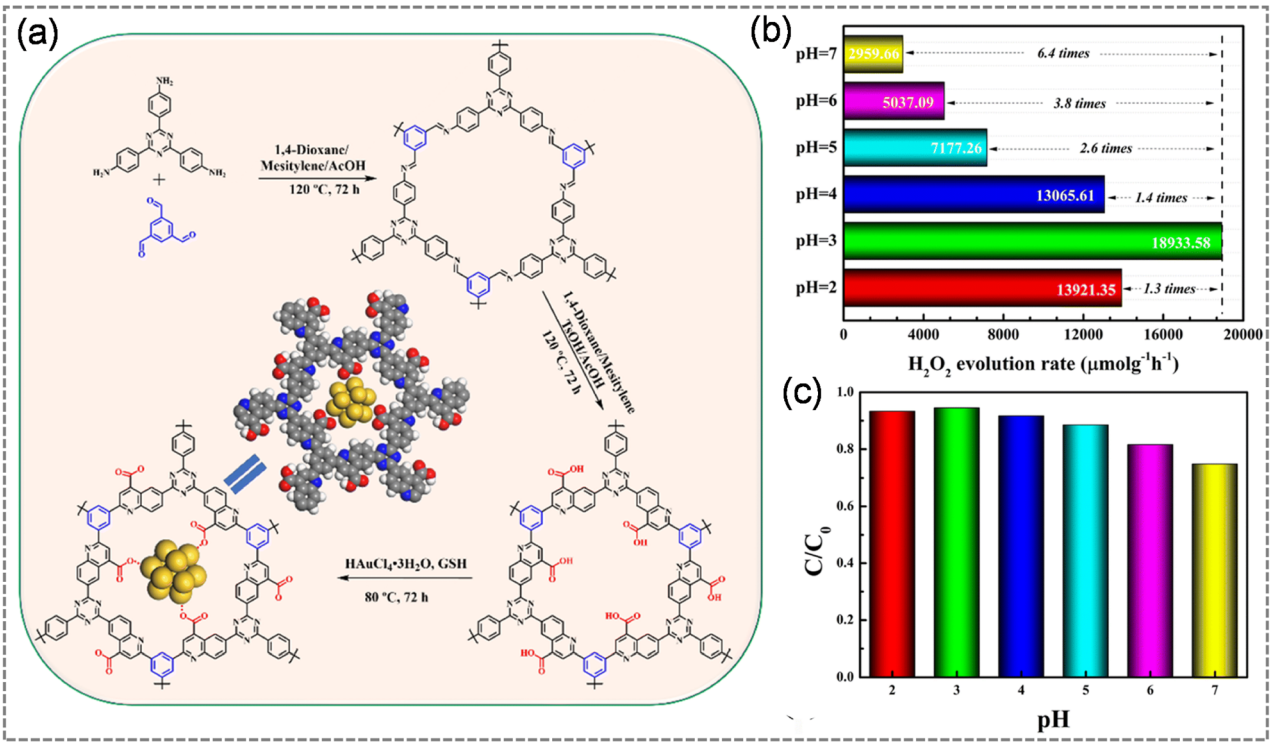

Fig. 24 (a) Synthetic route for the covalently treated Au@COF composite. (b) Photocatalytic H_2O_2 production of the Au@COF at different pHs. (c) The photocatalytic decomposition of H_2O_2 (200 mM) over the Au@COF at different pHs. (Reprinted with permission from ref. 235. Copyright 2023, Royal Society of Chemistry.)

composites was evaluated in pure water and oxygen under irradiation of LED light with a wavelength >420 nm. Amongst all the COF composites, the catalytic activity of 20WO_3/Tp-TAPB was found to be optimum towards light-driven H_2O_2 production with a rate of 1488.4 μmol h^{-1} g^{-1}. Towards the PSM of COFs and encapsulation of metal nanocrystals (NCs), Shang *et al.* have reported a novel strategy by generating anchoring sites within the framework of COFs that bind targeted NCs.[235] To achieve this, the TAPT-COF was first synthesised solvothermally and then decorated with carbonyl groups using the well-known Doebner–Miller reaction (Fig. 24a). The carbonyl groups acted as anchoring sites, and upon treatment of the functionalised COF with $HAuCl_4 \cdot 3H_2O$, gold NCs (Au NCs) were incorporated into the pores of the COF (Fig. 24a). Additionally, the carbonyl groups within the COF served as a bridge. The Au NCs incorporated into the COF enhanced charge transfer and catalytic activity, while the COF provided structural stability and a high surface area for efficient H_2O_2 production. The Au modified COF (Au@COF) has shown the photocatalytic H_2O_2 production rate of 18 933.58 μmol g^{-1} h^{-1} at pH = 3 (Fig. 24b). Also, the decomposition rate of H_2O_2 over Au@COF was merely 5.5% at pH = 3, which was lower than that at pH = 7 (35.2%) (Fig. 24c). The PSM of porous materials often uses toxic reagents or metal catalysts under harsh conditions, risking framework instability, metal contamination, and environmental hazards. Recently, Xu *et al.* have reported an eco-friendly route for PSM of COFs through an enzymatic reaction.[236] Through horseradish peroxidase (HRP)-catalysed click reactions, 2-hydroxyethylthio (–S–EtOH) and ethylthio (–S–Et) groups were covalently introduced into the COF pores under mild aqueous conditions (Fig. 25a). The modified COFs (ACOF–S–EtOH and ACOF–S–Et) retained their crystallinity relative to the pristine COF, as confirmed by PXRD (Fig. 25b) and HRTEM (Fig. 25c). After the introduction of the functional group, the H_2O_2 production was escalated up to 27.9 times, reaching a maximum production rate of 5440 μmol g^{-1} h^{-1} with COF–S–EtOH from H_2O and O_2 (Fig. 25d). Interestingly, the thermally modified sample showed a lower H_2O_2 production rate than the enzymatically modified route, confirming the advantage of the enzymatic PSM method. Furthermore, a continuous-flow photocatalytic reactor packed with ACOF–S–EtOH (Fig. 3d, S24) sustained a steady H_2O_2 concentration of 0.56 mM over 58 h, achieving a cumulative output of 2.5 L (Fig. 25e). The enhanced polarity after PSM has been verified through temperature-dependent photoluminescence (PL) studies. The altered PL emission of COFs was attributed to aggregation effects and enhanced charge polarisation induced by functionalization. Furthermore, the exciton binding energies (E_b) derived from Arrhenius fitting were observed to be 68.4 meV (ACOF), 58.6 meV (ACOF–S–Et), and 34.8 meV (ACOF–S–EtOH) (Fig. 25f). The significantly lower E_b of ACOF–S–EtOH indicates more efficient electron–hole separation, explaining its superior photocatalytic performance. Mechanistic investigation highlights the formation of H_2O_2 *via* both ORR and WOR pathways. *In situ* DRIFTS further verified the $^*OOH$ intermediate by the intensified peak at 1176 cm^{-1} (Fig. 25g). The growing band at 892 cm^{-1} indicated O_2 adsorption on ACOF–S–EtOH, while

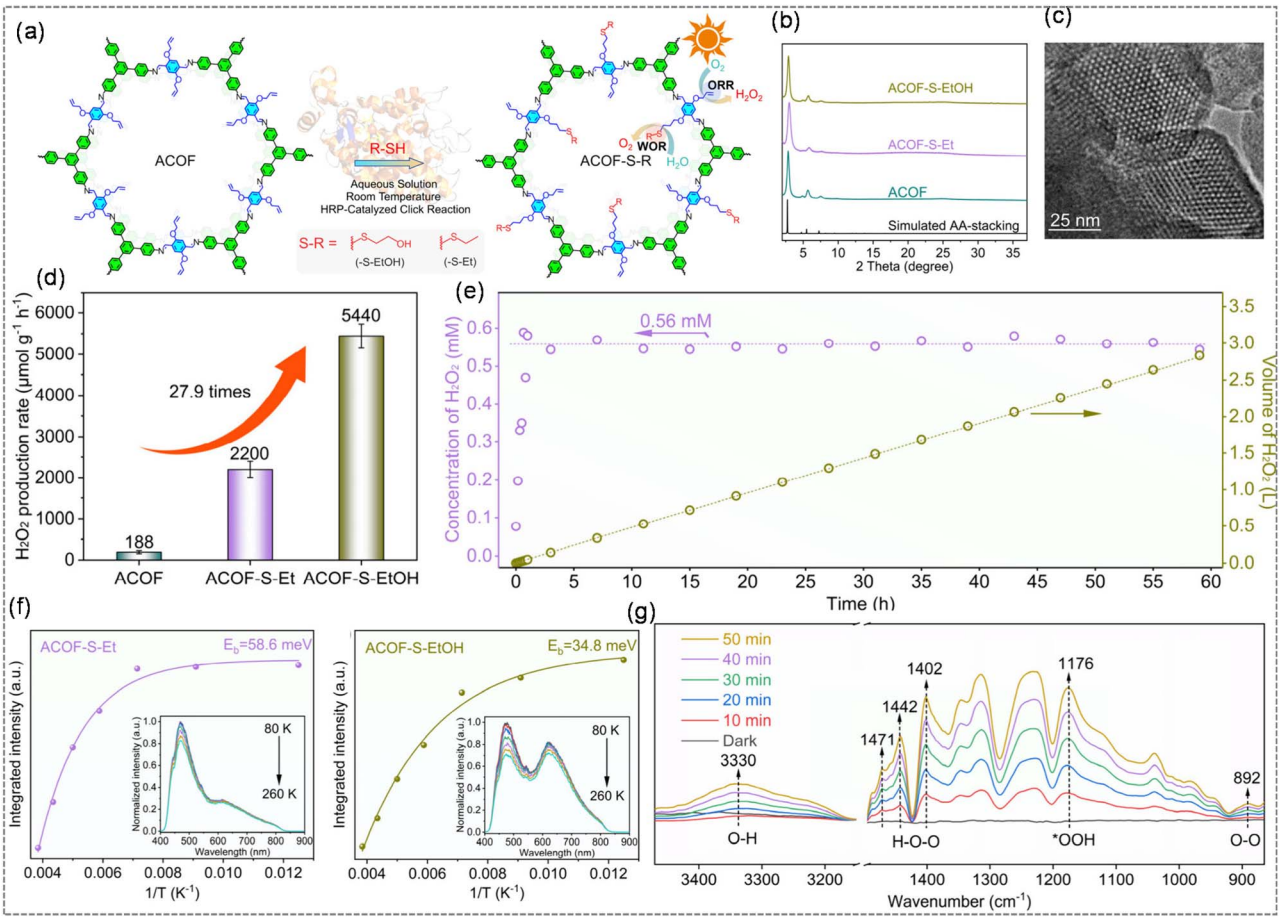

Fig. 25 (a) Schematic route for PSM of the ACOF through an enzymatic click reaction. (b) PXRD of pristine & modified ACOFs. (c) HRTEM image of ACOF–S–EtOH. (d) Comparative H_2O_2 production efficiency of pristine & modified ACOFs. (e) Long-term photocatalytic H_2O_2 production through continuous flow catalysis. (f) Integrated PL emission intensity as a function of temperature for ACOF–S–Et and ACOFS–EtOH. (g) *In situ* DRIFTS spectra of ACOF–S–EtOH during photocatalytic H_2O_2 production (Reprinted with permission from ref. 236. Copyright 2025, American Chemical Society.)

Table 8 Summary of representative AFPM-based composites for photocatalytic H_2O_2 production

Sl. no.	Catalyst	Reaction conditions	Dosage (mg) & volume (mL)	H_2O_2 yield (μmol g^{-1} h^{-1})	AQY	SCC	Ref.
1	Au@COF	H_2O : BA (4 : 1) and O_2	5 mg & 50 mL	18 933.58	—	—	235
2	MPa-COFs/CQDs-2	H_2O and O_2	20 mg & 100 mL	540	13.27% @ 400 nm	0.8%	230
3	CdS/TpMA	H_2O and O_2	20 mg & 50 mL	511.54 μmol L^{-1} h^{-1}	—	—	232
4	$ZnIn_2S_4$/TpPa-1	H_2O, EtOH and O_2	20 mg & 40 mL	516 μmol L^{-1}	—	—	233
5	WO_3/Tp-TAPB	H_2O and O_2	5 mg & 10 mL	1488.4	1.22% @ 420 nm	—	234
6	$ZnIn_2S_4$/UiO-66-NH_2	H_2O and air	20 mg & 40 mL	799	—	—	237
7	Al-TCPP (10-X)-TBAPyX	H_2O and O_2	5 mg & 5 mL	127	—	—	238
8	Al-MIL-101-NH_2	H_2O and O_2	5 mg & 5 mL	295	—	—	239
9	Pd_1/A-aUiO	H_2O and O_2	Membrane based	1.74 mmol g_{cat}^{-1} h^{-1}	—	—	240
10	COF@H_3PO_4	H_2O and O_2	10 mg & 20 mL	5214	—	0.69%	241
11	Fe SAS-TpPP-COF	H_2O : BA (9 : 1) and O_2	5 mg & 50 mL	4130	6.4% @ 420 nm	0.20%	242

increased signals at 3330 cm^{-1} (O–H stretching) and at 1402, 1442, and 1471 cm^{-1} (H–O–O bending) confirmed the formation and accumulation of H_2O_2. The major achievements of the AFPM-based composites for H_2O_2 production have been highlighted in Table 8.

Similar to COFs, the ubiquitous opportunity of MOF materials for PSM has been widely explored, especially for electrocatalytic applications.[243–246] Due to their distinctive advantages, MOF-based materials have become promising electrocatalysts for the $2e^-$ ORR in H_2O_2 generation.[247,248] Accordingly, MOF composites, pure MOFs, and bimetallic MOFs have been

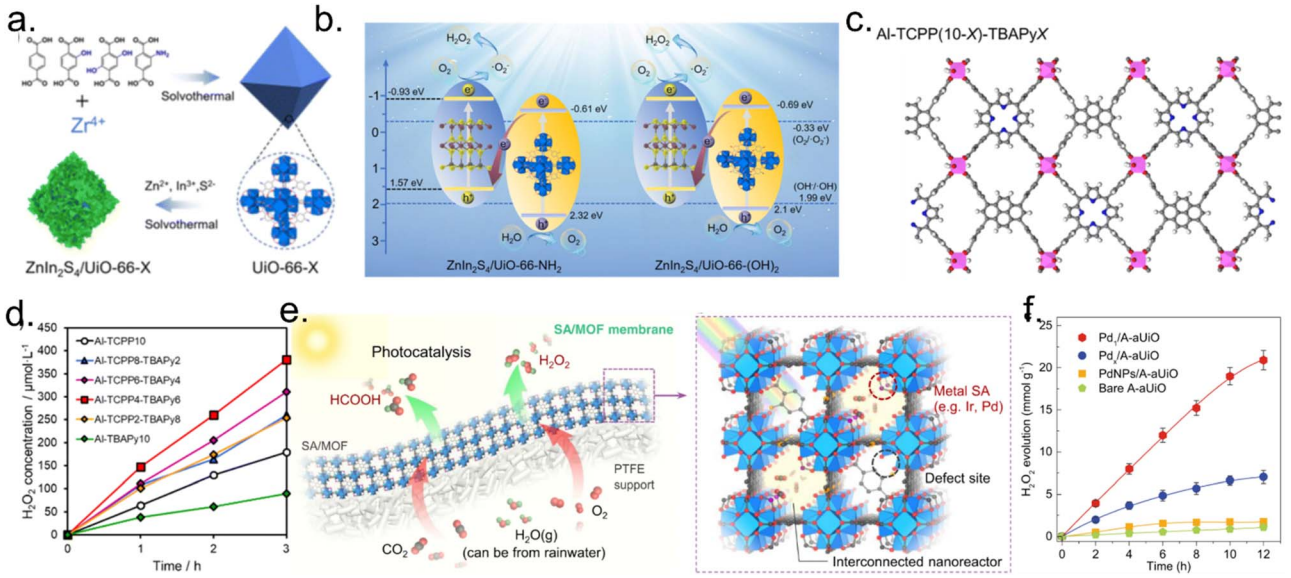

Fig. 26 (a) Preparation diagram of $ZnIn_2S_4$/UiO-66-X hybrids, (b) the proposed mechanism for photocatalytic H_2O_2 evolution using Z-UN and Z-U(OH)$_2$. (Reprinted with permission from ref. 237. Copyright 2023, Royal Society of Chemistry.) (c) schematic of Al-TCPP(10-X)-TBAPyX, (d) comparison of photocatalytic H_2O_2 production over Al-TCPP(10-X)-TBAPyX samples, and (e) schematic showing that humidified gases (*e.g.*, CO_2 and O_2) can be fed through the gas-permeable MOF/PTFE membranes and photocatalytically reduced to value-added chemicals (*e.g.*, HCOOH and H_2O_2) under visible light irradiation and ambient conditions and with controllable defect-engineering, specific metal SAs (*e.g.*, Ir and Pd) can be precisely anchored on the edges of the $Zr_6O_4(OH)_4(-CO_2)_{12-x}$ octahedral to act as programable catalytic centers for catalyzing different reactions, such as photocatalytic CO_2-to-HCOOH and O_2-to-H_2O_2 conversion. The open and interconnected MOF pores serve as the nanoreactors facilitating the diffusion and conversion of gas reactants. (Reprinted with permission from ref. 238. Copyright 2023, Royal Society of Chemistry.) (f) Time course of H_2O_2 generation on pristine A-aUiO and PdNPs-, Pd$_x$-, and Pd$_1$-decorated A-aUiO catalysts. (Reprinted with permission from ref. 240. Copyright 2023, Springer Nature.)

demonstrated to be promising materials for photocatalytic H_2O_2 generation. Yao and the team recently synthesised several $ZnIn_2S_4$/UiO-66-X (X = H, OH, (OH)$_2$, and NH_2) and discovered that amino or hydroxyl functionalisation may activate the effective photocatalytic production of H_2O_2 under visible light (Fig. 26a).[237] The H_2O_2 yields for $ZnIn_2S_4$/UiO-66-NH_2, $ZnIn_2S_4$/UiO-66-(OH)$_2$, and $ZnIn_2S_4$/UiO-66-OH are 799, 733, and 165 μmol L^{-1}, respectively, whereas the yield for $ZnIn_2S_4$/UiO-66 is just 84 μmol L^{-1} (without a sacrificial agent, in ambient air, and indirect ORR). The enhanced visible-light absorption and Z-scheme heterojunctions of $ZnIn_2S_4$/UiO-66-NH_2 and $ZnIn_2S_4$/UiO-66-(OH)$_2$ led to their significant H_2O_2 generation (Fig. 26b). The Yamashita research group synthesised an Al-MOF utilising mixed ligands of 1,3,6,8-tetrakis(*p*-benzoic acid) pyrene and tetrakis(4-carboxyphenyl) porphyrin for photocatalytic H_2O_2 generation under visible light (Fig. 26c).[238] Al-MOFs have the capacity to inhibit the breakdown of H_2O_2 and have introduced a novel pathway for the generation of H_2O_2 utilising $^1O_2$ as the intermediate.[239] The production of H_2O_2 *via* both the ORR ($^1O_2 + 2H^+ + 2e^- \rightarrow H_2O_2$) and WOR ($^1O_2 + 2H_2O \rightarrow 2H_2O_2$) utilizing $^1O_2$ was deduced. Wang *et al.* deposited Pd single atoms over faulty UiO-66-NH_2 and then fabricated gas-permeable Pd/UiO-66-NH_2 membranes for photocatalytic H_2O_2 production from humid O_2 at gas–solid interfaces.[240] The positively charged Pd single atoms can enhance H_2O_2 generation and simultaneously impede H_2O_2 breakdown, as shown in the prior work.[249] The defect sites facilitated light absorption and interaction with metal single atoms, whereas the UiO-66-NH_2 molecular structure functioned as several linked non-reactors. A notable H_2O_2 production rate of 10.4 mmol g^{-1} h^{-1} was achieved using Pd/UiO-66-NH_2 membranes in a gas–membrane–gas configuration, which is 4.9 times more than that produced with Pd/UiO-66-NH_2 particles in a particle-in-solution setup (utilising visible light, isopropanol as a sacrificial agent, and pure O_2 for the ORR) (Fig. 26f).

Conclusion and future perspectives

In recent years, H_2O_2 has received gradually increasing attention, and it is recognised not only as an efficient oxidant in various fields but also as a prospective energy carrier. The photosynthesis of H_2O_2 over AFPM has attracted growing interest, and efforts are being made to regulate the efficiency of AFPM-based photocatalysts to achieve remarkable H_2O_2 production performance. In this review, we have elaborated on the recent strategies applied to increase the efficiency of various AFPM-based photocatalysts for H_2O_2 photosynthesis. More importantly, the modification strategies reported thus far for achieving improved photocatalytic H_2O_2 production performance over AFPM-based photocatalysts have been comprehensively summarised and discussed. Most of the reported articles have tried to understand the effect of linkage modification, heteroatom doping, topology and structural modification, functional group incorporation, post-synthetic

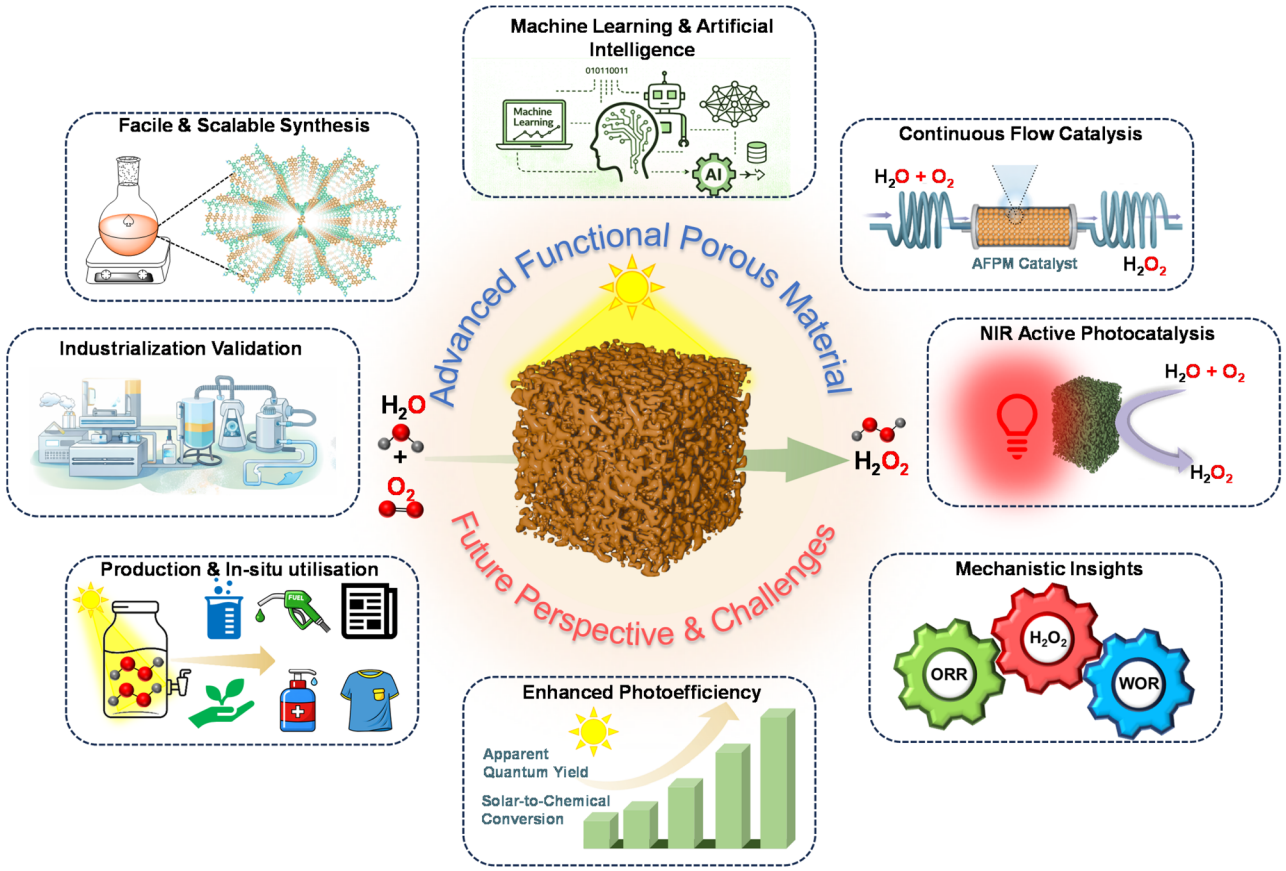

Fig. 27 Representative diagram highlighting the future perspectives and challenges in AFPM-based photocatalytic H_2O_2 production.

modification, *etc.*, towards improving the D–A property, enhanced charge separation, and effect on the band gap. The active site for H_2O_2 production has been meticulously studied in metal and metal-free AFPM using experimental and computational techniques. This has further enabled the better design of materials for practical implementation. Similarly, the range of applications has expanded, offering possibilities for photocatalytic H_2O_2 production that is not only efficient but also selective and recyclable for multiple cycles. The capability to adjust functionality in metal-free AFPMs has further provided an opportunity to tune band positions for efficient H_2O_2 production. The synthesis of composites using AFPMs has also showcased its photocatalytic efficiency by creating heterojunctions appropriate for photocatalytic H_2O_2 production. Though tremendous research is going on to improve the photocatalytic production of H_2O_2, there are still several challenges that need to be addressed to translate the potential of materials from laboratory to practical, real-world applications (Fig. 27). This involves tackling the following aspects:

(i) AFPM diversification with hierarchical porosity: among the various types of metal-free AFPM materials, there are numerous reports on COFs, while other AFPM materials have received less attention. Although COFs offer an ordered structure and a larger surface area than other organic frameworks like POPs and CTFs, more detailed research on other AFPMs to enhance photocatalytic activity would be beneficial. The photocatalytic performance is strongly dependent on the crystallinity of COFs; however, crystallinity can deteriorate over time during long-term catalytic operation. Therefore, the development of porous materials that can sustain high photocatalytic performance independent of long-range crystalline order, while effectively leveraging porous architectures, is highly desirable. In this regard, the development of porous material-based aerogels for H_2O_2 photosynthesis represents a promising breakthrough, as such systems can exploit hierarchical macro–mesoporosity to enhance mass transport and catalytic efficiency.

(ii) ORR-WOR engineering: the rational design of porous materials for photocatalytic H_2O_2 production must be tailored to the targeted reaction pathway: the ORR or WOR, as each imposes distinct electronic and structural requirements. After photoinduced electron–hole separation in a photocatalyst, the ORR proceeds *via* the excited electrons, while the WOR is driven by the photogenerated holes. The electron-deficient moieties like triazine, benzothiadiazole, and cyano groups function as ORR-active centres for the efficient $2e^-$ ORR, while electron-rich sulfur-containing units such as pyrene, thiophene, and triarylamines proved to be effective WOR-active sites for the $2e^-$ WOR. COFs, with tunable π-conjugation and ordered porosity, are well suited for ORR-driven H_2O_2 generation through D–A engineering, band-edge alignment toward the O_2/H_2O_2 potential, and pore environments that enhance O_2 diffusion and

H_2O_2 desorption while suppressing the $4e^-$ pathway. POPs, owing to their high chemical and oxidative stability, are particularly promising for WOR-driven H_2O_2 production, where functionalisable backbones and hydrophilic pores facilitate water adsorption, intermediate stabilisation, and proton-coupled electron transfer. MOFs offer site-isolated metal nodes (Zn, Zr, or single-site Fe/Co under controlled coordination) and modular coordination environments, enabling selective ORR *via* weak O–O activation or WOR through stable water-oxidation centres, provided oxidative robustness is ensured. MOPs and HOFs with an appropriate D–A site have shown H_2O_2 production through the simultaneous ORR–WOR pathway.

(iii) NIR photocatalysis: the most practical and sustainable route for H_2O_2 synthesis relies on solar energy; however, nearly 53% of the solar spectrum lies in the near-infrared (NIR, $\lambda > 760$ nm) region. In contrast, photocatalytic H_2O_2 production over AFPM-based catalysts remains largely restricted to visible-light excitation ($\lambda < 760$ nm). To date, only a handful of studies have focused on the rational design of NIR-responsive catalysts, highlighting a significant research gap. Therefore, greater emphasis should be placed on the development of NIR-active porous photocatalysts to more effectively utilise the full solar spectrum. Furthermore, as the AQY and SCC are key metrics for evaluating photocatalytic performance, photoefficiency improvement should not be overlooked. The highest AQYs of 22.78%, 14.9%, and 16.8% have been reported for COFs, MOFs, and CTFs, respectively, at ~420 nm. Similarly, SCC efficiencies of 1.41%, 0.91%, and 1.2% were reported for COFs, MOFs, and CTFs under artificial sunlight simulation. While SCC values above 1.0% have been reported under laboratory conditions, these are typically achieved through extensive parameter optimisation rather than intrinsic catalyst efficiency. Under natural sunlight, the SCC efficiencies of photocatalysts for H_2O_2-production remain well below the ~0.10% efficiency of natural photosynthesis, posing a major barrier to industrial application.

(iv) Facile and scalable synthetic route: from the viewpoint of practical photocatalytic H_2O_2 production, the scalability and facile synthesis of AFPM-based materials are of paramount importance. Although these materials have demonstrated impressive activity and selectivity toward the $2e^-$ ORR, most reported synthetic strategies remain complex, low-yielding, and difficult to translate to large-scale manufacturing. Future efforts should therefore focus on developing cost-effective, environmentally benign, and scalable fabrication routes, while maintaining precise control over active sites and electronic structures. Furthermore, achieving batch-to-batch uniformity and reproducibility remains a key challenge for the commercialisation of porous materials. Therefore, the development of well-controlled and scalable synthetic routes, such as melt polymerisation and continuous-flow COF synthesis, to enable reliable bulk production is necessary. Addressing these challenges will be essential for advancing AFPM-based photocatalysts from laboratory studies toward industrially viable H_2O_2 production technologies.

(v) Artificial intelligence (AI) and machine learning (ML) guided photocatalytic screening: AI and ML provide transformative high-throughput strategies for the discovery of efficient COF-based photocatalysts for H_2O_2 production. By learning structure–property–performance relationships from existing experimental and computational datasets, ML models should be employed to rapidly predict key descriptors such as band-edge alignment, charge-carrier separation efficiency, pore polarity, and adsorption energies of ORR intermediates (*OOH, H_2O_2, etc.). These data-driven predictions enable virtual screening of vast COF chemical spaces, significantly reducing reliance on trial-and-error synthesis. Coupled with automated synthesis and high-throughput photocatalytic evaluation, AI-guided frameworks can iteratively optimise COF architectures to selectively promote the $2e^-$ ORR pathway while suppressing competing reactions. Such AI-assisted discovery platforms are expected to accelerate the development of high-performance, solar-driven COF photocatalysts with improved AQY and SCC values. Furthermore, the integration of AI/ML automation and robotics into COF synthesis can also offer a powerful approach for rapidly screening reaction parameters and discovering new chemistries, thereby accelerating the transition of porous material from laboratory-scale materials to industrially viable platforms.

(vi) Decentralised H_2O_2 production and industrial validation: although the anthraquinone process remains the benchmark for large-scale H_2O_2 production, porous material-based photocatalytic systems are not yet positioned to compete directly at the industrial scale. While the anthraquinone process remains the established benchmark for large-scale, centralised H_2O_2 production. Rather than serving as direct replacements, AFPM-based systems are better suited for decentralised and on-demand H_2O_2 generation at low-to-moderate concentrations (10–100 mM), where transportation, storage, and safety considerations become critical. Operating under mild conditions and enabling integration with flow reactors and *in situ* utilisation, these systems are well-positioned to complement existing technologies in applications such as water treatment, disinfection, and selective oxidation.

(vii) Extraction and utilisation of *in situ* produced H_2O_2: the extraction and utilisation of generated H_2O_2 remain critical challenges for its practical deployment. While *ex situ* extraction and purification are often necessary for off-site applications, they introduce additional energy and separation costs and can accelerate H_2O_2 decomposition during handling. In contrast, *in situ* utilisation strategies, where H_2O_2 is consumed immediately after generation, offer a more efficient and sustainable alternative by minimising accumulation, suppressing decomposition, and reducing safety concerns. Oxidation reactions, antimicrobial processes, pollutant degradation, and heavy metal capture and sequestration offer practical strategies to consume H_2O_2 immediately, suppress degradation pathways, and extend the catalyst lifetime. Future advances will depend on reactor designs and porous catalyst architectures that simultaneously facilitate controlled H_2O_2 release, selective mass transport, and seamless integration with end-use reactions, thereby bridging the gap between laboratory-scale synthesis and real-world applications.

(viii) Continuous flow catalysis: flow catalysis presents a compelling strategy for advancing porous materials toward stable and scalable H_2O_2 synthesis. Continuous-flow reactors enable precise control over mass transport, reactant residence time, and photon utilisation, which are critical for regulating the $2e^-$ ORR or WOR pathways while minimising H_2O_2 over-reduction and catalytic decomposition. Importantly, flow operation alleviates local H_2O_2 accumulation and concentration gradients that often accelerate framework degradation in batch systems, thereby enhancing the structural stability and operational durability of porous catalysts. When coupled with robust frameworks and optimised pore environments, flow catalysis offers a practical platform for sustained H_2O_2 production, bridging the gap between laboratory-scale demonstrations and long-term, industrially relevant operation. By enabling decentralised, on-site generation, flow catalysis eliminates challenges associated with H_2O_2 storage, decomposition, and transport. For real-world implementation, photocatalytic systems should therefore be designed to deliver H_2O_2 on demand at concentrations in the range of 10–100 mM.

(ix) Suppression of H_2O_2 decomposition: direct exposure of the photocatalyst to the generated H_2O_2 frequently promotes its undesired decomposition, thereby restricting achievable yields. To address this challenge, several catalyst-product separation strategies have been explored. Among them, biphasic reaction systems (*e.g.*, water–benzyl alcohol) are widely employed, wherein the hydrophobic character of certain MOFs, combined with density-driven phase separation, enables the preferential transfer of H_2O_2 into the aqueous phase. Although sacrificial agents effectively suppress charge recombination, their use complicates H_2O_2 separation and purification. A more sustainable strategy is to employ sacrificial agents that selectively consume photogenerated holes while simultaneously enabling the synthesis of value-added chemicals.

(x) Structure–activity relationships and mechanistic insights: clarifying reaction mechanisms and structure–activity relationships remains a central challenge for AFPM-based photocatalysts in H_2O_2 photosynthesis. Although AFPM offers rich structural diversity through versatile bonding motifs, abundant building blocks, and tunable functional groups, their structure–performance correlations in H_2O_2 generation are still poorly understood due to complex architectures and reaction environments. Substantial efforts are therefore required to elucidate the roles of electronic structure, pore hydrophilicity/hydrophobicity, and nano-confinement effects in governing photocatalytic activity and selectivity. Beyond rational material design, the integration of advanced *in situ* characterisation techniques with density functional theory (DFT) calculations is essential to unravel charge-transfer pathways and free-radical mechanisms involved in AFPM-driven H_2O_2 synthesis, which will be critical for accelerating progress in this field.

Author contributions

Sagarmani Rasaily: conceptualisation, literature survey, writing original draft, figure preparation, and funding acquisition. Gourab K. Dam: literature survey, writing draft and figure preparation. Sujit K. Ghosh: review & editing, supervision, and funding acquisition.

Conflicts of interest

There are no conflicts to declare.

Data availability

No primary research results, software or code have been included and no new data were generated or analysed as part of this review.

Acknowledgements

SMR acknowledges ANRF (formerly SERB) for funding through the National Postdoctoral Fellowship (NPDF) Scheme (project no. PDF/2023/001234). GKD thanks CSIR for the fellowship. SKG acknowledges DST-SERB (project no. CRG/2022/001090) and CSIR, India (project no. 30523670 (01/3124/23/EMR-II)), for funding.

References

1 J. M. Campos-Martin, G. Blanco-Brieva and J. L. G. Fierro, *Angew. Chem., Int. Ed.*, 2006, **45**, 6962–6984.
2 H. J. H. Fenton, *J. Chem. Soc. Trans.*, 1894, **65**, 899–909.
3 M. A. Voinov, J. O. S. Pagán, E. Morrison, T. I. Smirnova and A. I. Smirnov, *J. Am. Chem. Soc.*, 2011, **133**, 35–41.
4 B. W. Richardson, *Lancet*, 1891, **137**, 707–709.
5 T. H. Oliver and D. V. Murphy, *Lancet*, 1920, **195**, 432–433.
6 J. W. Finney, H. C. Urschel, G. A. Balla, G. J. Race, B. E. Jay, H. P. Pingree, H. L. Dorman and J. T. Mallams, *Ann. N. Y. Acad. Sci.*, 1967, **141**, 231–241.
7 M. Armogida, R. Nisticò and N. B. Mercuri, *Br. J. Pharmacol.*, 2012, **166**, 1211–1224.
8 R. Ciriminna, L. Albanese, F. Meneguzzo and M. Pagliaro, *ChemSusChem*, 2016, **9**, 3374–3381.
9 R. L. Myers, *The 100 Most Important Chemical Compounds: A Reference Guide*, Greenwood Press, 2007.
10 A. B. Trench, C. M. Fernandes, J. P. C. Moura, L. E. B. Lucchetti, T. S. Lima, V. S. Antonin, J. M. de Almeida, P. Autreto, I. Robles, A. J. Motheo, M. R. V. Lanza and M. C. Santos, *Chemosphere*, 2024, **352**, 141456.
11 Y. Tang, W. Wang, J. Ran, C. Peng, Z. Xu and W. Chu, *Energy Environ. Sci.*, 2024, **17**, 6482–6498.
12 Y. Sun, L. Han and P. Strasser, *Chem. Soc. Rev.*, 2020, **49**, 6605.
13 Y. Yamada, M. Yoneda and S. Fukuzumi, *Energy Environ. Sci.*, 2015, **8**, 1698–1701.
14 Hydrogen Peroxide Market – By Function (Disinfectant, Bleaching, Oxidant), By Application (Pulp & Paper, Chemical Synthesis, Wastewater Treatment, Mining, Food & Beverages, Personal Care, Healthcare, Textiles), & Forecast, 2024–2032, 2024.

15 India Hydrogen Peroxide Market Analysis: Industry Market Size, Plant Capacity, Production, Operating Efficiency, Demand & Supply, End-User Industries, Sales Channel, Regional Demand, Company Share, Foreign Trade, Manufacturing, 2024.
16 X. Zhang, X. Zhao, P. Zhu, Z. Adler, Z. Y. Wu, Y. Liu and H. Wang, *Nat. Commun.*, 2022, **13**, 2880.
17 S. C. Perry, D. Pangotra, L. Vieira, L. I. Csepei, V. Sieber, L. Wang, C. Ponce de León and F. C. Walsh, *Nat. Rev.*, 2019, **3**, 442–458.
18 X. Liang, Z. Mi, Y. Wang, L. Wang, X. Zhang and T. Liu, *Chem. Eng. Technol.*, 2004, **27**, 176–180.
19 C. Xia, Y. Xia, P. Zhu, L. Fan and H. Wang, *Science*, 2019, **366**, 226–231.
20 R. Ernstorfer, M. Harb, C. T. Hebeisen, G. Sciaini, T. Dartigalongue and R. J. D. Miller, *Science*, 2009, **323**, 1033–1037.
21 J. H. Lunsford, *J. Catal.*, 2003, **216**, 455–460.
22 *Oxygen-enhanced combustion*, ed. C. E. Baukal Jr, CRC Press, 2nd edn, 2013.
23 L. Wang, J. Zhang, Y. Zhang, H. Yu, Y. Qu and J. Yu, *Small*, 2022, **18**, 2104561.
24 H. Tada, M. Teranishi and S. I. Naya, *J. Phys. Chem. C*, 2023, **127**, 5199–5209.
25 H. Huang, M. Sun, M. Li, L. Tang and S. Zhang, *Green Energy Resour.*, 2023, **1**, 10003125.
26 W. Wang, Q. Song, Q. Luo, L. Li, X. Huo, S. Chen, J. Li, Y. Li, S. Shi, Y. Yuan, X. Du, K. Zhang and N. Wang, *Nat. Commun.*, 2023, **14**, 2493.
27 Z. Li, Z. Yu, C. Guan, K. Xu and Q. Xiang, *J. Materiomics*, 2024, **11**, 100982.
28 Z. Jiang, C. Li, F. Qi, Z. Wang, Y. Liu, F. Li, H. Wang, Z. Bian, M. Zhu, J. Kumirska and E. M. Siedlecka, *Appl. Mater. Interfaces*, 2025, **17**, 42–66.
29 H. He, S. Liu, Y. Liu, L. Zhou, H. Wen, R. Shen, H. Zhang, X. Guo, J. Jiang and B. Li, *Green Chem.*, 2023, **25**, 9501–9542.
30 Y. Yang, C. Wang, Y. Li, K. Liu, H. Ju, J. Wang and R. Tao, *J. Mater. Sci. Technol.*, 2024, **200**, 185–214.
31 Y. Shi, Z. Zhao, D. Yang, J. Tan, X. Xin, Y. Liu and Z. Jiang, *Chem. Soc. Rev.*, 2023, **52**, 6938–6956.
32 Q. Wang and K. Domen, *Chem. Rev.*, 2020, **120**, 919–985.
33 X. Tao, Y. Zhao, S. Wang, C. Li and R. Li, *Chem. Soc. Rev.*, 2022, **51**, 3561.
34 R. Marschall, *Eur. J. Inorg. Chem.*, 2021, **2021**, 2435–2441.
35 Y. N. Gong, X. Guan and H. L. Jiang, *Coord. Chem. Rev.*, 2023, **475**, 214889.
36 Y. Hao, Y. L. Lu, Z. Jiao and C. Y. Su, *Angew. Chem., Int. Ed.*, 2024, **63**, e202317808.
37 B. Gurung, S. Pradhan, D. Sharma, D. Bhujel, S. Basel, S. Chettri, S. Rasaily, A. Pariyar and S. Tamang, *Catal. Sci. Technol.*, 2022, **12**, 5891–5898.
38 Ž. Kovačič, B. Likozar and M. Huš, *ACS Catal.*, 2020, **10**, 14984–15007.
39 W. Gao, H. Li, J. Hu, Y. Yang, Y. Xiong, J. Ye, Z. Zou and Y. Zhou, *Chem. Sci.*, 2024, **15**, 14081–14103.
40 S. Wu and X. Quan, *ACS ES&T Eng.*, 2022, **2**, 1068–1079.
41 A. Fujishima and K. Honda, *Nature*, 1972, **238**, 37–38.
42 G. Zhang, Z. Guan, J. Yang, Q. Li, Y. Zhou and Z. Zou, *Sol. RRL*, 2022, **6**, 2200587.
43 V. Soni, M. Malhotra, P. Singh, A. A. P. Khan, W. A. Bawazir, V. H. Nguyen, T. Ahamad, Q. Van Le, P. Raizada and K. A. Alzahrani, *J. Environ. Chem. Eng.*, 2025, **13**, 115151.
44 W. Ji, Z. Xu, S. Zhang, Y. Li, Z. Bao, Z. Zhao, L. Xie, X. Zhong, Z. Wei and J. Wang, *Catal. Sci. Technol.*, 2022, **12**, 2865–2871.
45 M. Gryszel, R. Rybakiewicz and E. D. Głowacki, *Adv. Sustainable Syst.*, 2019, **3**, 1900027.
46 Y. Zheng, J. Liu, J. Liang, M. Jaroniec and S. Z. Qiao, *Energy Environ. Sci.*, 2012, **5**, 6717.
47 S. Cao, J. Low, J. Yu and M. Jaroniec, *Adv. Mater.*, 2015, **27**, 2150–2176.
48 J. Fu, J. Yu, C. Jiang and B. Cheng, *Adv. Energy Mater.*, 2018, **8**, 1701503.
49 J. Zhu, P. Xiao, H. Li and S. A. C. Carabineiro, *ACS Appl. Mater. Interfaces*, 2014, **6**, 16449–16465.
50 S. Bordiga, C. Lamberti, G. Ricchiardi, L. Regli, F. Bonino, A. Damin, K. P. Lillerud, M. Bjorgen and A. Zecchina, *Chem. Commun.*, 2004, 2300–2301.
51 M. Alvaro, E. Carbonell, B. Ferrer, F. X. Llabrés I Xamena and H. Garcia, *Chem.—Eur. J.*, 2007, **13**, 5106–5112.
52 S. Navalón, A. Dhakshinamoorthy, M. Álvaro, B. Ferrer and H. García, *Chem. Rev.*, 2023, **123**, 445–490.
53 J. D. Xiao and H. L. Jiang, *Acc. Chem. Res.*, 2019, **52**, 356–366.
54 R. Chen, G. Liu, B. Xia, T. Liu, Y. Xia, S. Liu, A. Talebian-Kiakalaieh and J. Ran, *Chem. Commun.*, 2024, **60**, 10989.
55 M. G. Schwab, M. Hamburger, X. Feng, J. Shu, H. W. Spiess, X. Wang, M. Antonietti and K. Müllen, *Chem. Commun.*, 2010, **46**, 8932–8934.
56 S. Liu, M. Wang, Y. He, Q. Cheng, T. Qian and C. Yan, *Coord. Chem. Rev.*, 2023, **475**, 214882.
57 H. Ran, Q. Xu, Y. Yang, H. Li, J. Fan, G. Liu, L. Zhang, J. Zou, H. Jin and S. Wang, *ACS Catal.*, 2024, **14**, 11675–11704.
58 M. Debruyne, P. Van Der Voort, V. Van Speybroeck and C. V. Stevens, *Chem.–Eur. J.*, 2024, **30**, e202400311.
59 T. X. Wang, H. P. Liang, D. A. Anito, X. Ding and B. H. Han, *J. Mater. Chem. A*, 2020, **8**, 7003.
60 T. Gao, D. Zhao, S. Yuan, M. Zheng, X. Pu, L. Tang and Z. Lei, *Carbon Energy*, 2024, **6**, e596.
61 D. Tsukamoto, A. Shiro, Y. Shiraishi, Y. Sugano, S. Ichikawa, S. Tanaka and T. Hirai, *ACS Catal.*, 2012, **2**, 599–603.
62 H. L. Tan, C. H. T. Chai, J. Z. X. Heng, Q. V. Thi, X. Wu, Y. H. Ng and E. Ye, *Adv. Sci.*, 2025, **12**, 2407801.
63 Y. Shiraishi, S. Kanazawa, Y. Sugano, D. Tsukamoto, H. Sakamoto, S. Ichikawa and T. Hirai, *ACS Catal.*, 2014, **4**, 774–780.
64 X. Xiao, H. Wang, X. Wang, C. Liu, Y. Han, S. Zhai and H. Du, *Carbon Energy*, 2025, **7**, e666.
65 D. Tan, R. Zhuang, R. Chen, M. Ban, W. Feng, F. Xu, X. Chen and Q. Wang, *Adv. Funct. Mater.*, 2024, **34**, 2311655.
66 J. Qiu, D. Dai and J. Yao, *Coord. Chem. Rev.*, 2024, **501**, 215597.
67 W. Wang, X. Wang, M. Gao, Z. Li and W. Zhou, *Coord. Chem. Rev.*, 2024, **506**, 215694.

68 D. Tan and X. Fan, *Polymers*, 2024, **16**, 659.
69 K. H. Xie, G. B. Wang, F. Zhao, M. C. Wang, H. Y. Zhang, H. R. Ma, Z. Z. Chen, L. Jiang, Y. Geng and Y. Bin Dong, *Inorg. Chem. Front.*, 2024, **11**, 1322.
70 A. P. Cote, A. I. Benin, N. W. Ockwig, M. O'Keeffe, A. J. Matzger and O. M. Yaghi, *Science*, 2005, **310**, 1164–1166.
71 N. L. Campbell, R. Clowes, L. K. Ritchie and A. I. Cooper, *Chem. Mater.*, 2009, **21**, 204–206.
72 X. Zhao, P. Pachfule and A. Thomas, *Chem. Soc. Rev.*, 2021, **50**, 6871–6913.
73 Y. N. Gong, X. Guan and H. L. Jiang, *Coord. Chem. Rev.*, 2023, **475**, 214889.
74 L. Stegbauer, K. Schwinghammer and B. V. Lotsch, *Chem. Sci.*, 2014, **5**, 2789–2793.
75 Y. Yusran, H. Li, X. Guan, Q. Fang and S. Qiu, *J. Energy Chem.*, 2020, **2**, 100035.
76 Z. Alsudairy, N. Brown, A. Campbell, A. Ambus, B. Brown, K. Smith-Petty and X. Li, *Mater. Chem. Front.*, 2023, **7**, 3298–3331.
77 H. Li, A. Dilipkumar, S. Abubakar and D. Zhao, *Chem. Soc. Rev.*, 2023, **52**, 6294–6329.
78 Z. Wang, S. Zhang, Y. Chen, Z. Zhang and S. Ma, *Chem. Soc. Rev.*, 2020, **49**, 708–735.
79 X. Zhao, P. Pachfule and A. Thomas, *Chem. Soc. Rev.*, 2021, **50**, 6871–6913.
80 D. G. Wang, T. Qiu, W. Guo, Z. Liang, H. Tabassum, D. Xia and R. Zou, *Energy Environ. Sci.*, 2021, **14**, 688–728.
81 J. Guo, S. Kong, Y. Lian and M. Zhao, *Chem. Commun.*, 2024, **60**, 918–934.
82 X. Liu, D. Huang, C. Lai, G. Zeng, L. Qin, H. Wang, H. Yi, B. Li, S. Liu, M. Zhang, R. Deng, Y. Fu, L. Li, W. Xue and S. Chen, *Chem. Soc. Rev.*, 2019, **48**, 5266–5302.
83 R. Xue, Y. S. Liu, S. L. Huang and G. Y. Yang, *ACS Sens.*, 2023, **8**, 2124–2148.
84 J. Wang and S. Zhuang, *Coord. Chem. Rev.*, 2019, **400**, 213046.
85 C. I. Yeo, Y. S. Tan, H. T. A. Awan, A. Hanan, W. P. Wong, R. Walvekar, B. H. Goh and M. Khalid, *Coord. Chem. Rev.*, 2024, **521**, 216167.
86 S. Wan, J. Guo, J. Kim, H. Ihee and D. Jiang, *Angew. Chem., Int. Ed.*, 2008, **47**, 8826–8830.
87 I. H. Chowdhury, S. Gupta and V. G. Rao, *ChemCatChem*, 2023, **15**, e202300243.
88 H. Wang, H. Wang, Z. Wang, L. Tang, G. Zeng, P. Xu, M. Chen, T. Xiong, C. Zhou, X. Li, D. Huang, Y. Zhu, Z. Wang and J. Tang, *Chem. Soc. Rev.*, 2020, **49**, 4135–4165.
89 C. Krishnaraj, H. Sekhar Jena, L. Bourda, A. Laemont, P. Pachfule, J. Roeser, C. V. Chandran, S. Borgmans, S. M. J. Rogge, K. Leus, C. V. Stevens, J. A. Martens, V. Van Speybroeck, E. Breynaert, A. Thomas and P. Van Der Voort, *J. Am. Chem. Soc.*, 2020, **142**, 20107–20116.
90 G. Zhang, M. Zhao, L. Su, H. Yu, C. Wang, D. Sun and Y. Ding, *ACS Appl. Mater. Interfaces*, 2023, **15**, 20310–20316.
91 H. Liu, S. Zhu, Y. Zhi, H. Yue and X. Liu, *Chem. Sci.*, 2025, **16**, 12768.
92 J. Sun, H. Sekhar Jena, C. Krishnaraj, K. Singh Rawat, S. Abednatanzi, J. Chakraborty, A. Laemont, W. Liu, H. Chen, Y. Y. Liu, K. Leus, H. Vrielinck, V. Van Speybroeck and P. Van Der Voort, *Angew. Chem., Int. Ed.*, 2023, **62**, e202216719.
93 R. Liu, Y. Chen, H. Yu, M. Položij, Y. Guo, T. C. Sum, T. Heine and D. Jiang, *Nat. Catal.*, 2024, **7**, 195–206.
94 Y. Chen, R. Liu, Y. Guo, G. Wu, T. C. Sum, S. W. Yang and D. Jiang, *Nat. Synth.*, 2024, **3**, 998–1010.
95 D. Li, C. Li, L. Zhang, H. Li, L. Zhu, D. Yang, Q. Fang, S. Qiu and X. Yao, *J. Am. Chem. Soc.*, 2020, **142**, 8104–8108.
96 C. Qin, X. Wu, L. Tang, X. Chen, M. Li, Y. Mou, B. Su, S. Wang, C. Feng, J. Liu, X. Yuan, Y. Zhao and H. Wang, *Nat. Commun.*, 2023, **14**, 5238.
97 X. Wang, H. Li, S. Zhou, J. Ning, H. Wei, X. Li, S. Wang, L. Hao and D. Cao, *Adv. Funct. Mater.*, 2025, **35**, 2424035.
98 J. Y. Yue, L. P. Song, Y. F. Fan, Z. X. Pan, P. Yang, Y. Ma, Q. Xu and B. Tang, *Angew. Chem., Int. Ed.*, 2023, **62**, e202309624.
99 C. Shu, X. Yang, L. Liu, X. Hu, R. Sun, X. Yang, A. I. Cooper, B. Tan and X. Wang, *Angew. Chem., Int. Ed.*, 2024, **63**, e202403926.
100 J. Yang, Z. Zhao, X. Liu, H. Yang, J. Yang, M. Zhou, S. Li, X. Liu, X. Xu and C. Cheng, *Nat. Commun.*, 2025, **16**, 7654.
101 Z. Xue, B. Zhang, Q. Guo, Y. Wang, Q. Li, K. Yang and S. Qiao, *Adv. Mater.*, 2025, **37**, e10201.
102 M. Deng, L. Wang, Z. Wen, J. Chakraborty, J. Sun, G. Wang and P. Van Der Voort, *Green Chem.*, 2024, **26**, 3239–3248.
103 H. Ma, Y. Zhang, Y. Wu, Q. Gu, Z. Li and Q. Zhang, *Chem. Sci.*, 2025, **16**, 16668–16677.
104 Z. Zhang, Y. Hou, S. Zhu, L. Yang, Y. Wang, H. Yue, H. Xia, G. Wu, S. wang Yang and X. Liu, *Angew. Chem., Int. Ed.*, 2025, **64**, e202505286.
105 J. Chen, S. Yan, F. Wang, F. Lin, J. Lin, R. A. Borse and Y. Wang, *Angew. Chem., Int. Ed.*, 2025, **64**, e202500924.
106 H. Wang, C. Yang, F. Chen, G. Zheng and Q. Han, *Angew. Chem., Int. Ed.*, 2022, **61**, e20220232.
107 Y. Yang, J. Kang, Y. Li, J. Liang, J. Liang, L. Jiang, D. Chen, J. He, Y. Chen and J. Wang, *New J. Chem.*, 2022, **46**, 21605–21614.
108 J. N. Chang, Q. Li, J. W. Shi, M. Zhang, L. Zhang, S. Li, Y. Chen, S. L. Li and Y. Q. Lan, *Angew. Chem., Int. Ed.*, 2023, **62**, e202218868.
109 J.-C. Liu, C. Tuo, W.-Y. Xiao, M.-Y. Qi, Y. Yusran, Z.-T. Wang, H. Li, C.-S. Guo, J.-L. Song, S.-L. Qiu, Y.-J. Xu and Q. Fang, *Angew. Chem., Int. Ed.*, 2025, **64**, e202416240.
110 R. Wang, Z. Wang, L. Li, L. Zhang, Ji. Zhang, H. Jin, Q. Xu, Y. Wei, Y. Yang and S. Wang, *J. Catal.*, 2025, **450**, 116289.
111 Y. Xie, F. Mao, Q. Rong, X. Liu, M. Hao, Z. Chen, H. Yang, G. I. N. Waterhouse, S. Ma and X. Wang, *Adv. Funct. Mater.*, 2024, **34**, 2411077.
112 H. Xu, Y. Wang, Y. Xu, Q. Wang, M. Zhuang, Q. Liao and K. Xi, *Angew. Chem., Int. Ed.*, 2024, **63**, e202408802.
113 X. Di, X. Lv, H. Wang, F. Chen, S. Wang, G. Zheng, B. Wang and Q. Han, *Chem. Eng. J.*, 2023, **455**, 140124.

114 V. S. Vyas, F. Haase, L. Stegbauer, G. Savasci, F. Podjaski, C. Ochsenfeld and B. V. Lotsch, *Nat. Commun.*, 2015, **6**, 8508.
115 D. Chen, W. Chen, Y. Wu, L. Wang, X. Wu, H. Xu and L. Chen, *Angew. Chem., Int. Ed.*, 2023, **62**, e202217479.
116 Z. Zhang, Q. Zhang, Y. Hou, J. Li, S. Zhu, H. Xia, H. Yue and X. Liu, *Angew. Chem., Int. Ed.*, 2024, **63**, e202411546.
117 X. Yang, Z. X. Pan, J. Y. Yue, X. Li, G. Liu, Q. Xu and G. Zeng, *Small*, 2024, **20**, 2405907.
118 W. Wu, Z. Li, S. Liu, D. Zhang, B. Cai, Y. Liang, M. Wu, Y. Liao and X. Zhao, *Angew. Chem., Int. Ed.*, 2024, **63**, e202404563.
119 Z. Li, B. Cai, Y. Zou, D. Zhang, Y. Liang, Y. Zhou, Y. Ma, X. Wang, B. Shi, W. K. Chen, Y. Liu and X. Zhao, *Adv. Energy Mater.*, 2025, **15**, 2500341.
120 Y. Hou, P. Zhou, F. Liu, Y. Lu, H. Tan, Z. Li, M. Tong and J. Ni, *Angew. Chem., Int. Ed.*, 2024, **63**, e202318562.
121 D. Cao, J. Du, J. Li, Q. Sun, J. Guan and J. Liu, *ACS Catal.*, 2025, **15**, 3584–3594.
122 Y. Ju, H. Lin, G. Tan, P. Su, Z. Wang, C. Hu, R. Hou, T. Hao, F. Chen and Y. Tang, *Nat. Commun.*, 2025, **16**, 5658.
123 H. Yu, F. Zhang, Q. Chen, P. K. Zhou, W. Xing, S. Wang, G. Zhang, Y. Jiang and X. Chen, *Angew. Chem., Int. Ed.*, 2024, **63**, e202402297.
124 L. Guo, L. Gong, Y. Yang, Z. Huang, X. Liu and F. Luo, *Angew. Chem., Int. Ed.*, 2025, **64**, e202414658.
125 Y. Yao, C. Zhu, R. Liu, Q. Fang, S. Song, B. Chen and Y. Shen, *Small*, 2024, **20**, 2404885.
126 S. Kandambeth, A. Mallick, B. Lukose, M. V. Mane, T. Heine and R. Banerjee, *J. Am. Chem. Soc.*, 2012, **134**, 19524–19527.
127 H. Wang, C. Qian, J. Liu, Y. Zeng, D. Wang, W. Zhou, L. Gu, H. Wu, G. Liu and Y. Zhao, *J. Am. Chem. Soc.*, 2020, **142**, 4862–4871.
128 Y. Kong, X. He, H. Wu, Y. Yang, L. Cao, R. Li, B. Shi, G. He, Y. Liu, Q. Peng, C. Fan, Z. Zhang and Z. Jiang, *Angew. Chem., Int. Ed.*, 2021, **60**, 17638–17646.
129 H. Hu, Y. Tao, D. Wang, C. Li, Q. Jiang, Y. Shi, J. Wang, J. Qin, S. Zhou and Y. Kong, *J. Colloid Interface Sci.*, 2023, **629**, 750–762.
130 X. Zhang, J. Zhang, J. Miao, X. Wen, C. Chen, B. Zhou and M. Long, *Chem. Eng. J.*, 2023, **466**, 143085.
131 X. Zhang, S. Cheng, C. Chen, X. Wen, J. Miao, B. Zhou, M. Long and L. Zhang, *Nat. Commun.*, 2024, **15**, 2649.
132 H. Li, Y. Li, X. Lv, C. Liu, N. Zhang, J. Zang, P. Yue, Y. Gao, C. Liu and Y. Li, *Adv. Mater.*, 2025, **37**, 2415126.
133 K.-H. Xie, G.-B. Wang, F. Huang, F. Zhao, J.-L. Kan, Z.-Z. Chen, L. Cai, S.-L. Han, Y. Geng and Y.-B. Dong, *Nat. Commun.*, 2025, **16**, 3493.
134 T. Yang, D. Zhang, A. Kong, Y. Zou, L. Yuan, C. Liu, S. Luo, G. Wei and C. Yu, *Angew. Chem., Int. Ed.*, 2024, **63**, e202404077.
135 Y. Mou, X. Wu, C. Qin, J. Chen, Y. Zhao, L. Jiang, C. Zhang, X. Yuan, E. Huixiang Ang and H. Wang, *Angew. Chem., Int. Ed.*, 2023, **62**, e20230948.
136 L. Fang, H. Xu, S. Qiu, T. Ye, T. Wang, J. Shang, C. Gu, S. Kitagawa and L. Li, *Angew. Chem., Int. Ed.*, 2025, **64**, e202423220.
137 H.-H. Sun, Z.-B. Zhou, Y. Fu, Q.-Y. Qi, Z.-X. Wang, S. Xu and X. Zhao, *Angew. Chem., Int. Ed.*, 2024, **63**, e202409250.
138 A. Chakraborty, A. Alam, U. Pal, A. Sinha, S. Das, T. Saha-Dasgupta and P. Pachfule, *Nat. Commun.*, 2025, **16**, 503.
139 T. Xu, Z. Wang, W. Zhang, S. An, L. Wei, S. Guo, Y. Huang, S. Jiang, M. Zhu, Y. B. Zhang and W. H. Zhu, *J. Am. Chem. Soc.*, 2024, **146**, 20107–20115.
140 J. Y. Yue, Y. F. Fan, Z. X. Pan, P. Yang, Y. Ma, Q. Xu and B. Tang, *ACS Catal.*, 2024, **14**, 4728–4737.
141 W. Wang, R. Zhang, H. Chu, Z. Zhan, Q. Huang, Z. Li, X. Wang, F. Bai and W. Zhou, *Small*, 2025, **21**, 2406527.
142 P. Li, H. Zhao, R. Ji, W. Chi, X. Sun, Y. Dong and Y. Zhu, *Catal. Sci. Technol.*, 2024, **14**, 2470–2478.
143 K. Prakash, R. Deka and S. M. Mobin, *Inorg. Chem. Front.*, 2024, **11**, 6711–6752.
144 C. Pan, Y. Han and J. Lu, *Appl. Sci.*, 2020, **10**, 6374.
145 R. Freund, S. Canossa, S. M. Cohen, W. Yan, H. Deng, V. Guillerm, M. Eddaoudi, D. G. Madden, D. Fairen-Jimenez, H. Lyu, L. K. Macreadie, Z. Ji, Y. Zhang, B. Wang, F. Haase, C. Wöll, O. Zaremba, J. Andreo, S. Wuttke and C. S. Diercks, *Angew. Chem., Int. Ed.*, 2021, **60**, 23946–23974.
146 J. Y. Yue, J. X. Luo, Z. X. Pan, R. Z. Zhang, P. Yang, Q. Xu and B. Tang, *Angew. Chem., Int. Ed.*, 2024, **63**, e202405763.
147 J. Cheng, Y. Wu, W. Zhang, L. Wang, X. Wu and H. Xu, *Adv. Mater.*, 2025, **37**, 2410247.
148 H. M. El-Kaderi, J. R. Hunt, J. L. Mendoza-Cortés, A. P. Côté, R. E. Taylor, M. O'Keeffe and O. M. Yaghi, *Science*, 2007, **316**, 268–272.
149 X. Guan, F. Chen, Q. Fang and S. Qiu, *Chem. Soc. Rev.*, 2020, **49**, 1357–1384.
150 K. Yu, P. He, D. Zhang, H. Wu, K. Shu, H. Long, Y. Sun, X. Pei, B. Jiang, K. Cao, Y. Li and L. Ma, *Angew. Chem., Int. Ed.*, 2025, **64**, e202511501.
151 R.-M. Zhu, Y. Liu, W.-K. Han, J.-D. Feng, J. Zhang, H. Pang, J. Zhang and Z.-G. Gu, *Angew. Chem., Int. Ed.*, 2025, **64**, e202412890.
152 J. P. Liao, M. Zhang, P. Huang, L. Z. Dong, T. T. Ma, G. Z. Huang, Y. F. Liu, M. Lu, S. L. Li and Y. Q. Lan, *ACS Catal.*, 2024, **14**, 3778–3787.
153 W. Lan, B. Wei, Y. Jin, S. Xu, H. Zhou, Y. Wu, Q. Liu, P. Chen, J. Wang, X. Zhao, H. Meng, L. Liu, D. Wang, H. Huang, Y. Wei, Q. Zhu and Y. Yu, *Small*, 2025, **21**, 2501327.
154 Z. Gong, Y. Gao, J. Li, Z. Cai, N. Liu and J. Jiang, *Angew. Chem., Int. Ed.*, 2025, **64**, e202423205.
155 X. Wang, Y. Jin, N. Li, H. Zhang, X. Liu, X. Yang, H. Pan, T. Wang, K. Wang, D. Qi and J. Jiang, *Angew. Chem., Int. Ed.*, 2024, **63**, e202401014.
156 Z. S. Zhu, S. Zhong, C. Cheng, H. Zhou, H. Sun, X. Duan and S. Wang, *Chem. Rev.*, 2024, **124**, 11348–11434.
157 Y. Liu, L. Li, Z. Sang, H. Tan, N. Ye, C. Sun, Z. Sun, M. Luo and S. Guo, *Nat. Synth.*, 2025, **4**, 134–141.
158 Z. Ding, J. Yang, Z. Wu, M. Adeli, X. Luo, X. Wang, X. Xie, X. Xu, C. Cheng and C. Zhao, *Chem. Mater.*, 2025, **37**, 1972–1982.

159 Y. Zhang, Y. Wu, H. Ma, Y. Gao, X. Fan, Y. Zhao, F. Kang, Z. Li, Y. Liu and Q. Zhang, *Small*, 2025, **21**, 2500674.
160 Q. Zhou, Y. Guo and Y. Zhu, *Nat. Catal.*, 2023, **6**, 574–584.
161 M. Guo, C. He, Z. Wu, Y. Tian, J. Yang, Y. Wang, H. Wu, J. Yang, M. Xu, W. Xue, C. Cheng, S. Li and C. Zhao, *Adv. Sci.*, 2025, **12**, e05794.
162 X. Ding, T. Wang, B. Yu, Q. Zhi, H. Wang, H. Liu, P. A. Stuzhin and J. Jiang, *Adv. Funct. Mater.*, 2025, 2422291.
163 X. F. Lu, Y. Fang, D. Luan and X. W. D. Lou, *Nano Lett.*, 2021, **21**, 1555–1565.
164 W. Xia, A. Mahmood, R. Zou and Q. Xu, *Energy Environ. Sci.*, 2015, **8**, 1837–1866.
165 J. Lee, O. K. Farha, J. Roberts, K. A. Scheidt, S. T. Nguyen and J. T. Hupp, *Chem. Soc. Rev.*, 2009, **38**, 1450–1459.
166 W. Cheng, X. F. Lu, D. Luan and X. W. Lou, *Angew. Chem., Int. Ed.*, 2020, **59**, 18234–18239.
167 S. Zhao, Y. Wang, J. Dong, C. T. He, H. Yin, P. An, K. Zhao, X. Zhang, C. Gao, L. Zhang, J. Lv, J. Wang, J. Zhang, A. M. Khattak, N. A. Khan, Z. Wei, J. Zhang, S. Liu, H. Zhao and Z. Tang, *Nat. Energy*, 2016, **1**, 16184.
168 J. Q. Shen, P. Q. Liao, D. D. Zhou, C. T. He, J. X. Wu, W. X. Zhang, J. P. Zhang and X. M. Chen, *J. Am. Chem. Soc.*, 2017, **139**, 1778–1781.
169 N. Diyali, S. Rasaily and B. Biswas, *Coord. Chem. Rev.*, 2022, **469**, 214667.
170 S. Rasaily, D. Sharma, S. Pradhan, N. Diyali, S. Chettri, B. Gurung, S. Tamang and A. Pariyar, *Inorg. Chem.*, 2022, **61**, 13685–13699.
171 D. Sharma, S. Rasaily, S. Chettri, D. Sureka, S. Tamang and A. Pariyar, *Inorg. Chem.*, 2023, **62**, 4540–4549.
172 (*a*) L. J. Murray, M. Dincă and J. R. Long, *Chem. Soc. Rev.*, 2009, **38**, 1294–1314; (*b*) H. Li, L. Li, R. B. Lin, W. Zhou, Z. Zhang, S. Xiang and B. Chen, *J. Energy Chem.*, 2019, **1**, 100006.
173 R. B. Lin, S. Xiang, W. Zhou and B. Chen, *Chem*, 2020, **6**, 337–363.
174 S. Dutta, S. Mukherjee, O. T. Qazvini, A. K. Gupta, S. Sharma, D. Mahato, R. Babarao and S. K. Ghosh, *Angew. Chem., Int. Ed.*, 2022, **61**, e202114132.
175 S. Mollick, S. Saurabh, Y. D. More, S. Fajal, M. M. Shirolkar, W. Mandal and S. K. Ghosh, *Energy Environ. Sci.*, 2022, **15**, 3462–3469.
176 S. Fajal, D. Ghosh, W. Mandal and S. K. Ghosh, *Chem. Commun.*, 2024, **60**, 1884–1887.
177 H. Sohrabi, S. Ghasemzadeh, Z. Ghoreishi, M. R. Majidi, Y. Yoon, N. Dizge and A. Khataee, *Mater. Chem. Phys.*, 2023, **299**, 127512.
178 P. Samanta, S. Let, W. Mandal, S. Dutta and S. K. Ghosh, *Inorg. Chem. Front.*, 2020, **7**, 1801–1821.
179 A. Karmakar, N. Kumar, P. Samanta, A. V. Desai and S. K. Ghosh, *Chem.–Eur. J.*, 2016, **22**, 864–868.
180 H. S. Wang, Y. H. Wang and Y. Ding, *Nanoscale Adv.*, 2020, **2**, 3788–3797.
181 J. Y. Choi, B. Check, X. Fang, S. Blum, H. T. B. Pham, K. Tayman and J. Park, *J. Am. Chem. Soc.*, 2024, **146**, 11319–11327.
182 X. Wang, J. Li, X. Wei, J. Song, J. Xie, Z. Li, M. Yuan, L. Jiang, Y. Wang, C. Liang and W. Liu, *ACS Omega*, 2024, **9**, 33671–33678.
183 Y. Zhang, Z. Luo, T. Zhou, H. Huang and H. Tang, *Chem. Commun.*, 2024, **60**, 1920–1923.
184 Y. Zheng, H. Zhou, B. Zhou, J. Mao and Y. Zhao, *Catal. Sci. Technol.*, 2022, **12**, 969–975.
185 X. Y. Ji, Y. Y. Wang, Y. Li, K. Sun, M. Yu and J. Tao, *Nano Res.*, 2022, **15**, 6045–6053.
186 Y. Zhang, C. Pan, G. Bian, J. Xu, Y. Dong, Y. Zhang, Y. Lou, W. Liu and Y. Zhu, *Nat. Energy*, 2023, **8**, 361–371.
187 M. Shao, R. Bao, H. Guo, C. Yao, S. Wang, Y. Song and X. Guo, *Inorg. Chem.*, 2025, **64**, 18567–18576.
188 A. Pal, S. Suresh, A. Khan, L. Huai Kuo, L. Tang Chi, A. Ganguly, C.-Y. Kao, M. Kumar Sharma, T.-S. Andrew Wang, D.-Y. Kang and Z.-H. Lin, *Sci. Adv.*, 2025, **11**, 4711.
189 Y.-X. Li, Y. Hu, H.-S. Bae, J. Du, S. Zhao, D. Pan and W. Choi, *ACS Nano*, 2024, **42**, 29233–29247.
190 S. Fajal, S. Dutta and S. K. Ghosh, *Mater. Horiz.*, 2023, **10**, 4083–4138.
191 A. Trewin and A. I. Cooper, *Angew. Chem., Int. Ed.*, 2023, **2010**(49), 1533–1535.
192 B. Mishra, A. Alam, B. Kumbhakar, D. Díaz Díaz and P. Pachfule, *Cryst. Growth Des.*, 2023, **23**, 4701–4719.
193 C. Liu, M. Chen, H. Li, Q. Shi, Y. Feng and B. Zhang, *Cryst. Growth Des.*, 2022, **22**, 4745–4756.
194 L. Liao, M. Li, Y. Yin, J. Chen, Q. Zhong, R. Du, S. Liu, Y. He, W. Fu and F. Zeng, *ACS Omega*, 2023, **8**(5), 4527–4542.
195 M. Liu, L. Guo, S. Jin and B. Tan, *J. Mater. Chem. A*, 2019, **7**, 5153–5172.
196 S. R. Zhu, Q. Qi, Y. Fang, W. N. Zhao, M. K. Wu and L. Han, *Cryst. Growth Des.*, 2018, **18**, 883–891.
197 F. Niu, L. Tao, Y. Deng, H. Gao, J. Liu and W. Song, *New J. Chem.*, 2014, **38**, 5695–5699.
198 C. Yang, W. Huang, L. C. da Silva, K. A. I. Zhang and X. Wang, *Chem.–Eur. J.*, 2018, **24**, 17454–17458.
199 S. Kumar, B. Bayarkhuu, H. Ahn, H. Cho and J. Byun, *Nano Trends*, 2023, **4**, 100023.
200 H. Zhang, W. Wei, K. Chi, Y. Zheng, X. Y. Kong, L. Ye, Y. Zhao and K. A. I. Zhang, *ACS Catal.*, 2024, 17654–17663.
201 L. Zhang, C. Wang, Q. Jiang, P. Lyu and Y. Xu, *J. Am. Chem. Soc.*, 2024, **146**, 29943–29954.
202 L. Chen, L. Wang, Y. Wan, Y. Zhang, Z. Qi, X. Wu and H. Xu, *Adv. Mater.*, 2020, **32**, 1904433.
203 Y. Yang, Q. Guo, Q. Li, L. Guo, H. Chu, L. Liao, X. Wang, Z. Li and W. Zhou, *Adv. Funct. Mater.*, 2024, **34**, 2400612.
204 X. Nie, Y. Zhao, W. Gao, W. Liu, X. Cheng, Y. Gao, N. Shang, S. Gao and C. Wang, *Chem.–Eur. J.*, 2023, **29**, e202203607.
205 Y. Wang, W. Chi, R. Zhang, Y. Guo, X. Sun, H. Zhao, J. Zhang, Y. Dong and Y. Zhu, *New J. Chem.*, 2024, **48**, 9043–9051.
206 X. Xu, D. Jiang, K. Xie, Y. Sui, W. Chen, Y. Li, H. Zhong and H.-R. Wen, *ACS Appl. Polym. Mater.*, 2025, **7**, 6920–693.
207 X. Xu, L. Chai, Y. Li, W. Chen, X. Li, W. Huang, G. Zhou, H. Zhong and Y. Sui, *Polymer*, 2025, **340**, 129236.
208 G. Lv, X. Yu, J. Wang, J. Qiu, D. Yang and Y. Zhu, *Adv. Funct. Mater.*, 2026, **36**, e17393.

209 R. Sun, X. Yang, X. Hu, Y. Guo, Y. Zhang, C. Shu, X. Yang, H. Gao, X. Wang, I. Hussain and B. Tan, *Angew. Chem., Int. Ed.*, 2025, **64**, e202416350.
210 Y. Guo, X. Yang, R. Sun, X. Hu, C. Shu, X. Yang, H. Gao, X. Wang and B. Tan, *Small*, 2024, **20**, 2403743.
211 X. Xu, Y. Sui, W. Chen, S. Xiong, Y. Li, X. Li, W. Huang, H. Zhao, G. Zhou, H. Chen and H. Zhong, *ACS Sustain. Chem. Eng.*, 2024, **12**, 11409–11418.
212 S. Lee, H. Jeong, D. Nam, M. S. Lah and W. Choe, *Chem. Soc. Rev.*, 2021, **50**, 528–555.
213 A. J. Gosselin, C. A. Rowland and E. D. Bloch, *Chem. Rev.*, 2020, **120**, 8987–9014.
214 E. S. M. El-Sayed, Y. Di Yuan, D. Zhao and D. Yuan, *Acc. Chem. Res.*, 2022, **55**, 1546–1560.
215 Y. P. Wang, Y. Zhang, X. H. Duan, J. J. Mao, M. Pan, J. Shen and C. Y. Su, *Coord. Chem. Rev.*, 2024, **501**, 215570.
216 D. Majumder, S. Fajal, M. M. Shirolkar, A. Torris, Y. Banyla, K. Biswas, S. Rasaily and S. K. Ghosh, *Angew. Chem., Int. Ed.*, 2025, **64**, e202419830.
217 Y. Liu, L. Huang, L. Qin and T. Zhou, *ChemCatChem*, 2025, **17**, e202401487.
218 Y. L. Lu, Y. P. Wang, K. Wu, M. Pan and C. Y. Su, *Acc. Chem. Res.*, 2024, **57**, 3277–3291.
219 J. N. Lu, J. J. Liu, L. Z. Dong, J. M. Lin, F. Yu, J. Liu and Y. Q. Lan, *Angew. Chem., Int. Ed.*, 2023, **62**, e202308505.
220 L. Xiao, H. Zhao, F. Fu, Y. Han, J. Wang, Q. Dong, X. Hu, N. Wang, Y. Wei, P. Wang, D. Liu and Y. Li, *Angew. Chem., Int. Ed.*, 2025, **64**, e202516678.
221 R. B. Lin, Y. He, P. Li, H. Wang, W. Zhou and B. Chen, *Chem. Soc. Rev.*, 2019, **48**, 1362–1389.
222 B. Wang, R. B. Lin, Z. Zhang, S. Xiang and B. Chen, *J. Am. Chem. Soc.*, 2020, **142**, 14399–14416.
223 W. Yang, A. Greenaway, X. Lin, R. Matsuda, A. J. Blake, C. Wilson, W. Lewis, P. Hubberstey, S. Kitagawa, N. R. Champness and M. Schröder, *J. Am. Chem. Soc.*, 2010, **132**, 14457–14469.
224 Y. He, S. Xiang and B. Chen, *J. Am. Chem. Soc.*, 2011, **133**, 14570–14573.
225 Y. Li, S. Tang, A. Yusov, J. Rose, A. N. Borrfors, C. T. Hu and M. D. Ward, *Nat. Commun.*, 2019, **10**, 4477.
226 C. J. Lu, W. J. Shi, Y. N. Gong, J. H. Zhang, Y. C. Wang, J. H. Mei, Z. M. Ge, T. B. Lu and D. C. Zhong, *Angew. Chem., Int. Ed.*, 2024, **63**, e202405451.
227 Q. Yin, E. V. Alexandrov, D. H. Si, Q. Q. Huang, Z. Bin Fang, Y. Zhang, A. A. Zhang, W. K. Qin, Y. L. Li, T. F. Liu and D. M. Proserpio, *Angew. Chem., Int. Ed.*, 2022, **61**, e202115854.
228 J. H. Zhang, Z. M. Ge, J. Wang, D. C. Zhong and T. B. Lu, *Nat. Commun.*, 2025, **16**, 2448.
229 J. L. Segura, S. Royuela and M. Mar Ramos, *Chem. Soc. Rev.*, 2019, **48**, 3903–3945.
230 Y. Cong, X. Li, S. Zhang, Q. Zheng, Y. Zhang and S. W. Lv, *ACS Appl. Mater. Interfaces*, 2023, **15**, 43799–43809.
231 L. Ma, J. Xu, S. Zhao, L. Li and Y. Liu, *Chem.–Eur. J.*, 2021, **27**, 15795–15805.
232 Y. He, J. Zhao, Y. T. Sham, S. Gao, M. Pan, Q. Chen, G. Huang, P. K. Wong and J. Bi, *ACS Sustain. Chem. Eng.*, 2023, **11**, 17552–17563.
233 G. Xia, J. Qiu, L. Zhang, D. Dai and J. Yao, *Colloids Surf., A*, 2023, **664**, 131124.
234 Y. Yang, Y. Li, X. Ma, L. Xie, D. Lv, L. Jiang, J. He, D. Chen and J. Wang, *Catal. Sci. Technol.*, 2023, **13**, 5599–5609.
235 Q. Shang, Y. Liu, J. Ai, Y. Yan, X. Yang, D. Wang and G. Liao, *J. Mater. Chem. A*, 2023, **11**, 21109–21122.
236 Q. Zuo, B. Chu, X. Ye, F. Li, L. Li and Q. Xu, *J. Am. Chem. Soc.*, 2025, **147**, 34681–34689.
237 J. Qiu, L. Zhang, G. Xia, D. Dai, Y. Tang and J. Yao, *Catal. Sci. Technol.*, 2023, **13**, 2101–2107.
238 Y. Kondo, K. Hino, Y. Kuwahara, K. Mori and H. Yamashita, *J. Mater. Chem. A*, 2023, **11**, 9530–9537.
239 Y. Kondo, K. Hino, Y. Kuwahara, K. Mori, H. Kobayashi and H. Yamashita, *Chem. Commun.*, 2022, **58**, 12345–12348.
240 Y. C. Hao, L. W. Chen, J. Li, Y. Guo, X. Su, M. Shu, Q. Zhang, W. Y. Gao, S. Li, Z. L. Yu, L. Gu, X. Feng, A. X. Yin, R. Si, Y. W. Zhang, B. Wang and C. H. Yan, *Nat. Commun.*, 2021, **12**, 2682.
241 Y. Lin, J. Zou, X. Wu, S. Tong, Q. Niu, S. He, S. Luo and C. Yang, *Nano Lett.*, 2024, **24**, 6302–6311.
242 Z. Li, X. Shi, H. Cheng, Y. Song, Y. Jiao, S. Shi, J. Gao and J. Hou, *Adv. Energy Mater.*, 2024, **14**, 2302797.
243 J. Zhu, X. F. Lu, D. Luan and X. W. Lou, *Angew. Chem., Int. Ed.*, 2024, **63**, e202408846.
244 S. Rasaily, K. Baruah, D. Sharma, P. Lepcha, S. Biswas, A. N. Biswas, S. Tamang and A. Pariyar, *Inorg. Chem.*, 2023, **62**, 3026–3035.
245 S. Rasaily, S. Chettri, D. Sharma, K. Baruah, R. Dewan, S. Tamang and A. Pariyar, *Inorg. Chem.*, 2024, **63**, 17846–17855.
246 Y. T. Zheng, S. Li, N. Y. Huang, X. Li and Q. Xu, *Coord. Chem. Rev.*, 2024, **510**, 215858.
247 M. I. Gonzalez, A. B. Turkiewicz, L. E. Darago, J. Oktawiec, K. Bustillo, F. Grandjean, G. J. Long and J. R. Long, *Nature*, 2020, **577**, 64–68.
248 Z. R. Tao, J. X. Wu, Y. J. Zhao, M. Xu, W. Q. Tang, Q. H. Zhang, L. Gu, D. H. Liu and Z. Y. Gu, *Nat. Commun.*, 2019, **10**, 2911.
249 C. D. Gheewala, B. E. Collins and T. H. Lambert, *Science*, 2016, **351**, 961–965.